

CABLE AXIAL LOAD MEASUREMENT DEVICE AND BUCKLING SENSOR
DEVELOPMENT

A THESIS SUBMITTED TO
THE GRADUATE SCHOOL OF NATURAL AND APPLIED SCIENCES
OF
MIDDLE EAST TECHNICAL UNIVERSITY

BY

EMİNE CEREN USALAN

IN PARTIAL FULFILLMENT OF THE REQUIREMENTS
FOR
THE DEGREE OF MASTER OF SCIENCE
IN
CIVIL ENGINEERING

AUGUST 2015

Approval of the thesis:

**CABLE AXIAL LOAD MEASUREMENT DEVICE AND BUCKLING
SENSOR DEVELOPMENT**

Submitted by **EMİNE CEREN USALAN** in partial fulfillment of the requirements for the degree of **Master of Science in Civil Engineering Department, Middle East Technical University** by,

Prof. Dr. Gülbin Dural Ünver
Dean, Graduate School of **Natural and Applied Sciences**

Prof. Dr. Ahmet Cevdet Yalçiner
Head of Department, **Civil Engineering**

Prof. Dr. Ahmet Türer
Supervisor, **Civil Engineering Dept., METU**

Examining Committee Members:

Prof. Dr. Erdem Canbay
Civil Engineering Dept., METU

Prof. Dr. Ahmet Türer
Civil Engineering Dept., METU

Assoc. Prof. Dr. Alp Caner
Civil Engineering Dept., METU

Assoc. Prof. Dr. Özgür Kurç
Civil Engineering Dept., METU

Asst. Prof. Dr. Burcu Güldür
Civil Engineering Dept., Hacettepe University

Date: 21.08.2015

I hereby declare that all information in this document has been obtained and presented in accordance with academic rules and ethical conduct. I also declare that, as required by these rules and conduct, I have fully cited and referenced all material and results that are not original to this work.

Name, Surname: Emine Ceren USALAN

Signature:

ABSTRACT

CABLE AXIAL LOAD MEASUREMENT DEVICE AND BUCKLING SENSOR DEVELOPMENT

Usalan, Emine Ceren

M. Sc., Department of Civil Engineering

Supervisor : Prof. Dr. Ahmet Türer

August 2015, 139 pages

Axial compression or tension carrying members may need to be monitored for their structural behaviors and/or damage detection. In this thesis, two different types of practical and cost efficient monitoring devices are proposed: The column buckling sensor and the cable tension measuring device. The columns of steel structures are prone to buckling due to their slender nature. The buckling sensor is developed by using strain gauges installed in half Wheatstone bridge and measures the strain level of the most critical section. The strain readings are used to determine the critical buckling condition based on tangent slope of the bending and axial strain graph. The readings are repeated in orthogonal directions for columns with symmetric cross section and the program gives warning when the specified load limit is reached. The buckling sensor is tested on rectangular hollow steel profiles with pin end restraints for both elastic and plastic buckling. The test results, which are compatible with the

theory, prove that the buckling sensor works as intended. The cable tension measuring device is developed for measurement of axial load levels in the cables using a low tech sensor without assembling a complicated electronic setup. The device consists of a slender beam with a circular section attached in the mid-span, a laser pointer device at one end and a ruler at the other end for measuring the slope at supports. The beam is clamped to the cable at both ends to bend the beam around the middle circular section. As the slopes at the ends are measured, the bending shape as well as the force at the mid-span can be calculated. The mid-span force and deformed shape of the slender beam and cable can be used to calculate the axial force in the cable. The simplicity and size that permits mobility of the device are its advantages. A prototype is developed and tested for moderately stressed cables and the results are found to be compatible with the analytical studies.

Keywords: Axial Load Carrying Members, Buckling, Steel Column, Strain Gauges, Wheatstone Bridge, Cable Tension, Structural Health Monitoring

ÖZ

KABLO EKSENEL YÜK ÖLÇME CİHAZI VE BURKULMA SENSÖRÜ GELİŞTİRİLMESİ

Usalan, Emine Ceren

Yüksek Lisans, İnşaat Mühendisliği Bölümü

Tez Yöneticisi : Prof. Dr. Ahmet Türer

Ağustos 2015, 139 sayfa

Eksenel basınç ya da çekme taşıyan elemanlar yapısal davranışları ve/ya hasar tespiti için izlenmek istenebilir. Bu tezde, iki farklı tip kullanımı kolay ve düşük maliyetli yapısal sağlık izleme cihazı tasarlanmıştır: Kolon burkulma sensörü ve kablo eksenel yük ölçme cihazı. Çelik yapıların kolonları narin yapıları nedeniyle burkulmaya daha yatkındır. Burkulma sensörü, yarım Wheatstone köprüsü şeklinde kurulmuş olan birim deformasyon ölçerler ile en kritik kesitteki gerinim seviyesini ölçecek şekilde geliştirilmiştir. Gerinim okumalarından elde edilen eğilme ve eksenel gerinim grafiklerinin tanjant eğimleri kritik burkulma durumunu hesaplamak için kullanılmaktadır. Bu okumalar, simetrik kesitli kolonlar için her iki ortogonal yönde tekrarlanmakta ve öncedenbelirlenmiş yük sınırı aşıldığında program uyarı vermektedir.

Burkulma sensörü, basit mesnet bağlantılı, dikdörtgen kutu çelik profiller üzerinde hem elastik hem de plastik burkulma için test edilmiştir. Teoriyle uyumlu çıkan test sonuçları, burkulma sensörünün planlandığı gibi çalıştığını kanıtlamaktadır. Kablo gerilme ölçme cihazı, kablolarda karmaşık bir elektronik düzenek kurmaksızın yük seviyelerini düşük teknoloji bir cihazla ölçmek için geliştirilmiştir. Cihaz, orta noktasına dairesel bir kesit bağlı olan narin bir kirişten, bir uçta lazer cihazı ile diğer uçta mesnetlerdeki eğim ölçümü için cetvelden oluşmaktadır. Kiriş kabloya her iki uçtan tuttularak ortadaki dairesel kesitin etrafında eğilmesi sağlanır. Uçlardaki eğim ölçülerek, kirişin eğilme şekli ve açıklık ortasındaki kuvvet hesaplanabilir. Açıklık ortasındaki kuvvet ve narin kirişin deforme olmuş şekli kablodaki aksenal yükü hesaplamada kullanılmaktadır. Düzenegin basitliđi ve taşınabilir boyutları cihazın avantajlarındandır. Orta seviyede gerilmelerde çalışan kablolar için bir örnek geliştirilmiş ve sonuçlar analitik çalışmalar ile uyumlu çıkmıştır.

Anahtar kelimeler: Aksenal Yük Taşıyan Elemanlar, Burkulma, Çelik Kolon, Birim Deformasyon Ölçer, Wheatstone Köprüsü, Kablo Gerilmesi, Yapısal Sağlık İzleme.

To my family, friends, and my dearest Tuğcan

ACKNOWLEDGEMENTS

First of all, I would like to thank my supervisor Prof. Dr. Ahmet Türer for always supporting me and guiding me through this challenging period. He always encouraged me to do better and never withheld his help.

I owe thanks to my family for always being there when I was in distress, and trying everything they could to keep me comfortable throughout this exhausting journey. My father İbrahim Usalan, my mother Nilüfer Usalan and my sister Cansu Usalan, I am grateful for you are my family. I also appreciate the efforts of my cat to comfort me by sleeping on my desk or computer each and every time I was working. It really did help minimizing my stress.

I am also grateful to the assistants of room K2-105 Gizem Mestav Sarıca, İsmail Ozan Demirel, Alper Aldemir and Erhan Budak for hosting me in their room during my studies in the laboratory. I would also like to thank to Hasan Metin for helping me preparing the test setups and everything else in the laboratory. Thanks to Feyza Soysal and Utku Albostan for breakfast sessions every morning I was in school for laboratory tests.

I want to thank my friends and colleagues for supporting and motivating me. Thank you very much Özlem Temel Yalçın, Ezgi Anık, Pelin Ergen, Elif Ün Balıkçı, Afşin Emrah Demirtaş, Cemal İçel, Başak Seyisoğlu, Volkan Aydoğan and all my other friends whose names I might have forgotten.

My special thanks goes to Arzu İpek Yılmaz and Naz Topkara Özcan who have always been there for me in every obstacle during my thesis study, motivating me, cheering me up and listening to me when I was stressed. Your places cannot be replaced, thanks for being my friends.

Last but not last, I would like to express my greatest gratitude to my boyfriend Tuğcan Selimhocaoğlu for being always on my side, encouraging me to collect my energy to proceed whenever I breakdown, always coming up with solutions when I was in distress, and simply for being with me. I cannot think how life would be without you by my side.

TABLE OF CONTENTS

ABSTRACT.....	v
ÖZ.....	vii
ACKNOWLEDGEMENTS.....	x
TABLE OF CONTENTS.....	xii
LIST OF TABLES.....	xv
LIST OF FIGURES.....	xvi
LIST OF SYMBOLS.....	xx
CHAPTERS	
1. INTRODUCTION.....	1
1.1 BACKGROUND.....	1
1.2 OBJECTIVE OF THE THESIS.....	3
1.3 SCOPE AND OUTLINE OF THE THESIS.....	7
2. BUCKLING SENSOR DEVELOPMENT.....	9
2.1 BUCKLING THEORY IN LITERATURE.....	9
2.1.1 Euler Buckling Load.....	10
2.1.2 End Conditions.....	14
2.1.3 Plastic Buckling.....	19
2.1.4 Empirical Column Formulae.....	29
2.1.5 Initial Imperfections.....	33

2.2	SENSOR WORKING PRINCIPLES FROM LITERATURE	38
2.2.1	Strain Gauge Working Principles	38
2.2.2	Wheatstone Bridge	45
2.3	ANALYTICAL STUDIES FOR SENSOR DEVELOPMENT	50
2.4	LABORATORY TESTS.....	52
2.4.1	Elastic Buckling Test.....	52
2.4.2	Plastic Buckling Test	56
2.5	DISCUSSION OF RESULTS	59
2.5.1	Elastic Buckling Test Results.....	59
2.5.2	Plastic Buckling Test Results.....	71
3.	CABLE TENSION MEASUREMENT DEVICE	77
3.1	CABLE HISTORY, DEFINITIONS AND COMPOSITION.....	77
3.1.1	History of Modern Cables	77
3.1.2	Definitions and Construction	79
3.2	CABLES UNDER TENSION.....	84
3.2.1	Tensile Force in a Wire.....	84
3.2.2	Tensile Force in a Strand or Wire Rope.....	86
3.2.3	Effect of Poisson's Ratio.....	89
3.2.4	Wire Rope Modulus of Elasticity	90
3.3	VIBRATIONAL ANALYSIS METHOD	91
3.4	DEVICE WORKING PRINCIPLES	93
3.4.1	Governing Equations	94
3.4.2	Modification of equations by real dimensions	96
3.5	ANALYTICAL STUDIES.....	98
3.5.1	Optimization of member dimensions.....	98

3.5.2	Prototype calculations	99
3.6	LABORATORY TESTS	103
3.6.1	Test results	108
3.7	DISCUSSION OF RESULTS.....	110
4.	CONCLUSIONS AND FUTURE WORK	121
	REFERENCES.....	124
APPENDICES		
A.	CABLE AXIAL LOAD MEASUREMENT DEVICE SUPPLEMENTARY DATA FOR OPTIMIZATION	127
B.	CABLE AXIAL LOAD MEASUREMENT DEVICE DATA CHARTS FOR DIFFERENT PARAMETERS.....	133

LIST OF TABLES

TABLES

Table 1. Summary table for fundamental buckling cases	19
Table 2. Different cases for Wheatstone bridge configurations	49
Table 3. Moment per reading calculations	60
Table 4. Prototype-1 Data	100
Table 5. Analytical calculation results for Prototype-1	100
Table 6. Prototype-2 Data	101
Table 7. Analytical calculation results for Prototype-2	102
Table 8. Comparison of different circular section diameters	119
Table 9. Cable axial load measurement device data chart for different parameters.	135

LIST OF FIGURES

FIGURES

Figure 1. Examples to tension members [1]	2
Figure 2. Chord members in a truss either under tension or compression	2
Figure 3. Column under compressive load	2
Figure 4. “Strand Tensionmeter” [5]	4
Figure 5. “Check-Line Cable Tension Meter” [6].....	4
Figure 6. “Rope Tension Gauge” [7].....	5
Figure 7. The buckling of columns following the start of the collapse in 7 World Trade Center[8]	6
Figure 8. Equilibrium of a ball analogy.....	10
Figure 9. Euler column	11
Figure 10. First three buckling mode shapes of a pin-ended column.....	14
Figure 11. Buckling shapes for different end conditions.....	15
Figure 12. Equilibrium of a statically indeterminate column	15
Figure 13. Tangent Modulus Model [12]	21
Figure 14. Tangent Modulus Column Curve [9].....	22
Figure 15. Reduced Modulus Model [12].....	23
Figure 16. Shanley’s column model [9]	26
Figure 17. P/P_T versus y_0/d for an arbitrary value $\tau=0.5$ [9].....	28
Figure 18. Column failure lines	32
Figure 19. Initial imperfections of a column [9].....	33

Figure 20. Magnification factors for imperfection cases [9].....	38
Figure 21. Working principle of strain gauge [17]	39
Figure 22. Strain gauge construction close-up [17].....	41
Figure 23. Difference between accuracy and precision [20].....	42
Figure 24. Strain gauge installation [19].....	45
Figure 25. Wheatstone bridge circuit.....	46
Figure 26. Wheatstone bridge alternatives [17]	47
Figure 27. Hammered tip of column and guide plates.....	52
Figure 28. Strain gauge installation on the column	53
Figure 29. Wiring panel	53
Figure 30. Elastic buckling test setup	54
Figure 31. Elastically buckled column in two different cycles	55
Figure 32. Initial test setup for plastic buckling	56
Figure 33. Final test setup for plastic buckling	57
Figure 34. End crushing of the column before plastic buckling load is reached.....	58
Figure 35. Plastically buckled column.....	58
Figure 36. Axial load – bending moment graph for elastic buckling tests	61
Figure 37. Axial strain – bending strain graph for elastic buckling tests.....	62
Figure 38. Axial stress – bending stress graph for elastic buckling tests.....	62
Figure 39. Rectangular hollow section column bridge configuration	65
Figure 40. Square hollow section column bridge configuration	66
Figure 41. Pin ended circular hollow section column [21]	67
Figure 42. Circular hollow section column bridge configuration	67
Figure 43. Bending strain change determination for buckling warning	69
Figure 44. Warning system based on slope of axial strain – bending strain curve	70

Figure 45. Warning system based on output voltage/load cell reading curve	70
Figure 46. Axial load – bending moment graph for plastic test.....	72
Figure 47. Axial strain – bending strain graph for plastic test.....	73
Figure 48. Axial load – bending moment idealized graph for plastic test.....	73
Figure 49. Axial strain – bending strain idealized graph for plastic test.....	74
Figure 50. Typical spiral wire rope cross-sections [23]	79
Figure 51. Elements of a typical stranded wire rope [24].....	80
Figure 52. Definition of lay length, lay angle and winding radius [23]	81
Figure 53. Strand lay configurations [24].....	82
Figure 54. Cross sections of commonly used wire ropes [25].....	83
Figure 55. Wire rope classification according to usage.....	83
Figure 56. Forces in the individual wires of a strand	85
Figure 57. Wire elongation in a strand [23].....	87
Figure 58. Cable tension measurement device at free and attached states	94
Figure 59. Free-body diagrams of beam and cable	94
Figure 60. Calculation of beam deflection from moment-area theorem	95
Figure 61. Distance between beam and cable in test setup.....	97
Figure 62. Cable - load cell - hydraulic jack assembly	103
Figure 63. Test setup with beam not yet installed.....	104
Figure 64. Test setup with beam installed	105
Figure 65. Detail of circular section in the middle.....	106
Figure 66. End connectors	106
Figure 67. Top – connection of cable to load cell, Bottom – connection of beam to horseshoe connector	107
Figure 68. Top – Ruler at one end of beam, Bottom – Ruler connection detail	108

Figure 69. Laser pointer marking on ruler	108
Figure 70. Test results versus theory, D=80 mm.....	109
Figure 71. Test results versus theory, D=43 mm.....	110
Figure 72. Test results versus modified theory, D=80 mm.....	111
Figure 73. Test results versus modified theory, D=43 mm.....	112
Figure 74. Applied load versus Measured Tension, D=80 mm.....	113
Figure 75. Applied load versus Measured Tension, D=43 mm.....	113
Figure 76. Accuracy of measurements in the first test with D=80 mm	114
Figure 77. Accuracy of measurements in the second test with D=43 mm.....	115
Figure 78. Additional tension relations.....	115
Figure 79. Measured tension and existing tension, D=80 mm.....	117
Figure 80. Measured tension and existing tension, D=43 mm.....	118
Figure 81. Preliminary optimization, L=1000 mm, S235	128
Figure 82. Preliminary optimization, L=1000 mm, S355	129
Figure 83. Preliminary optimization, L=1500 mm, S235	130
Figure 84. Preliminary optimization, L=1500 mm, S355	131

LIST OF SYMBOLS

b	Cross-sectional width
d	Shanley column cross-sectional depth
f_n	Natural frequency
h	Cross-sectional height
h_1	Cross-sectional height of tension side in reduced modulus model
h_2	Cross-sectional height of compression side in reduced modulus model
h_w	Strand length which makes a complete turn
k	Column effective length factor
l	Wire length
m	Mass per unit length of a cable
n	Buckling mode number
n	Number of wire layers
n_s	Number of strands
n_w	Number of wire layers in a strand
q	Distributed load on column
r	Radius of gyration
r_w	Wire winding radius

x	x-coordinate
y	y-coordinate
z	Number of wires in a strand
z_1	Tension side distance from neutral axis in reduced modulus model
z_2	Compression side distance from neutral axis in reduced modulus model
A	Cross-sectional area
A	Cross-sectional area of foil or wire
C_c	Johnson's column constant
D	Circular section diameter attached to beam
E	Modulus of elasticity
E_r	Reduced modulus of elasticity
E_t	Tangent modulus of elasticity
G	Shear modulus
GF	Gauge factor
I	Moment of inertia of a member
I_1	Moment of inertia of tension side in reduced modulus model
I_2	Moment of inertia of compression side in reduced modulus model
J_i	Equatorial moment of inertia in a wire layer i
J_{pi}	Polar moment of inertia in a wire layer i
L	Length

L	Initial length of foil
L_e	Effective length of column
M	Moment
M_b	Wire bending moment about binormal axis
M_{int}	Internal moment
M_{ext}	External moment
M_{tor}	Wire torsional moment
P	Compressive force on column
P	Applied load on cable due to installation
P_c	Column crushing load
P_{cr}	Euler buckling load
$P_{j,l}$	Johnson's linear buckling load
$P_{j,p}$	Johnson's parabolic buckling load
P_R	Reduced modulus buckling load
P_{Ra}	Rankine buckling load
P_T	Tangent modulus buckling load
P_u	Column ultimate load
Q_i	Wire shear force
R	Initial resistance of foil or wire
R	Curvature in reduced modulus model

R_1	Resistance value of strain gauge 1 in Wheatstone bridge circuit
R_2	Resistance value of strain gauge 2 in Wheatstone bridge circuit
R_3	Resistance value of strain gauge 3 in Wheatstone bridge circuit
R_4	Resistance value of strain gauge 4 in Wheatstone bridge circuit
S	Wire rope tensile force
S_i	Strand tensile force
T	Cable tensile force
U_i	Circumference force
V	Shear load on column
V_{Ex}	Excitation voltage in Wheatstone bridge circuit
V_O	Output voltage in Wheatstone bridge circuit
α	Lay angle of a wire rope
α_m	Modification factor for end moments in cable tension measurement device
δ_1	Deflection in cable
δ_2	Deflection in beam
δ_i	Diameter of an individual wire in a strand
δ'	Distance between cable and beam
ε	Extension in wire
ϵ^T	Thermal strain
ϵ_1	Strain value of strain gauge 1 in Wheatstone bridge circuit

ϵ_2	Strain value of strain gauge 2 in Wheatstone bridge circuit
ϵ_3	Strain value of strain gauge 3 in Wheatstone bridge circuit
ϵ_4	Strain value of strain gauge 4 in Wheatstone bridge circuit
ϵ^T	Thermal strain
θ	Beam rotation
θ_o	Shanley column deformed shape rotation
μ	Poisson's ratio of foil or wire material
ν	Wire helix Poisson's ratio equivalent
ρ	Resistivity of a foil or wire
σ	Axial stress
σ_1	Stress in the outside convex in reduced modulus model
σ_2	Stress in the inside concave in reduced modulus model
σ_{all}	Allowable stress
σ_c	Crushing stress
σ_{cr}	Critical stress
σ_u	Ultimate stress
σ_y	Yield stress
σ_z	Wire rope global tensile stress
τ	Ratio of tangent modulus to elastic modulus
τ_r	Ratio of reduced modulus to elastic modulus

Δl	Change in wire length
Δu	Change in winding circumference
ΔR_1	Change in resistance value of strain gauge 1 in Wheatstone bridge circuit
ΔR_2	Change in resistance value of strain gauge 2 in Wheatstone bridge circuit
ΔR_3	Change in resistance value of strain gauge 3 in Wheatstone bridge circuit
ΔR_4	Change in resistance value of strain gauge 4 in Wheatstone bridge circuit
$\Delta \epsilon_1$	Change in strain value of strain gauge 1 in Wheatstone bridge circuit
$\Delta \epsilon_2$	Change in strain value of strain gauge 2 in Wheatstone bridge circuit
$\Delta \epsilon_3$	Change in strain value of strain gauge 3 in Wheatstone bridge circuit
$\Delta \epsilon_4$	Change in strain value of strain gauge 4 in Wheatstone bridge circuit

CHAPTER 1

INTRODUCTION

1.1 BACKGROUND

Axial load carrying members exist in almost every kind of building or non-building structure in the form of columns, truss elements, bracing elements, or cables. Axial load carrying members are divided in two categories: Compression members and tension members. See Figure 1, Figure 2, and Figure 3 for examples to compression and tension members.

The response of an element to axial loading depends on the nature of loading. Tensile load carrying members are expected to yield and/or rupture depending on the material behavior; which means that the strength behavior governs. On the other hand, compressive load carrying members are affected more critically from instability.

Compression members generally occur as chord members in trusses, diagonal braces in braced structures and columns in buildings where the gravity force governs.

Some examples to tension members include cables in suspension or cable-stayed bridges, chord members in trusses, diagonal braces in braced structures, wind columns or columns in buildings where the uplift force governs.

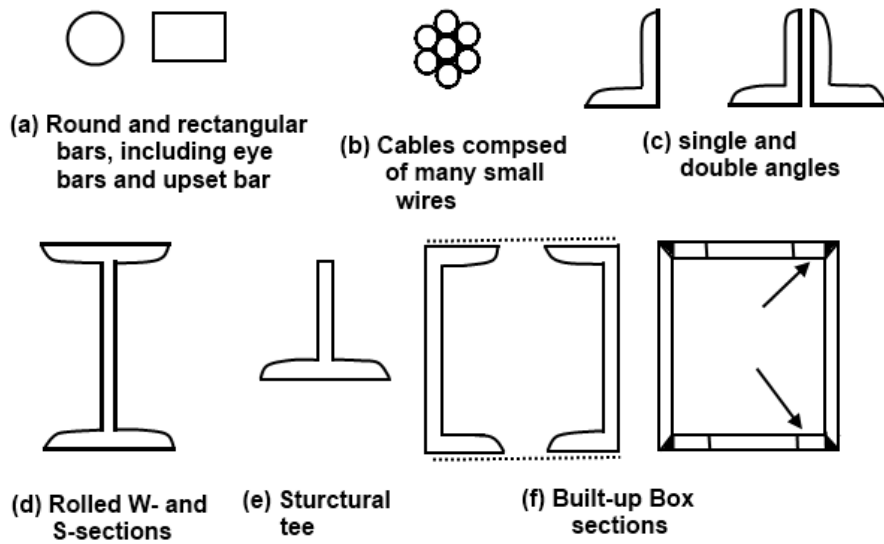


Figure 1. Examples to tension members [1]

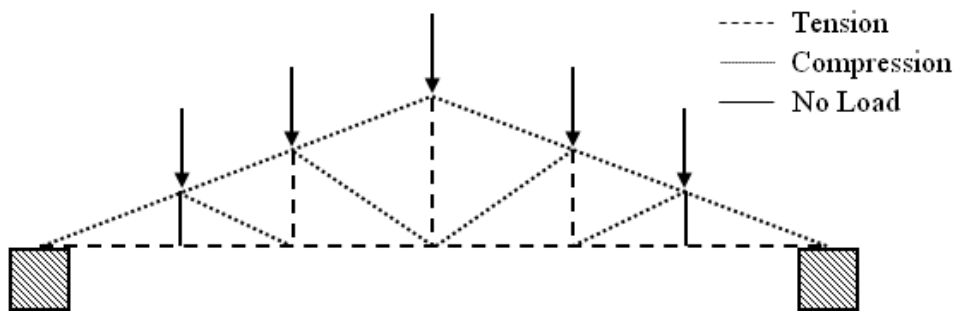


Figure 2. Chord members in a truss either under tension or compression



Figure 3. Column under compressive load

Axial load carrying members can be a very critical part of the structure considered, as in the cables of a cable-stayed or suspension bridge or the main load carrying columns in a building. A constant or transient monitoring might be necessary for these members. There is a variety of monitoring techniques both for compression and

tension members for different types of structures. However, due to the differences in the behavior of the element under different loading conditions, structural health monitoring techniques of tension and compression members are differs from each other a great deal. Moreover, there are many different monitoring tools one can use for these different monitoring techniques.

1.2 OBJECTIVE OF THE THESIS

As a consequence of the above discussions, the goal is to develop easy to use and cost-efficient monitoring tools for both compression and tension members. In this thesis, the development of the column buckling sensor and the cable tension monitoring device will be discussed.

As discussed in the previous section, cables in suspension or cable-stayed bridges are the main tension-load carrying members. Since cables are one of the most important elements in these structures, the monitoring is generally inevitable. There are several methods of monitoring tensile load in the cables. The vibrational analysis method to obtain the tensile load in the cables by making use of natural frequency of the cable is a study investigated by many researchers. One of the recent studies include the tensile load determination of the pedestrian bridge near M.E.T.U. campus conducted by Wandji and Türer (2014). [2] Also, Liao et al. (2001) investigated the wireless PVDF piezoelectric films for in-situ monitoring of cables in cable-stay bridges. [3] This study also is based on the vibrational method. The data collected by PVDF piezoelectric films are used to conduct a vibrational analysis of the cable and then the tensile force in the cable is obtained. More information on vibrational method will also be given in 3.3.

However, the monitoring cost using the conventional methods discussed above might be almost as much as the construction and maintenance cost of the bridge itself, especially for smaller scaled bridges. Hence, a practical and cost-efficient method is developed for measuring smaller-scale stresses in cables. The main advantage of the cable tension monitoring device is its mobility and easy installation. Also, this device does not require early installation and is able to give the tensile stress on the cable directly. For example, it might be necessary to sort the data out by vibrational

analysis to reach the absolute value of the measurement when using the strain gauges.

There are similar products available in the market for cable tension measurement; however, either their working principles are different than the device proposed in this thesis or their load range and/or usage is different.

For example, “Strand Tensionmeter” which can be seen in Figure 4, is a solely mechanical device used for tensioning a strand or measuring the tension in a stressed strand. However, it can be used for a maximum tensile force of about 44 kN. [5]

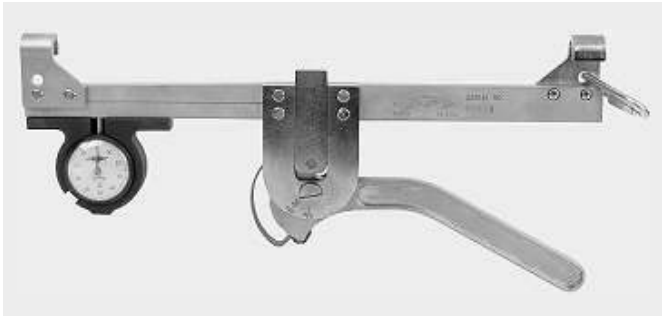


Figure 4. “Strand Tensionmeter” [5]

Another product example is “Check-Line Cable Tension Meter” which can be used to measure tension in guardrails, overhead wires, etc. This device measures the tensile force in a cable and reads the measured value through its digital load cell. It has a load range limited by 45 kN. The device can be used for twenty cable sizes. See Figure 5. [6]

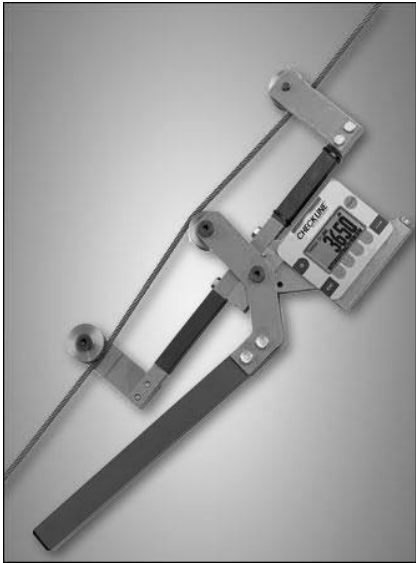


Figure 5. “Check-Line Cable Tension Meter” [6]

A similar device is “Rope Tension Gauge” which is used for tensioning elevator and hoist ropes. It has an adjustable pivot point for different tensile load levels. [7] See Figure 6 for schematic description of this device.

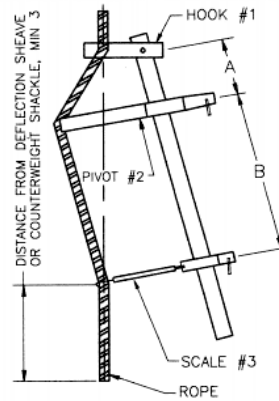


Figure 6. “Rope Tension Gauge” [7]

The main difference of the device proposed in this thesis with the above examples is that it is a low-tech device with a higher tensile load range. Also, the devices given in the examples may not be suitable to use for a bridge cable due to their construction, except for “Cable Tension Meter”. The working principles as well as construction of cable tension measurement device proposed will be explained in detail in Chapter 3.

The second monitoring technique suggested in this thesis is for the steel columns which are the main compressive force resisting members in especially steel frames. Steel columns are especially prone to buckling compared to reinforced concrete columns. A steel cross-section with the equivalent cross-sectional properties (i.e. cross-sectional area, moment of inertia, etc.) as a reinforced concrete cross-section will always be more slender in nature. Even though steel is a very ductile material which can withstand very large inelastic deformations and exhibits an increased strength at strain hardening stage after the yield point is reached, the ductility of the steel is also affected from the stability loss due to buckling. [4] When a steel cross-section buckles under compressive loads, it will fail long before reaching this increased strength due to ductility, yet alone reaching the yield point. Since the main concern is stability for compression members, a buckling sensor for steel columns is

developed. Buckling in columns is very crucial as the critical buckling load is reached, the failure is inevitable.

One of the most catastrophic examples to this is the collapse of the World Trade Center twin towers along with the some other buildings in the World Trade Center complex. After the impact of the plane crashing to the towers, the fire-induced loads caused failure of some members and finally collapse of the twin towers, namely 1 World Trade Center (1WTC) and 2 World Trade Center (2WTC). Then, the debris impact from the collapse of the 1WTC caused severe damage and started out of control fires in the nearby 7 World Trade Center (7WTC) building of the WTC complex. The failure of beams and lateral supports around column 79 of the 7WTC building on Floors 8 to 14 provoked the buckling of the named column. The column failed by pulling the nearby columns 77-78-73-75, finally leading to collapse of the whole structure. See Figure 7 for illustration of the failure.

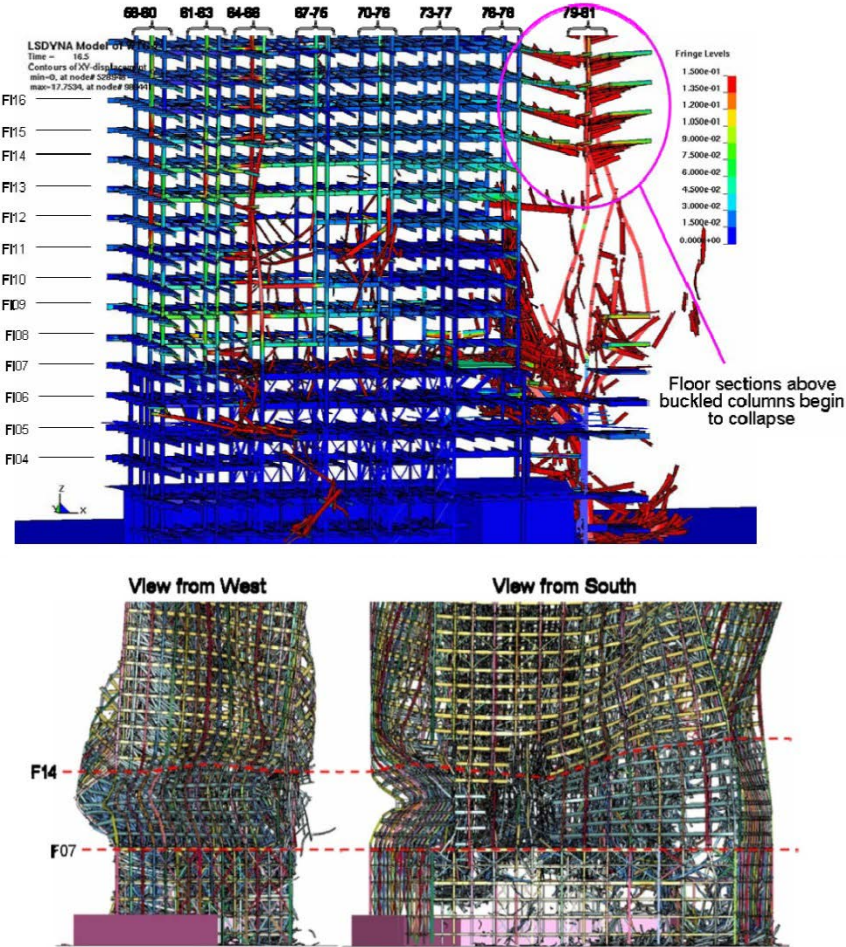


Figure 7. The buckling of columns following the start of the collapse in 7 World Trade Center[8]

As one can understand from the above example, even if the design is safe under expected actions, it might become suddenly unstable under unpredictable situations. [9]

Therefore, monitoring of the columns against buckling might be necessary to prevent a sudden failure. The design codes prohibit development of buckling by guiding the designer to take precautions against instability (i.e. using lateral supports to reduce the buckling length, etc.). However, monitoring of the columns against buckling still might be necessary for reasons such as: double-checking the design, or when an additional load should be considered in the structure which was not taken into account in the design of the structure. The latter is encountered frequently especially in the industrial buildings when an expansion of the current structure is needed or an equipment is changed after the construction is completed.

There are several studies targeting steel column buckling monitoring topic. Most studies include active buckling control or remote controlling with fiber optic sensors. For example, Berlin (1995) investigated the active buckling of columns by using piezo-ceramic actuators. [10] There is also a study conducted by Ravet et al. (2006) on buckling monitoring of columns and pipelines by using Brillouin sensors which are some types of fiber optic remote sensor. [11]

The techniques used in buckling monitoring of members, as the examples given above, are generally makes use of remote sensors which are more expensive compared to many other monitoring tools.

The buckling sensor developed in this thesis is cost-efficient and simple to install. It consists of strain gauges used as half Wheatstone bridge to obtain the current strain level in the column. This strain value obtained is then used to calculate the axial load in the column. The device then alerts if the current axial load is in the vicinity of the appointed percentage of the critical buckling load.

1.3 SCOPE AND OUTLINE OF THE THESIS

This study is divided into four chapters. Chapter 1 gives background information about axial load carrying members as well as some examples of monitoring

methodology found in literature of those members. In Chapter 2, the theory of buckling and the working principles of the buckling sensor developed are explained; moreover, the lab test setup and results are presented. In Chapter 3, the background information about cables is provided; and then, the installation and operation rules of the cable tension measurement device and its prototype properties are demonstrated. Chapter 4 consists of the conclusion remarks and possible future work.

CHAPTER 2

BUCKLING SENSOR DEVELOPMENT

In this chapter, the theory behind the buckling will be presented; then, the mechanism of the buckling sensor developed and the lab tests for the sensor will be explained.

2.1 BUCKLING THEORY IN LITERATURE

Buckling is an instability phenomenon caused by compressive axial loads leading to bend a straight and slender element in lateral direction from its original longitudinal position. In theory, buckling is caused by the bifurcation in the static equilibrium solutions. However, as a matter of fact, there are two kinds of buckling: Bifurcation type buckling and deflection-amplification type buckling. In practice, the latter is the most encountered buckling type. It is due to the fact that the bifurcation type buckling is a conceptual phenomenon which will occur only if the member is perfectly straight and homogeneous, and the compressive load applied is concentric. Apparently, all these three conditions to be met at the same time are not very likely for an ordinary member. [12]

Buckling may occur locally in a part of a member or globally in the member itself. However, the buckling of a single member may cause the main structure to fail; in other words, a whole system instability might be encountered. Since the buckling is a sudden failure, the consequences of a sudden system failure might be fatal, as

illustrated with the World Trade Center example in Chapter 1. In this text, the global buckling of members will be investigated.

Buckling of a column can be explained with the analogy of “equilibrium of a ball”. In Figure 8, all three positions of the ball indicate equilibrium; however, in fact the stability of each ball is different from each other. In (a), when a small disturbance is applied to the ball, it will try to return to its original position when the disturbance is removed, which is called stable equilibrium. In (b), the ball will move away from its original position even when the disturbance is removed. This case is called an unstable equilibrium. In the last case (c), after the removal of the disturbance, the ball will neither try to move away nor come back to its original position, which is called neutral equilibrium. A similar response to the ball example above can be observed in a column. If it is under small loads, the column will keep its original straight shape and will be still stable. However, under larger loads, it will be unstable and cannot keep its original shape. The very moment that the column to pass from the stable equilibrium to unstable equilibrium is the neutral equilibrium state; and the load at this state is called the critical buckling load. [12]

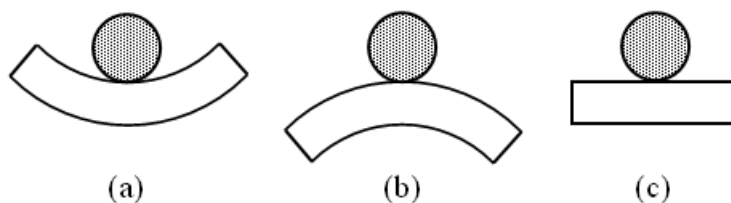


Figure 8. Equilibrium of a ball analogy

The derivation of critical buckling load, which is also called Euler buckling load, will be presented in the following section.

2.1.1 Euler Buckling Load

Euler column, as it is called, is an idealized model to explain the buckling which follows the assumptions listed below [12]:

- The member has a constant cross-sectional area made out of homogeneous material which has a linear-elastic behavior.
- The member is perfectly straight with a concentrated compressive force P acting concentrically.

- The member is pinned at both ends (at the top it can move vertically and free to rotate, but fixed at the horizontal direction).
- Small deformation theorem is valid for the member.

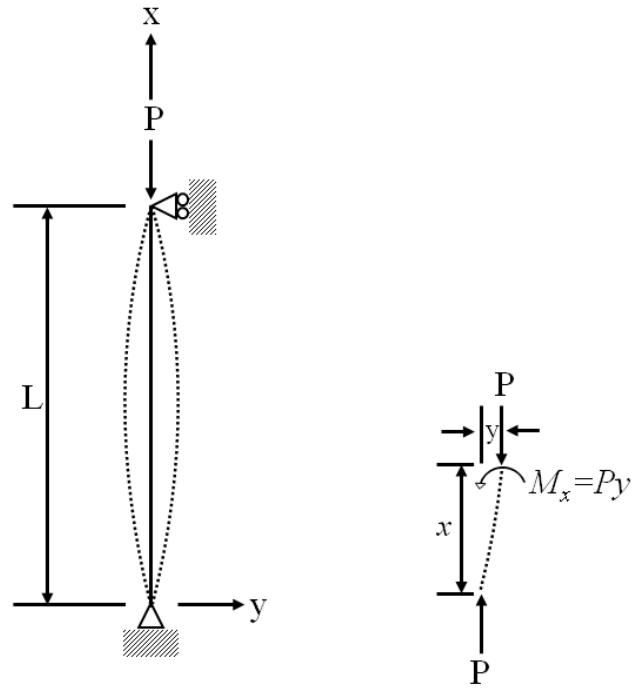


Figure 9. Euler column

As it is also illustrated in Figure 9, when a compressive load P in x -direction is applied, the member will deflect in the lateral y -direction. A secondary moment M will be generated due to small lateral deflection. According to the elastic beam theory, second derivative of deformation gives curvature. When these two formulas are combined, the second order differential equation (1) is obtained.

$$M = P * y \quad (1)$$

$$-\frac{M}{EI} = y'' \quad (2)$$

$$EI * y'' + P * y = 0 \quad (3)$$

The boundary conditions of this equation are as follows for a pin-ended column:

$$y = 0 \text{ at } x = 0 \quad (4)$$

$$y = 0 \text{ at } x = L \quad (5)$$

Equation (3) can be arranged as:

$$y'' + \frac{P}{EI} * y = 0 \quad (6)$$

Let $k^2=P/EI$, then the equation (6) can be written in the form of:

$$y'' + k^2 * y = 0 \quad (7)$$

The solution of this equation is in the form of:

$$y = \alpha e^{mx} \quad (8)$$

Where;

$$y' = \alpha m e^{mx} \quad (9)$$

$$y'' = \alpha m^2 e^{mx} \quad (10)$$

$$\alpha m^2 e^{mx} + k^2 * \alpha m e^{mx} = 0 \quad (11)$$

$$\alpha e^{mx}(m^2 + k^2) = 0 \quad (12)$$

It would be nontrivial solution if $\alpha e^{mx} = 0$, therefore $(m^2 + k^2) = 0$.

$$m = \mp ki \quad (13)$$

Then substituting these solutions into equation (7),

$$y = \alpha e^{\mp kix} \quad (14)$$

Therefore, the solution becomes:

$$y = C1 * \alpha * e^{kix} + C2 * \alpha * e^{-kix} \quad (15)$$

The Euler formula can be used to modify equation (15) as in the form below:

$$e^{ix} = \cos x + i \sin x \quad (16)$$

$$y = A \cos kx + B \sin kx \quad (17)$$

The integral constants A and B can be obtained by substituting the boundary conditions (4) and (5) into equation (17).

$$y = A * \cos 0 + B * \sin 0 = 0, \quad A = 0 \quad (18)$$

$$y = 0 * \cos kL + B * \sin kL = 0, \quad B \neq 0, \sin kL = 0 \quad (19)$$

For nontrivial solution $B \neq 0$ and for $\sin kL = 0$, $kL = n * \pi$ should be satisfied where $n = 1, 2, 3, \dots$. Substituting $k^2 = P/EI$:

$$k = \frac{n * \pi}{L}, \text{ and } k^2 = \frac{n^2 * \pi^2}{L^2} = \frac{P}{EI} \quad (20)$$

$$P_{cr} = \frac{n^2 * \pi^2 * EI}{L^2} \text{ where } n = 1, 2, 3, \dots \quad (21)$$

P_{cr} in equation (21) is the critical buckling load at which the column is in equilibrium position. The solution of P_{cr} is a set of discrete values which are called “eigenvalues”. [12] The positive integer values n determine the buckling mode of the column. All mode shapes of a buckled column are in the form of sinusoidal waves. As the mode number increases, the magnitude of the sine wave will decrease. The critical buckling load for a higher mode will be greater; thus, harder to attain. The smallest buckling load at $n=1$ is the most critical case for a pin-ended column; and if no lateral braces are provided, a column will always buckle in the first mode. Providing lateral braces will increase the mode shape, and thus the critical buckling load. Figure 10 shows the first three modes of a pin-ended column.

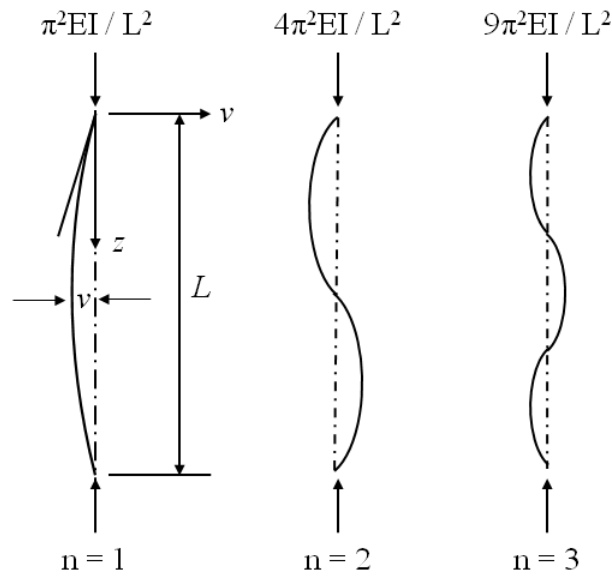


Figure 10. First three buckling mode shapes of a pin-ended column

Also note that, the coefficient B is unknown in the solution; this shows that the magnitude of the sinusoidal mode shape and direction of the buckling cannot be determined. It is called an immaterial property, i.e. independent of the material properties. [12]

2.1.2 End Conditions

The solution of P_{cr} for different modes of a pin-ended column is given in equation (22). However, a column is not always pin-ended. When the end restraint conditions change, critical buckling load P_{cr} also changes since it is a function of column length L. If the column length L is described as L_e , then, equation (22) can be expressed in the form of:

$$P_{cr} = \frac{n^2 * \pi^2 * EI}{L_e^2} \text{ where } n = 1,2,3, \dots \quad (22)$$

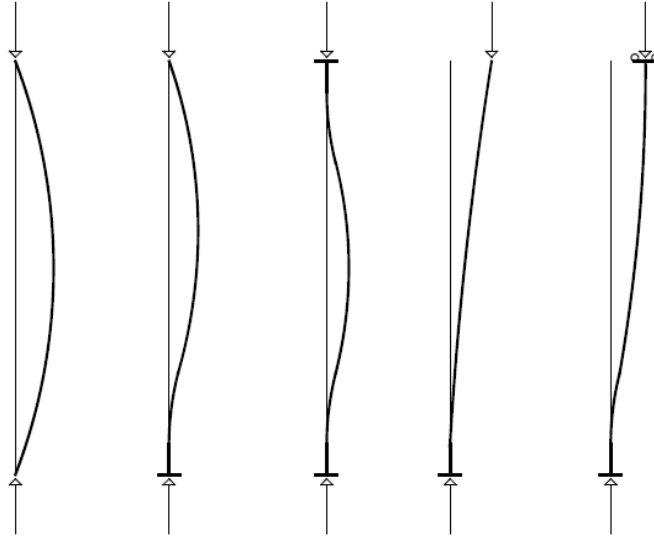


Figure 11. Buckling shapes for different end conditions

Figure 11 shows the five fundamental cases of end conditions. As the end condition changes, due to different boundary conditions, the mode shape and magnitude of buckling load will also change. For fix-ended cases, moment term will also be taken into account. Therefore, a general form of equation is constituted as follows according to the free body diagram at Figure 12. [13]

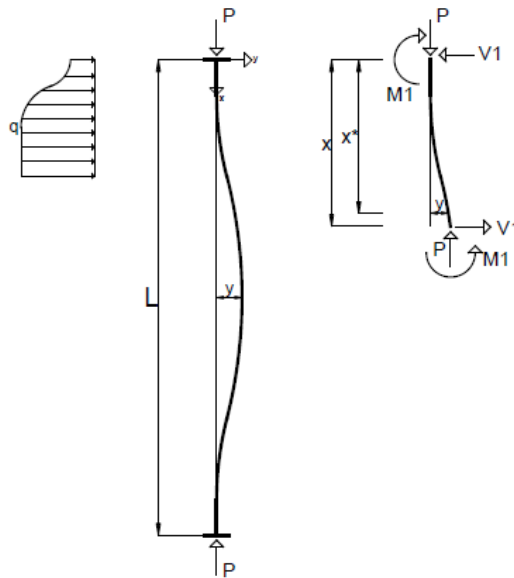


Figure 12. Equilibrium of a statically indeterminate column

According to force and moment equilibrium at the segment;

$$V(x) - V_1 + \int_0^x p(x^*) dx^* = 0 \quad (23)$$

$$M(x) + P * y(x) - M_1 + V * x + \int_0^x q(x^*) * x dx^* = 0 \quad (24)$$

When equations (23) and (24) are differentiated with respect to x, the following equations are obtained:

$$V' + q = 0 \quad (25)$$

$$M' + P * y' + V + V' * x + q * x = 0 \quad (26)$$

Where,

$$V' = -q \quad (27)$$

$$M' + P * y' + V - q * x + q * x = 0 \quad (28)$$

$$M' + P * y' + V = 0 \quad (29)$$

By differentiating equation (28) and substituting it in equation (29), the following equation (30) is obtained. Further substituting $M = EI * y''$ into equation (30), a 4th order ordinary differential equation (31) is obtained. This is the generalized formulation for beam-columns or columns with moment and axial load.

$$(M')' + (P * y')' = q \quad (30)$$

$$(EI * y'')'' + (P * y')' = q \quad (31)$$

It is assumed that the axial force P and the bending rigidity EI does not vary along the beam cross-section, for easier solution. For the homogeneous differential equation where q=0, the solutions are in the form of $y = \alpha e^{mx}$ as in equation (8). Similarly, the characteristic equation is in the form of equation (12). Finally, the solution to the general equation is as follows:

$$y = A \cos mx + B \sin mx + Cx + D + y_p(x) \quad (32)$$

$y_p(x)$ is a particular solution to the distributed load p(x), and A, B, C, D are arbitrary constants.

For different end conditions, the boundary conditions are defined as follows:

- Fixed end: $y = 0, y' = 0$
- Hinge: $y = 0, y'' = \frac{M}{EI} = 0$
- Free end: $M = 0, V = 0$
- Sliding restraint: $y' = 0, V = 0$

For the cases defined in Figure 11, the critical buckling load is obtained by using the general equation (32). Distributed load q is set to zero in the solutions. Case 2, which is a column with one end fixed and one end pinned is used to show the steps of the solution of the general equation.

Boundary conditions:

- $y = 0, \text{ at } x = 0$
- $M = 0 \rightarrow y'' = 0, \text{ at } x = 0$
- $y = 0, \text{ at } x = L$
- $y' = 0, \text{ at } x = L$

$$0 = A \cos 0 + B \sin 0 + C * 0 + D, \quad A + D = 0 \quad (33)$$

$$0 = -A m^2 \cos 0 - B m^2 \sin 0, \quad -A m^2 = 0 \quad (34)$$

$$0 = A \cos mL + B \sin mL + C * L + D \quad (35)$$

$$0 = -Am \sin mL + Bm \cos mL + C \quad (36)$$

The nonzero solution to the system of equations with four unknowns is obtained when the determinant of the system is equal to zero.

$$\begin{aligned} A + D &= 0 \\ -Am^2 &= 0 \\ A \cos mL + B \sin mL + CL + D &= 0 \\ -Am \sin mL + Bm \cos mL + C &= 0 \end{aligned} \quad (37)$$

$$\text{Det} = \begin{vmatrix} 1 & 0 & 0 & 1 \\ -m^2 & 0 & 0 & 0 \\ \cos mL & \sin mL & L & 1 \\ -m \sin mL & m \cos mL & 1 & 0 \end{vmatrix} = 0 \quad (38)$$

$$\text{Det} = m^2(\sin mL - mL \cos mL) = 0 \quad (39)$$

$$m^2 \neq 0, \rightarrow (\sin mL - mL \cos mL) = 0 \quad (40)$$

$$\frac{\sin mL}{\cos mL} - \frac{mL \cos mL}{\cos mL} = \frac{0}{\cos mL}, \rightarrow \tan mL - mL = 0 \quad (41)$$

The final equation obtained (41) is called a transcendental algebraic equation, which means that the approximate roots can be obtained graphically as the intersection points of curves $y = \tan mL$ and $y = mL$. Then, for more accuracy of the root values, Newton method can be used. Finally, the root values are obtained as $mL = 4.4934$, where $m = \sqrt{P/EI}$. Then, P_{cr} is obtained as:

$$P_{cr} = \frac{\pi^2}{(0.699L)^2} EI \cong \frac{\pi^2}{(0.7L)^2} EI \quad (42)$$

Equation (42) shows that for a column with one end pinned and other end fixed, the column effective length for buckling is $L_e = 0.7L$. In a similar manner, the effective length values can be calculated for the cases presented in Figure 10. The boundary conditions, effective length and critical buckling load values for each case is presented in the below summary table.

Table 1. Summary table for fundamental buckling cases

End Restraints	Boundary Conditions	Effective Length, L_e	Critical Buckling Load, P_{cr}
Pin-Pin	$y = 0$ at $x = 0$ $y' = 0$ at $x = L$	L	$P_{cr} = \frac{\pi^2}{L^2} EI$
Fix-Pin	$y = 0$ at $x = 0$ $y'' = 0$ at $x = 0$ $y = 0$ at $x = L$ $y' = 0$ at $x = L$	$0.7L$	$P_{cr} = \frac{\pi^2}{(0.7L)^2} EI$
Fix-Fix	$y = 0$ at $x = 0$ $y' = 0$ at $x = 0$ $y = 0$ at $x = L$ $y' = 0$ at $x = L$	$0.5L$	$P_{cr} = \frac{\pi^2}{(0.5L)^2} EI$
Fix-Free	$y'' = 0$ at $x = 0$ $y''' + m^2 y' = 0$ at $x = 0$ $y = 0$ at $x = L$ $y' = 0$ at $x = L$	$2L$	$P_{cr} = \frac{\pi^2}{(2L)^2} EI$
Fix-Roller	$y' = 0$ at $x = 0$ $y''' + m^2 y' = 0$ at $x = 0$ $y = 0$ at $x = L$ $y' = 0$ at $x = L$	L	$P_{cr} = \frac{\pi^2}{L^2} EI$

2.1.3 Plastic Buckling

The buckling theory is investigated in the previous sections for a linear elastic column. As long as the cross-section is slender, the linear elastic behavior is valid. However, in the case of a short column, due to high axial stresses, the proportional limits are not satisfied. Thus, when the buckling of a short column is considered, plastic behavior should be taken into account.

The problem with Euler's column formula is that even though it works perfectly for slender columns, it is highly unconservative for short columns. Since buckling of short columns will be in the plastic range, the modulus of elasticity E is not constant and actually a function of strain. In 1889, Engesser proposed tangent modulus concept which considered that all the fibers of a column will work with the same modulus of elasticity, tangent modulus, E_T , in the inelastic range. Independent of Engesser, again in 1889, Considère suggested that for buckling above proportional limit, modulus of elasticity E in the Euler's formula should be replaced by an effective modulus, E_{Eff} . This effective modulus is said to be somewhere between elastic modulus E and tangent modulus E_T , according to the tests conducted by Considère. In 1895, Jasinsky pointed out an error in Engesser's formula by stating that in reality, materials unload according to the elastic modulus E ; and thus, the real strength of the column should be greater than the strength obtained with E_T . Later in 1898, Engesser corrected his theory to take into account for elastic unloading, by introducing reduced modulus, E_R . In 1910, von Karman further developed reduced modulus concept by introducing explicit expressions for rectangular and I-shape cross-sections. However, even though the reduced modulus concept was accepted widespread and theoretical validity, still the tests on inelastic buckling were giving results closer to the tangent modulus concept. This controversy was dissipated not until 1947 when Shanley, upon many test results on short aluminum columns, further developed tangent modulus and reduced modulus theories. Shanley's test results demonstrated that the lateral deflections started very near to the range of tangent modulus; however, instability did not start until very near to the reduced modulus range. This can be summarized as the tangent modulus represents a lower bound to the inelastic buckling load while the reduced modulus represents an upper bound. [14]

While controversy and progress on tangent and reduced modulus concepts proceeded, some researchers also worked on empirical formulae based on Euler's equation which can be applied for practical purposes. These are Rankine's formula and Johnson's straight line and parabolic formulae.

The concepts introduced above such as tangent modulus, reduced modulus and Shanley's contributions, as well as Rankine and Johnson's formulae, are all explained in the following sections.

2.1.3.1 Tangent Modulus

Tangent modulus theory assumes that the axial load increases during straight to bent position. This increase in compressive stress is greater than the reduction in flexural stress in the convexly bent extreme fiber. This causes the compressive stress to increase every point and therefore tangent modulus governs for the whole cross-section. [12] See Figure 13 for tangent modulus model description.

It can be assumed that the increase in load P is insignificant compared to P . Then, equation (21) can be written by using tangent modulus as follows:

$$P_T = \frac{\pi^2 E_t I}{L^2} \quad (43)$$

$$\sigma_{cr} = \frac{P_T}{A} = \frac{\pi^2 E_t}{(L/r)^2} = \frac{\pi^2 \tau E}{(L/r)^2} \quad \text{where } \tau = \frac{E_t}{E} < 1.0 \quad (44)$$

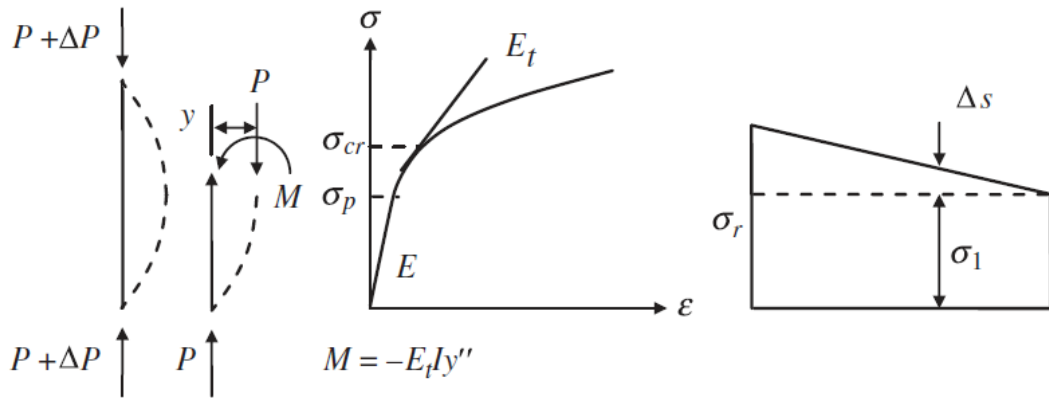


Figure 13. Tangent Modulus Model [12]

In equations (43) and (44), E_t is the slope of the stress-strain curve. The axial load corresponding to stress σ_{cr} is called tangent modulus load P_T . Since in equation (43) tangent modulus is also a function of the stress, the critical stress cannot be calculated analytically. Instead, a column curve as in Figure 14 should be constructed

by using equation (45) and then the critical stress can be obtained from the column curve.

$$(L/r)_{cr} = \pi\sqrt{E_t/\sigma} \tag{45}$$

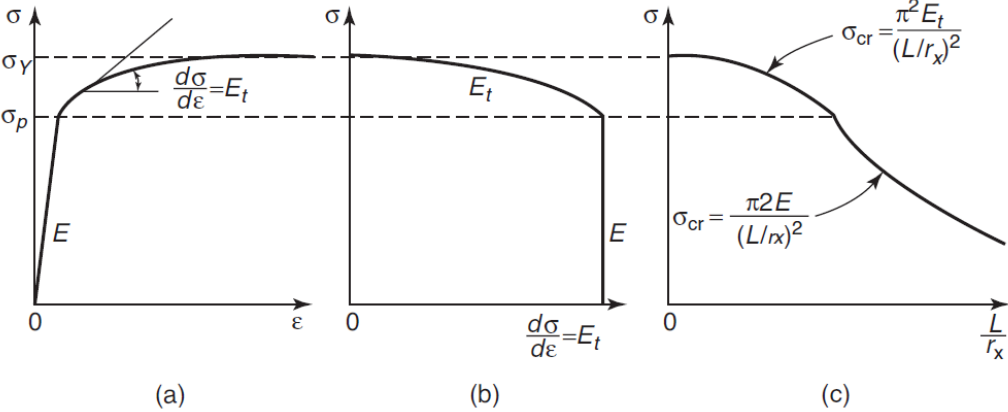


Figure 14. Tangent Modulus Column Curve [9]

2.1.3.2 Reduced Modulus

In reduced modulus theory, it is assumed that axial load remains constant as the member deforms from straight to bent position, unlike tangent modulus theory. [12] See Figure 15 for reduced modulus model description.

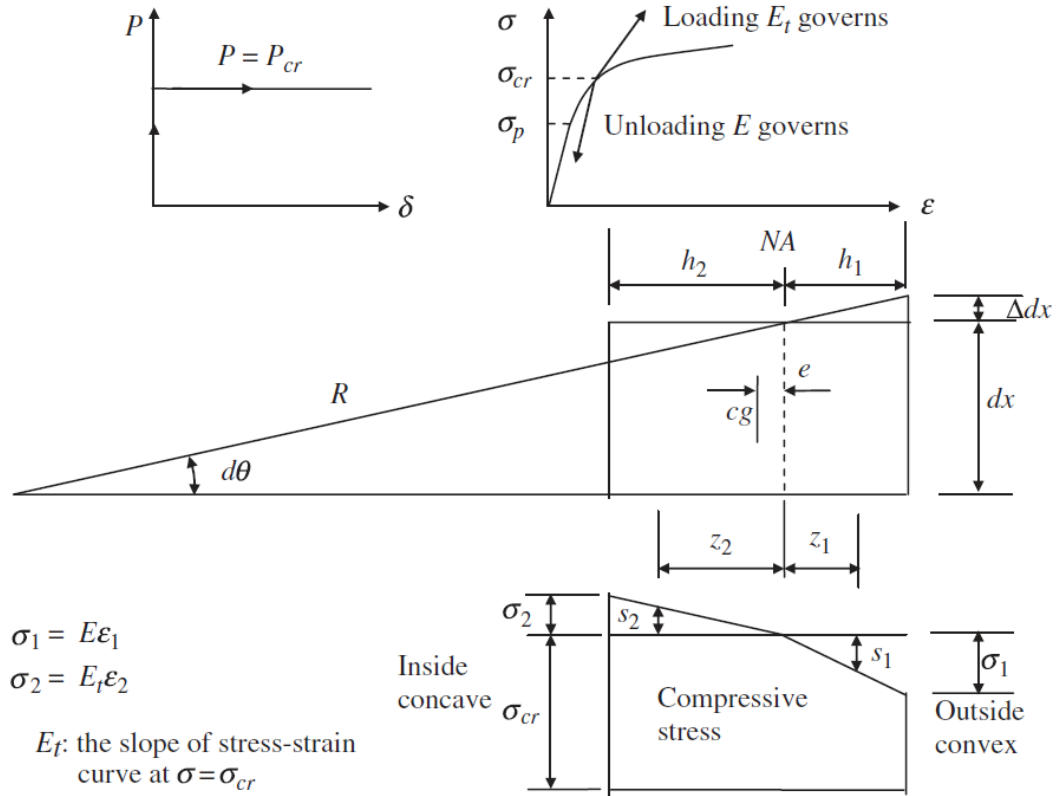


Figure 15. Reduced Modulus Model [12]

Small displacement theory proposes that the curvature of a bent column is:

$$\frac{1}{R} = \frac{d^2y}{dx^2} = \frac{d\theta}{dx} \quad (46)$$

$$\epsilon_1 = z_1 y'' \text{ and } \epsilon_2 = z_2 y'' \quad (47)$$

$$\sigma_1 = E h_1 y'' \text{ and } \sigma_2 = E_t h_2 y'' \quad (48)$$

$$s_1 = E z_1 y'' (\text{tension}) \text{ and } s_2 = E_t z_2 y'' (\text{comp.}) \quad (49)$$

In pure bending;

$$\int_0^{h_1} s_1 dA + \int_0^{h_2} s_2 dA = 0 \quad (50)$$

$$E y'' \int_0^{h_1} z_1 dA + E_t y'' \int_0^{h_2} z_2 dA = 0 \quad (51)$$

$$Q_1 = \int_0^{h_1} z_1 dA \text{ and } Q_2 = \int_0^{h_2} z_2 dA \quad (52)$$

$$EQ_1 + E_t Q_2 = 0 \quad (53)$$

Equating the internal moment to external moment;

$$\int_0^{h_1} s_1 z_1 dA + \int_0^{h_2} s_2 z_2 dA = Py \quad (54)$$

$$y'' \left(E \int_0^{h_1} z_1^2 dA + E_t \int_0^{h_2} z_2^2 dA \right) = Py \quad (55)$$

$$I_1 = \int_0^{h_1} z_1^2 dA \text{ and } I_2 = \int_0^{h_2} z_2^2 dA \quad (56)$$

$$E_r = \frac{EI_1 + E_t I_2}{I} \quad (57)$$

Where, I_1 is the moment of inertia of the tension side, I_2 is the moment of inertia of the compression side, and E_r is the reduced modulus which depends on the stress-strain relationship of the material and the cross-section shape. By substituting equation (56) and (57) into equation (55), it takes the form:

$$E_r I y'' + Py = 0 \quad (58)$$

$$P_R = \frac{\pi^2 E_r I}{L^2} \quad (59)$$

$$\sigma cr = \frac{P_R}{A} = \frac{\pi^2 E_r}{\left(\frac{L}{r}\right)^2} = \frac{\pi^2 \tau_r E}{\left(\frac{L}{r}\right)^2} \text{ where } \tau_r = \frac{E_r}{E} < 1.0 \quad (60)$$

$$\tau_r = \tau \frac{I_2}{I} + \frac{I_1}{I} \quad (61)$$

$$(L/r)_{cr} = \pi \sqrt{\tau_r E / \sigma} \quad (62)$$

In a similar manner to tangent modulus procedure, column curves are constructed by using equation (62). First, $\sigma - \varepsilon$, then $\sigma - \tau$ diagrams are constructed. According to these diagrams, $\tau_r - \sigma$ diagram is obtained. Finally, $\sigma_r - (L/r)$ column curve is prepared.

As it can be seen from the above equations, reduced modulus takes into account both elastic and tangent moduli, as well as the cross-section properties. It should be noted that since reduced modulus E_r is greater than tangent modulus E_t , P_r will always be greater than P_t . [9]

2.1.3.3 Shanley's Model

Upon a large amount of tests on small aluminum columns, Shanley developed a model to explain the dilemma of tangent modulus and reduced modulus test results, as explained in the previous sections. He concluded that the column starts to deflect very near to the tangent modulus range but it carries the load without buckling until the reduced modulus range.

Shanley's column model consists of two rigid bars connected to each other at the center by a deformable cell which consists of two flanges of area $A/2$ and a zero-area web. All of the deformations occur in this deformable cell. The flanges of the cell are such that one is elastic with modulus E_1 , and the other is a material with modulus E_2 . In the deformed shape, as it can be seen from Figure 16, the following expressions are obtained.

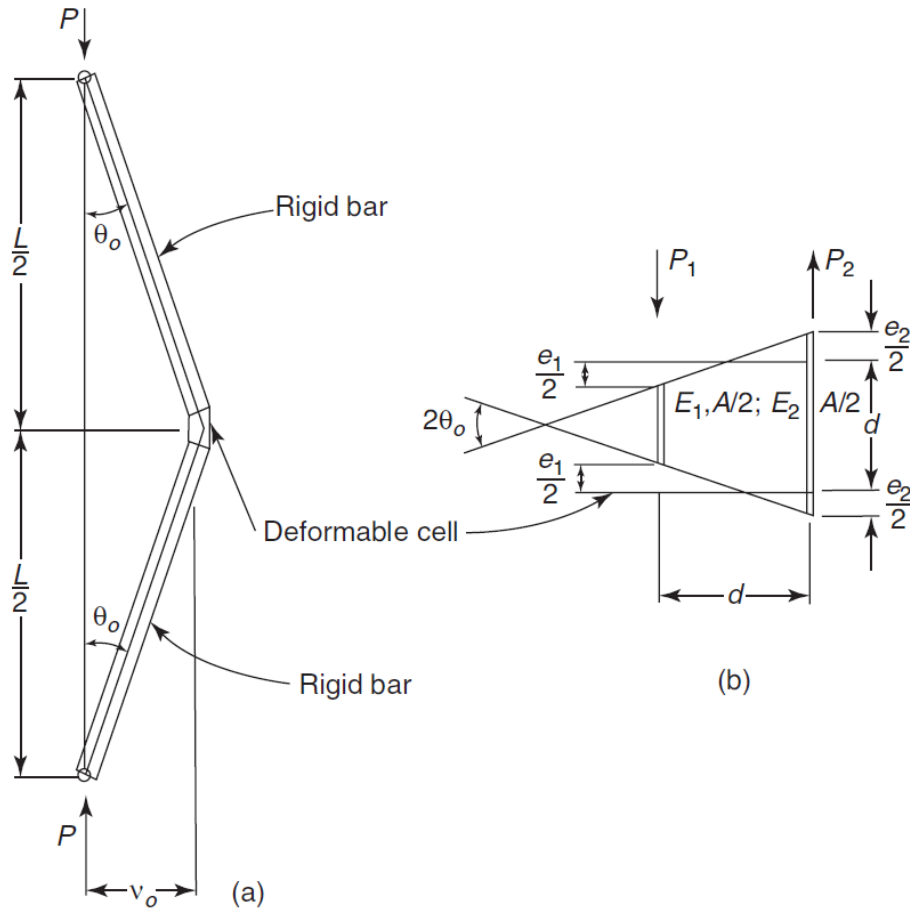


Figure 16. Shanley's column model [9]

$$y_o = \frac{\theta_o L}{2} \text{ and } \theta_o = \frac{(e_1 + e_2)}{2d} \quad (63)$$

$$y_o = \frac{(e_1 + e_2)L}{4d} \quad (64)$$

$$M_{ext} = Py_o = \frac{PL(e_1 + e_2)}{4d} \quad (65)$$

$$P_1 = \frac{E_1 e_1 A}{2d} \text{ and } P_2 = \frac{E_2 e_2 A}{2d} \quad (66)$$

$$M_{int} = \frac{d}{2}(P_1 + P_2) = \frac{A}{4}(E_1 e_1 + E_2 e_2) \quad (67)$$

From moment equilibrium;

$$M_{ext} = M_{int} \rightarrow P = \frac{Ad}{L} \left(\frac{E_1 e_1 + E_2 e_2}{e_1 + e_2} \right) \quad (68)$$

If the deformable case is elastic, then:

$$E_1 = E_2 = E \quad (69)$$

$$P_E = \frac{AE d}{L} \quad (70)$$

For the tangent modulus case:

$$E_1 = E_2 = E_t \quad (71)$$

$$P_T = \frac{AE_t d}{L} \quad (72)$$

When the elastic unloading is considered (for tension flange);

$$E_1 = E_t \text{ and } E_2 = E \quad (73)$$

$$P = \frac{Ad}{L} \left(\frac{E_t e_1 + E e_2}{e_1 + e_2} \right) \quad (74)$$

Recall from equation (44) that $\tau = \frac{E_t}{E}$.

$$P = P_T \left[1 + \frac{L e_1}{4 d y_o} \left(\frac{1}{\tau} - 1 \right) \right] \quad (75)$$

$$P = P_T + (P_1 - P_2) \quad (76)$$

Equation (76) shows that, the amount of load increase above load P_T is equal to the difference between the loads of two flanges. Equation (76) can be written in the form as:

$$P_1 - P_2 = \frac{AE_t}{2d} \left[\frac{4 d y_o}{L} - \left(1 + \frac{1}{\tau} \right) e_2 \right] \quad (77)$$

$$P = P_T \left[1 + \frac{2y_o}{d} - \frac{Le_2}{2d^2} \left(1 + \frac{1}{\tau} \right) \right] \quad (78)$$

$$P = P_T \left[1 + \frac{1}{\frac{d}{2y_o} + \frac{1+\tau}{1-\tau}} \right] \quad (79)$$

Equation (77) can be rewritten as $P_1 - P_2 = 0$ considering that according to the reduce modulus concept, reduced modulus load P_R is the load at which deflection occurs with no change in load.

$$0 = \frac{AE_t}{2d} \left[\frac{4dy_o}{L} - \left(1 + \frac{1}{\tau} \right) e_2 \right], \quad e_2 = \frac{4dy_o}{L} \left(\frac{1}{1 + \frac{1}{\tau}} \right) \quad (80)$$

By substituting equation (80) into equation (78);

$$P_R = P_T \left[1 + \left(\frac{1 - \tau}{1 + \tau} \right) \right] \quad (81)$$

Since $\tau = \frac{E_t}{E}$ depends on the strain in the column, the value of the load P also depends on strain. To illustrate the relationship between P and P_T , P/P_T versus y_o/d graph is constructed for an arbitrary value $\tau=0.5$ (Figure 17).

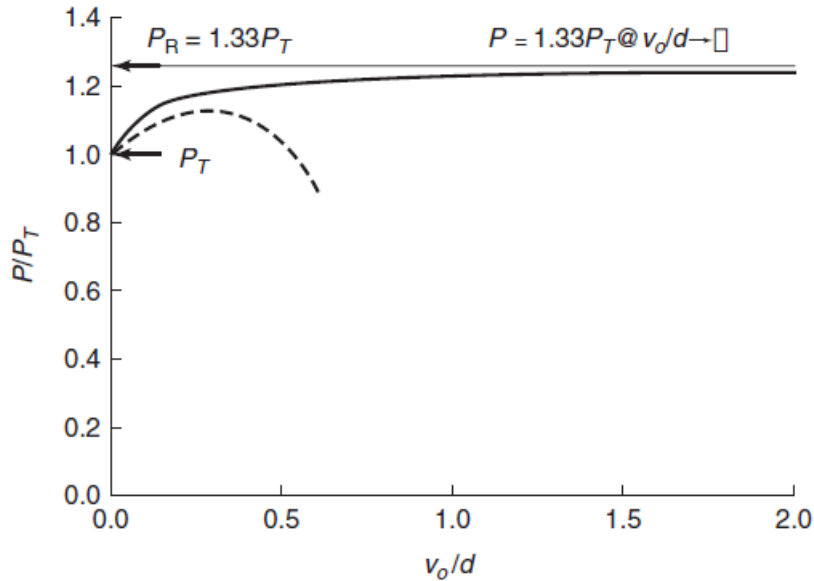


Figure 17. P/P_T versus y_o/d for an arbitrary value $\tau=0.5$ [9]

For an arbitrary value $\tau=0.5$, equation (81) becomes:

$$P_R = P_T * 1.333 \quad (82)$$

For y_0 value equal to zero, which means there is no deflection in the column yet, the load P is equal to P_T . In other words, until the column is disturbed with load P resulting in deflection y_0 at mid-height; the minimum critical buckling load is tangent modulus load. For any load greater than tangent modulus load, the equilibrium requires a deflection y_0 to be present. Moreover, after P_T is surpassed, the bending of the column proceeds with a deflection at compression side of the deformation cell. Therefore, τ is reduced further and P - y_0 curve reaches a peak below reduced modulus load P_R (See dashed-lined curve, Figure 17). When the deflection y_0 becomes infinitely large, the maximum load asymptotically reaches P_R (See solid-lined curve, Figure 17). This shows that for an inelastically buckling column, the maximum possible buckling load in theory is P_R . [9]

Even though Shanley's column model is not similar to a real-life column, the analysis results can be applied to real columns. The critical load of an inelastically buckling column will be between tangent modulus load and reduced modulus load. Any load below tangent modulus load does not disturb the straightness of a column. After tangent modulus load is surpassed, the buckling will occur inelastically where the buckling load cannot be greater than the reduced modulus load.

2.1.4 Empirical Column Formulae

Many researchers also focused on improving the column equation of Euler in the smaller slenderness ranges where the column is not behaving fully elastically. When the slenderness ratio of the column is relatively small, the yielding or crushing of the material may overcome the buckling. For this range, Euler buckling formula oversees the buckling load. Therefore, some empirical formulae are developed for the short to intermediate column ranges. Among these formulae, the most recognized ones are the Rankine's formula and Johnson's Linear and Parabolic formulae.

2.1.4.1 Rankine's Formula

Rankine's formula considers any range of column length. Where P_{Ra} is Rankine buckling load, P_{cr} is Euler buckling load and P_c is the crushing load of column:

$$\frac{1}{P_{Ra}} = \frac{1}{P_c} + \frac{1}{P_{cr}} = \frac{1}{\sigma_c * A} + \frac{L^2}{\pi^2 * EI} \quad (83)$$

For a short column, P_{cr} value is high; therefore, $1/P_{cr}$ value approaches to zero. This results in $P_{Ra} \cong P_u = \sigma_c * A$ which means that ultimate crushing load of column governs.

For a longer column, L^2 value is high resulting in $1/P_{cr}$ is much greater than $1/P_u$. Then, it can be considered that $P_{Ra} \cong P_{cr} = \frac{\pi^2 * EI}{L^2}$.

Rankine's formula can be rewritten as follows, where σ_u is the ultimate crushing stress and r is the radius of gyration:

$$P_{Ra} = \frac{\sigma_c * A}{1 + \frac{\sigma_c}{\pi^2 * EI} * \frac{A * L^2}{A * r^2}} = \frac{\sigma_c * A}{1 + a * \left(\frac{L}{r}\right)^2} \quad (84)$$

$$a = \frac{\sigma_c}{\pi^2 * E} \quad (85)$$

a is called Rankine's constant the value of which changes for different materials. The length L should be considered as effective length, depending on the end conditions. For a mild steel material, $\sigma_c = 330 \text{ MPa}$ and $a = 1/7500$. [15]

2.1.4.2 Johnson's Linear Formula

Johnson also worked on an experimental column formula. Based on experimental data, he observed that both Euler's formula and Rankine's formula were not very close to the actual buckling values for short to intermediate columns. This is caused mainly due to the following reasons:

- Euler formula ignored the effect of direct compression,
- In reality, load may not be applied perfectly as assumed,

- Even if it is assumed pin connections are frictionless, in actual case they are not perfectly frictionless,
- Also, in practice, it is not possible to fixate the ends as perfect pin and this creates errors,
- Columns in reality are not perfectly straight and homogeneous as Euler column in theory.

Thus, the difference between theory and actual case creates an error in results up to 5-10%. Johnson proposed the following empirical line formula based on allowable stress of column as well as slenderness ratio, where σ_{all} is the allowable stress and C is a constant depending on column materials. [15]

$$P_{J,linear} = A * \left[\sigma_{all} - C \left(\frac{L}{r} \right) \right] \quad (86)$$

For mild steel material, Johnson's straight line formula is as follows:

$$P_{J,linear} = A * \left[150 - 0.57 \left(\frac{L}{r} \right) \right] \quad (MPa) \quad (87)$$

2.1.4.3 Johnson's Parabolic Formula

After realizing that linear formula creates high errors, Johnson developed a parabolic formula with less error. [15]

$$P_{J,parabolic} = A * \left[\sigma_{all} - C \left(\frac{L}{r} \right)^2 \right] \quad (88)$$

$$C = \frac{\sigma_{all}^2}{4\pi^2 E} \quad (89)$$

$$P_{J,parabolic} = A * \sigma_{all} \left[1 - \frac{\sigma_{all} \left(\frac{L}{r} \right)^2}{4\pi^2 E} \right] \quad (90)$$

If the allowable stress in the formula is considered without any safety factors, it will be equal to the yield stress. Also, if the length is considered as effective length by including effective length k , the equation (90) can be rewritten as:

$$P_{J,parabolic} = A * \sigma_y \left[1 - \frac{\sigma_y \left(\frac{kL}{r} \right)^2}{4\pi^2 E} \right] \quad (91)$$

Johnson's Parabolic Formula can be used for short to intermediate columns. As the column gets more slender, Johnson formula will not depict the critical load correctly in that case, Euler equation governs. To determine the correct equation to use in case considering column length, column constant C_c can be calculated as follows:

$$C_c = \sqrt{\frac{2\pi^2 E}{\sigma_y}} \quad (92)$$

Column constant C_c is basically a slenderness ratio determining the limit at which the column buckles – closer to Euler load or Johnson load. If slenderness ratio of the column is smaller than C_c , then the critical load should be calculated with Johnson's formula. For column slenderness greater than C_c , column will be completely in the elastic range and Euler buckling load will govern.

The relationship between the column length and critical buckling load can be understood better from the graphical description of Euler load and Johnson parabola. Figure 14 below shows the column buckling limits for S235 quality steel.

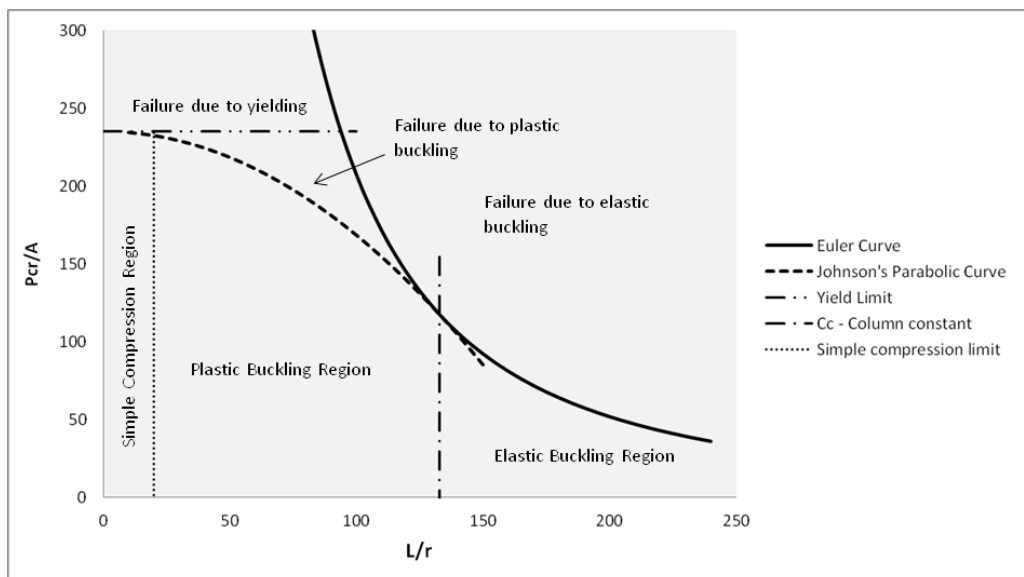


Figure 18. Column failure lines

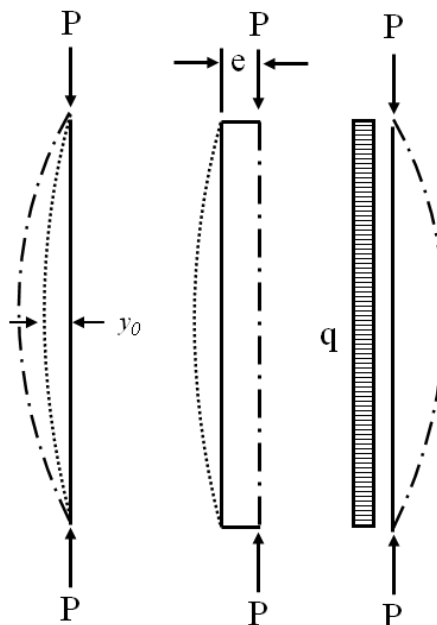
As it can be seen from Figure 18, Euler curve is not conservative anymore for slenderness ratios smaller than 132 for S235 quality steel material. Below this range, Johnson parabola governs up to yield limit and it can be used for intermediate columns. For short columns with slenderness ratio smaller than 20, failure will be due to yielding under simple compression.

2.1.5 Initial Imperfections

Euler's column formulas are based on the assumption that the column is initially perfect. However, in real life, no column is perfect. The imperfections in a column due to hot rolling, welding, transportation or any other reason are always expected as long as these imperfections are in the limit of specified tolerances in design codes/specifications. Moreover, while loading the column, small eccentricities might exist, as well.

There are basically three types of effects causing the Euler column to be “imperfect”, as it is also illustrated in Figure 19:

- Small initial out-of-straightness of column profile
- Small eccentricities in loading
- Small lateral loads



i) Initial eccentricity ii) Eccentric loading iii) Lateral load

Figure 19. Initial imperfections of a column [9]

2.1.5.1 Small Initial Out-of-Straightness of Column Profile

Recall that the column buckling curve is a half-sine wave shape. If it is assumed that the shape of the initial imperfections are also in the half-sine wave form, then, the initial shape function for the first mode can be expressed as:

$$y_i = y_o * \sin \frac{\pi x}{L} \quad (93)$$

While internal moment does not change, external moment is increased due to additional deflection. By equating internal and external moments, the differential equation can be written as in the below form.

$$M_{int} = EI * y'', \quad M_{ext} = P * (y_i + y) \quad (94)$$

$$EI * y'' + P * y = -P * y_i \quad (95)$$

$$y'' + \frac{P}{EI} * y = -P * y_i \quad (96)$$

For $k^2 = P/EI$;

$$y'' + k^2 * y = -P * y_i \quad (97)$$

This time the solution of the differential equation is not homogeneous unlike perfect Euler column solution. The homogeneous part of the solution is the same as equation (17) and the particular solution is introduced as: $y_p = C \cos kx + D \sin kx$

After solving the differential equation in the same manner with a perfect column, and applying the boundary conditions for pin-ended column (see Table 1), the solution becomes and the constants are obtained as:

$$y = A \cos kx + B \sin kx + C \cos kx + D \sin kx \quad (98)$$

$$C = 0, \quad D = -\frac{k^2 * y_o}{k^2 - \pi^2/L^2} \quad (99)$$

$$y_p = -\frac{k^2 * y_o}{k^2 - \pi^2/L^2} \sin \frac{kx}{L} \quad (100)$$

Then, the solution of the whole equation becomes:

$$y = A \cos kx + B \sin kx - \frac{k^2 * y_o}{k^2 - \pi^2/L^2} \sin \frac{kx}{L} \quad (101)$$

Recall that, the solution of the Euler column in the first mode is $P_E = \pi^2 EI/L^2$ and $k^2 = P/EI$. Then, after substituting these two equations into equation (101) and arranging the formula accordingly:

$$y = A \cos kx + B \sin kx + \frac{y_o + P/P_E}{1 - P/P_E} \sin \frac{kx}{L} \quad (102)$$

Substituting boundary conditions $x = 0$ at $y = 0$, $x = L$ at $y = 0$, the constants A and B are obtained as zero. Then, equation (102) becomes:

$$y = \frac{y_o + P/P_E}{1 - P/P_E} \sin \frac{kx}{L} \quad (103)$$

$$y_{total} = y + y_i = \frac{y_o * \sin \frac{\pi x}{L}}{1 - P/P_E} \quad (104)$$

The imperfections play an important role especially when P/P_E ratio approaches to 1, i.e. additional load due to imperfection is very close to the critical load. Yet, it is impossible to construct a column perfectly as assumed in the Euler formulas. However, codes and design specifications limit the initial imperfections in a column or propose reduction factors to take into account initial imperfections. [9]

2.1.5.2 Small Eccentricities in Loading

When there is a small eccentricity in loading, the external moment term in equation is increased by $P * e$. [9]

$$EI * y'' + P * (y + e) = 0 \quad (105)$$

$$y'' + \frac{P}{EI} * (y + e) = 0 \quad (106)$$

$$y'' + k^2 * (y + e) = 0 \quad (107)$$

The general solution applied to this homogeneous second order differential equation is $y = A \cos kx + B \sin kx - e$ with boundary conditions same as the perfect column case, $x = 0$ at $y = 0$, $x = L$ at $y = 0$. Then, the solution takes the form of:

$$y = e * \left(\cos kx + \frac{1 - \cos kL}{\sin kL} \sin kx - 1 \right) \quad (108)$$

2.1.5.3 Small Lateral Load

Even though small lateral load applied to a column is not necessarily an imperfection, the behavior in small lateral load case is similar to the cases considered in 2.1.4.1 and 2.1.4.2. [9] The general formula used in equation (31) can be rearranged as:

$$(y'')'' + k^2 y'' = q/EI \quad (109)$$

$$y = A + Bx + C \cos kx + D \sin kx + \frac{qx^2}{2P} \quad (110)$$

Boundary conditions are: $y = 0$ at $x = 0$ and $x = L$, $y'' = 0$ at $x = 0$ and $x = L$

$$y = \frac{q}{Pk^2} \left[\left(\frac{1 - \cos kx}{\sin kx} \right) \sin kx + \cos kx + \frac{kx^2}{2} - \frac{k^2 Lx}{2} - 1 \right] \quad (111)$$

2.1.5.4 Magnification Factor for Initial Imperfection

The maximum deflections at the column mid-length for the three imperfection cases are obtained by substituting $L/2$ for x in equations (104), (108) and (111). Then, these maximum deflections are compared with the respective deflection formulas for each case to obtain magnification factors applied to the column due to imperfections.

Small initial out-of-straightness:

$$y_{L/2} = \frac{y_o}{1 - P/P_E} \quad (112)$$

$$MF = \frac{y_{total,L/2}}{y_o} = \frac{1}{1 - P/P_E} \quad (113)$$

Small eccentricities in loading:

$$y_{L/2} = e * \left(\frac{1 - \cos kL}{\cos kL} \right) \quad (114)$$

This case can be considered as beam with end moments. Therefore, the magnification factor is obtained by dividing the maximum deflection in equation (112) with beam deflection at mid-point for beam with end moments.

$$y, b_{L/2} = \frac{ML^2}{8EI} = \frac{PeL^2}{8EI} = \frac{Pe}{8P_E/\pi^2} = \frac{\left(\frac{P}{P_E}\right)e\pi^2}{8} \quad (115)$$

$$MF = \frac{e \left(\frac{1 - \cos kL}{\cos kL} \right)}{\frac{\left(\frac{P}{P_E}\right)e\pi^2}{8}} = \frac{8}{\pi^2(P/P_E)} \left[\frac{1 - \cos \frac{\pi}{2} \sqrt{\left(\frac{P}{P_E}\right)}}{\cos \frac{\pi}{2} \sqrt{\left(\frac{P}{P_E}\right)}} \right] \quad (116)$$

Small lateral load:

$$y_{L/2} = \frac{q}{Pk^2} \left[\left(\frac{1}{\cos \frac{kL}{2}} \right) - \frac{(kL)^2}{8} - 1 \right] \quad (117)$$

This case is considered as beam with distributed loading. Thus, the magnification factor is obtained by dividing the maximum deflection in equation (117) with beam deflection at mid-point for beam with distributed loading.

$$y, b_{L/2} = \frac{5qL^4}{384EI} \quad (118)$$

$$MF = \frac{384}{5L^4k^4} \left[\left(\frac{1}{\cos \frac{kL}{2}} \right) - \frac{(kL)^2}{8} - 1 \right] \quad (119)$$

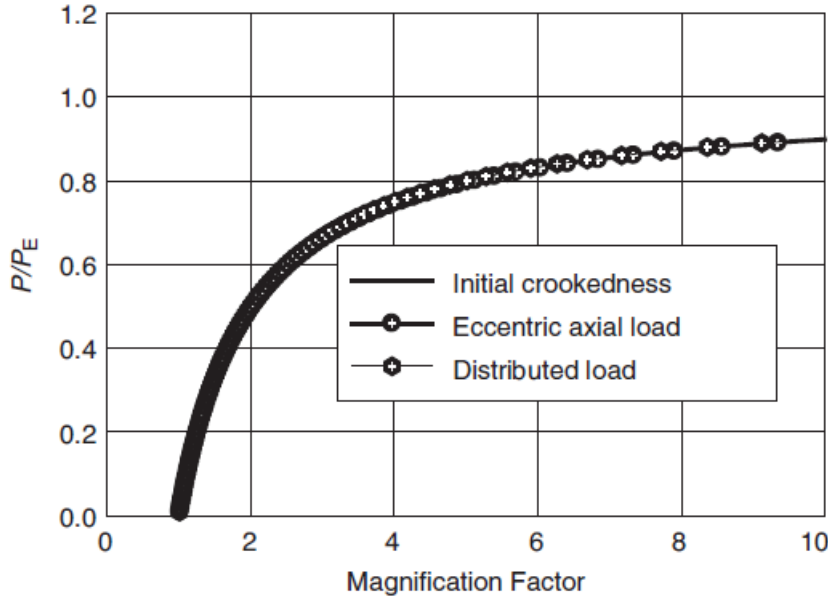


Figure 20. Magnification factors for imperfection cases [9]

When the magnification factors for all three cases are plotted against P/P_E , it is seen that all curves coincide with each other in Figure 20. In the light of this information, the magnification factor for the first case, small initial out-of-straightness, can be used as a governing factor since it is simplest of all. [9]

2.2 SENSOR WORKING PRINCIPLES FROM LITERATURE

Information on strain gauges will be given first for better understanding of working principles of the buckling sensor.

2.2.1 Strain Gauge Working Principles

Strain gauges are the most common strain measurement sensors used widely all around the world. This post stamp sized simple sensor is used in a variety of areas for structural health monitoring.

The invention of the strain gauges go back to 1938 when Simmons from California Institute of Technology and Ruge from Massachusetts Institute of Technology,

independent from each other, discovered that thin wire bonded to a surface was actually reacting to the strain of the studied surface. The bonded resistance wire strain gauge progression advanced from early 1940s to 1950s by the first strain gauge manufacturer BLH. In mid-1950s, development of foil strain gauge started. Upon evolution along these years, now there is a whole industry founded on strain gauges. [16]

Today, the most widely used strain gauge type is electric resistance foil type. There are several other types of strain gauges such as semiconductor type, capacitive type and vibrating wire type. In this thesis, the foil type electrical resistance strain gauge will be investigated and also used in the lab tests which will be studied in 2.2.1.

The main working principle of electric resistance strain gauges is based on the change in length of wire or foil due to the deformation (due to bending, axial tension or compression, etc.) of the bonded member. When the foil (or wire, depending on the gauge type) elongates, its cross-sectional area decreases and electrical resistance increases. Likewise, when the foil shortens, its cross-sectional area increases and electrical resistance decreases (Figure 21). As long as these stresses in the foil due to elongation and shortening are kept within the elastic limits of the foil material, the foil can work as a measuring tool for physical strain. The change in electrical resistance in the foil can be measured by help of a circuit, which will be investigated in section 2.2.2.

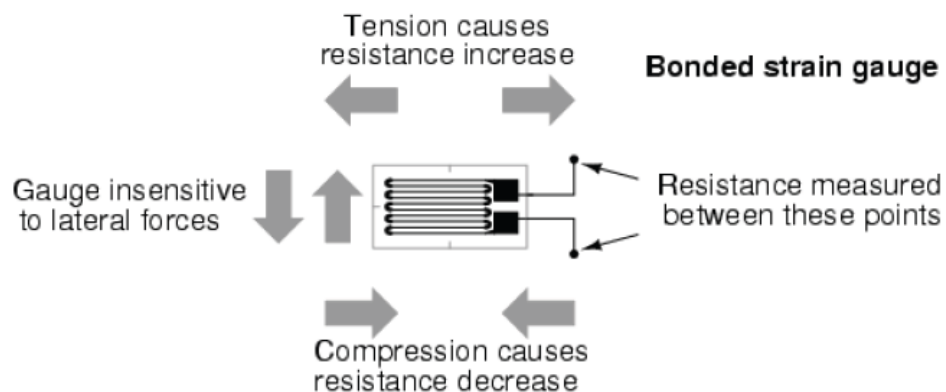


Figure 21. Working principle of strain gauge [17]

The relationship between the resistance change and strain of the foil (or wire) is given in the following equations; where, ρ is the resistivity, A is the cross-sectional

area of the foil, L is the initial length of the foil, R is the initial resistance of the foil, and μ is the Poisson's Ratio which is 0.3 for most metals.

$$R = \frac{\rho L}{A} \quad (120)$$

$$GF = \frac{\Delta R/R}{\Delta L/L} = \frac{\Delta \rho/\rho}{\Delta L/L} + (1 + 2\mu) \quad (121)$$

Equation (121) gives the gauge factor of a strain gauge. Gauge factor value depends on the metal alloy used in the foil (or wire) construction. The metal alloys used as strain gauge foil the most often are nickel alloys Constantan, Iso-elastic, and Karma with gauge factors +2.0, +3.5, and +2.1, respectively. [18]

When equation (121) is considered, it should be noted that, if the own resistivity ρ of the material did not change with strain, then the equation will result as $1 + 2\mu$ which is equal to $1 + 2(0.3) = 1.6$ for most metals. However, the real value for gauge factor is obtained as equal to or greater than +2.0 which shows that the own resistivity of the metal also contributes to the gauge factor. [19]

2.2.1.1 Strain Gauge Construction and Terminology

Foil construction strain gauges are composed of thin foils (about 0.1 mm thickness), lead wires connecting to the foils and backing material from epoxy, plastic etc. to hold the very fragile foil in place, as illustrated in Figure 22. The backing material also supports the foil laterally so that it can shorten without buckling. This way, compressive strains can also be measured with ease by using strain gauges. [18] The lead wires connected to the end of the foil strips are used to measure the resistance of the gauge.

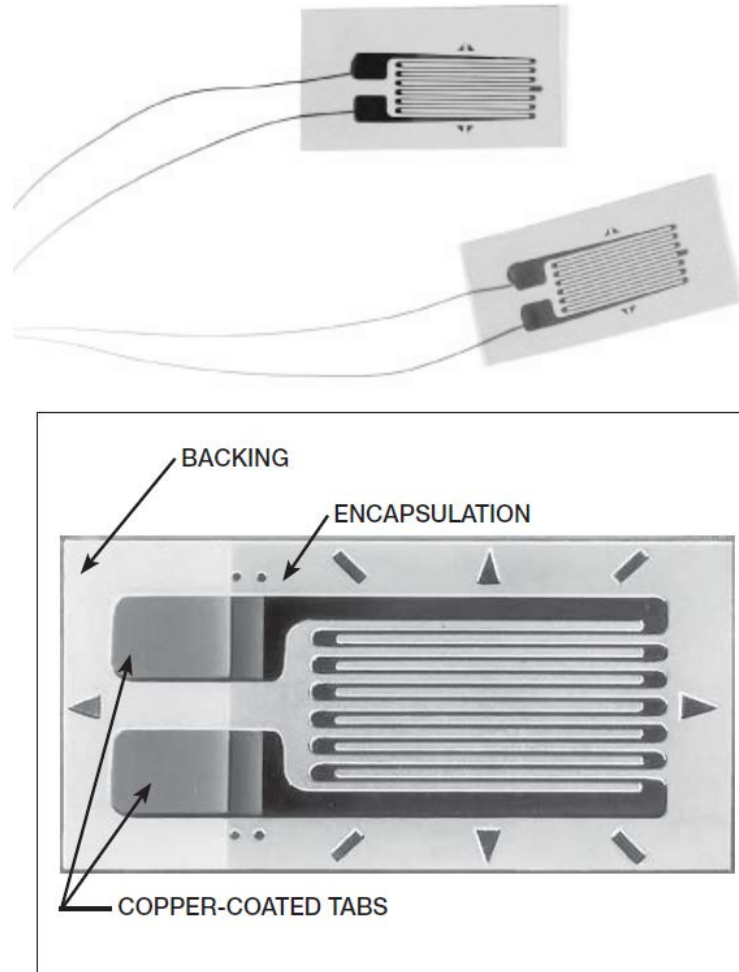


Figure 22. Strain gauge construction close-up [17]

As all sensors, strain gauges have characteristic values that affect the measurements. These characteristics are related with the response of sensor output due to a change in input, selectiveness of the sensor in producing an output, and stability of the system during measurement. The most important characteristics of a strain gauge are explained as following. [20]

Accuracy is the correctness of the output compared to the actual value it should measure, e.g. if actual strain is $200\mu\epsilon$, the strain gauge with an output of $203\mu\epsilon$ is more accurate than the strain gauge with an output of $210\mu\epsilon$.

Precision is the ability of the strain gauge to give the same output in different measurements of the same subject, e.g. for an actual strain value of $200\mu\epsilon$, if a strain gauge outputs are $202\mu\epsilon$, $199\mu\epsilon$, $204\mu\epsilon$ in repetitive measurement, and another strain gauge outputs are $205\mu\epsilon$, $220\mu\epsilon$, $190\mu\epsilon$, the first strain gauge has higher precision

and higher accuracy. If the measurements of the strain gauge are $208\mu\epsilon$, $209\mu\epsilon$, $210\mu\epsilon$, it means the gauge has high precision and low accuracy. The difference between accuracy and precision is also illustrated in Figure 23

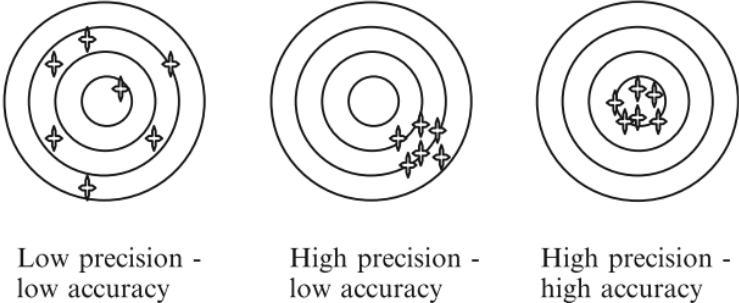


Figure 23. Difference between accuracy and precision [20]

Sensitivity is can be described as the minimum output value which can be observed for a unit disturbance, e.g. for a strain gauge with 10 mV/V sensitivity, 10 mV of output can be obtained per volt of excitation voltage.

Resolution is the smallest detectable change in measurement which can produce a detectable increase in output value.

Range of a strain gauge is the values spanning between the maximum and the minimum output values which can be measured. Any value outside of this range may cause unintelligible readings or even harm the gauge.

Noise is described as the undesirable fluctuations in the output even though the measured subject is not changing. Its source might be internal or external. Examples to external noise sources are signals produced by transmission and reception circuits as well as power supplies, mechanical vibrations, changes in the environment temperature, etc. External noise causes systematic errors. On the other hand, internal noise sources are more complicated such as random variations of current or voltage in sensor systems which is called electronic noise, thermal disturbance of careers named as thermal noise, and pink noise, of which the interfering signals are stronger at lower frequencies.

2.2.1.2 Strain Gauge Installation

The strain gauge is glued to the element to be tested by the help of a bonding material. Foil gauges have the advantage of easy bonding compared to wire gauges since they have a flat structure. The bonding and installation of strain gauges is a very delicate procedure, and if it is not executed properly, the measurement results might be incorrect. In order to manage an acceptable bonding, the steps below should be followed, which are also illustrated in Figure 24:

- First, the surface on which the strain gauge will be glued should be smoothed with either sandpaper or for more rough surfaces a stronger tool such as sharpening stone. The material residues should be cleaned off the surface after smoothing is completed.
- Then, the area of bonding should be thoroughly cleaned with proper chemicals such as acetone.
- Before directly bonding, the strain gauge first should be correctly positioned on the surface, for correct measurement. The positioning can be done by using a duct tape piece. The sticky surface of the duct tape can be made slightly rougher by touching, in order to decrease the adhesion strength of the tape. This is necessary so as not to damage the strain gauge while pulling of the tape after bonding material is applied.
- After the strain gauge is correctly positioned, the adhesive can be applied. The application of the adhesive should be done very carefully; a small drop of adhesive should be applied and spread delicately under the strain gauge without overflowing.
- After the correct amount of adhesive is applied and spread, for proper and strong bonding, the strain gauge should be pressed upon for fixing it to the surface. While pressing on the strain gauge, it is also important to not harm the strain gauge by pushing too hard onto the surface.
- When the bonding is completed, the duct tape can be slowly and carefully removed. If the adhesive is not yet dried and bonded so well, or if the duct tape is not roughened and bonded to the strain gauge too much, while removing the tape, the strain gauge may also be removed from the surface.

Moreover, even though the strain gauge is correctly bonded and held on place while removing the tape, the lead wires connected to the strain gauge may come off if the tape is pulled hardly.

- The strain gauge is ready to use after removing the duct tape correctly. However, the lead wires which will be used to measure the resistance difference in the gauge should be fixed on to the surface. The wires should be soldered or spot-welded to a terminal (which is also glued in front of the strain gauge in the same manner) and the excess length of wires can be cut off. The terminal ends will be connected with the data acquisition system. If the soldering of the wires to the terminal is not done properly, during testing, wires may detach from the surface and measurement cannot be done.
- If necessary, after cabling is finished, the measurement point can be covered for protecting the strain gauge and wires. This may especially be necessary if there is moisture that can cause corrosion in the test environment.

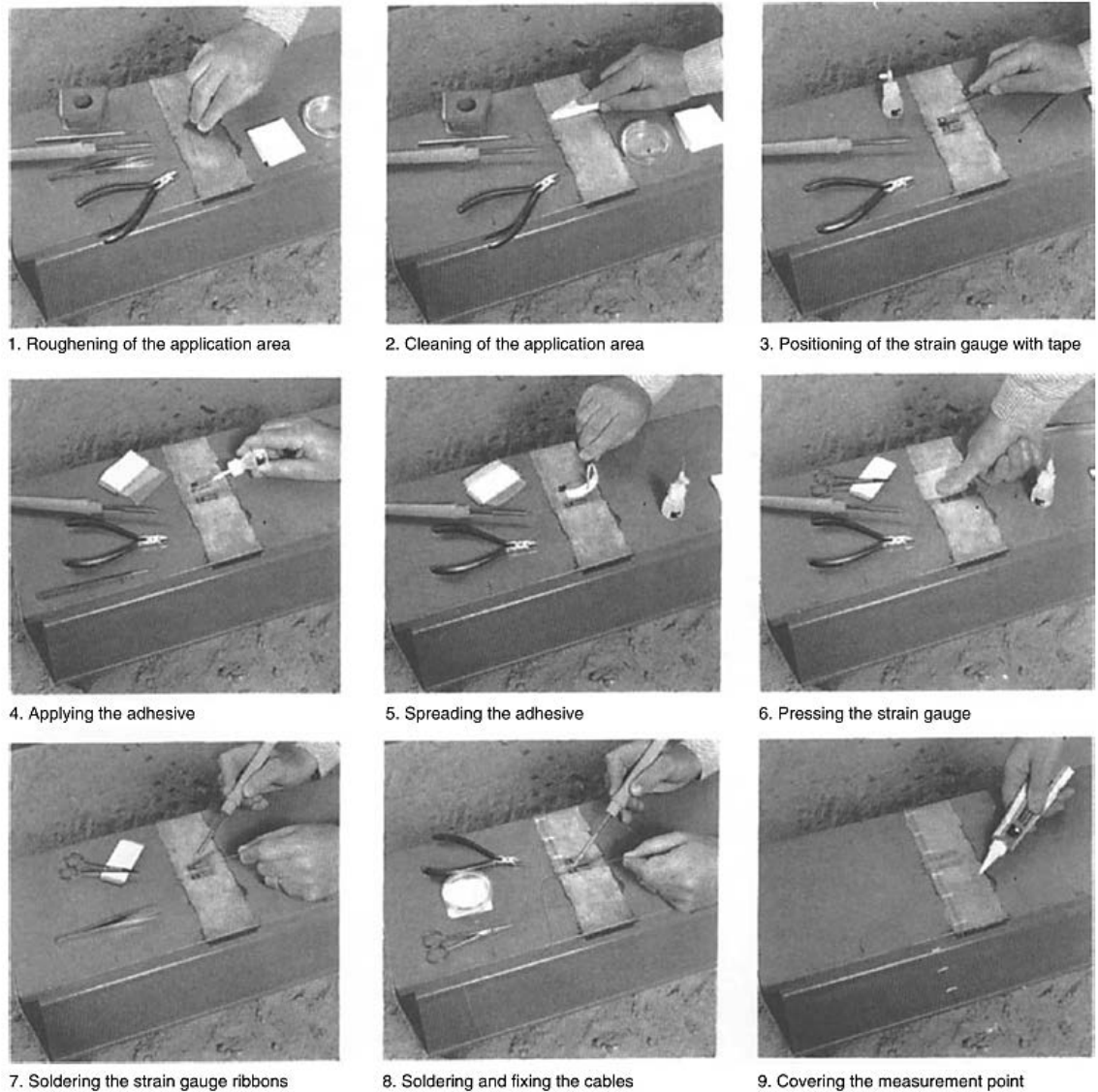


Figure 24. Strain gauge installation [19]

2.2.2 Wheatstone Bridge

A typical strain gauge resistance ranges between 30Ω and 3000Ω in unstressed state. In the elastic limits, the possible changes in resistance is very small; and if it is intended to obtain greater resistance changes, this time it might deform the gauge and the test specimen permanently. Therefore, for a greater measurement range, generally amplification is required. To amplify the strain measurements, a bridge circuit can be used.

A bridge electrical circuit is set up such that its two parallel branches are linked by a third branch at an intermediate point. Wheatstone bridge is the most commonly used bridge circuit consisting of four resistors where two parallel branches of resistors connected intermediately. See Figure 25 for figurative description of Wheatstone bridge.

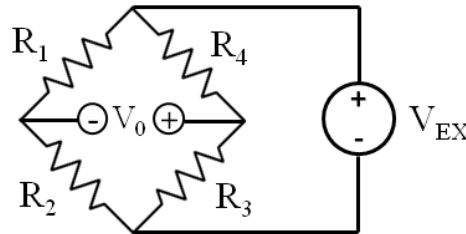


Figure 25. Wheatstone bridge circuit

Bridge output voltage can be calculated as:

$$V_O = V_{Ex} * \left(\frac{\Delta R_1}{R_1} - \frac{\Delta R_2}{R_2} + \frac{\Delta R_3}{R_3} - \frac{\Delta R_4}{R_4} \right) \quad (122)$$

Where, V_O is output voltage and V_{Ex} is excitation voltage given to the system. By substituting equation (121) into (122), equation (122) can be expressed in terms of strain:

$$V_O = V_{Ex} * \frac{GF}{4} * \left(\frac{\Delta \epsilon_1}{\epsilon_1} - \frac{\Delta \epsilon_2}{\epsilon_2} + \frac{\Delta \epsilon_3}{\epsilon_3} - \frac{\Delta \epsilon_4}{\epsilon_4} \right) \quad (123)$$

In Figure 20, if no force is applied on the system, the strain gauges will be unstressed and the system will be in equilibrium, i.e. output voltage V_O will indicate zero voltage. As the system is applied a force, the gauges will be compressed or stretched and the resistance values of the gauges will change. Since input voltage is known and the output voltage value can be read, the change in the resistances of strain gauges will indicate the strain in the element tested. So, basically, Wheatstone bridge makes use of the tendency of the circuit to balance each leg for measuring an unknown resistance.

Wheatstone bridge can be constituted with one, two or four active gauges. If all of the resistances in Wheatstone bridge are strain gauges, then it is a *full-bridge*. If two

consecutive resistances (R_1 and R_3 or R_2 and R_4) are strain gauges and the other two are normal resistors to complete the bridge, then it is called a *half-bridge*. If only one of the resistances is an active strain gauge with three resistors to complete the bridge, then it is a *quarter-bridge*. See Figure 26 for description.

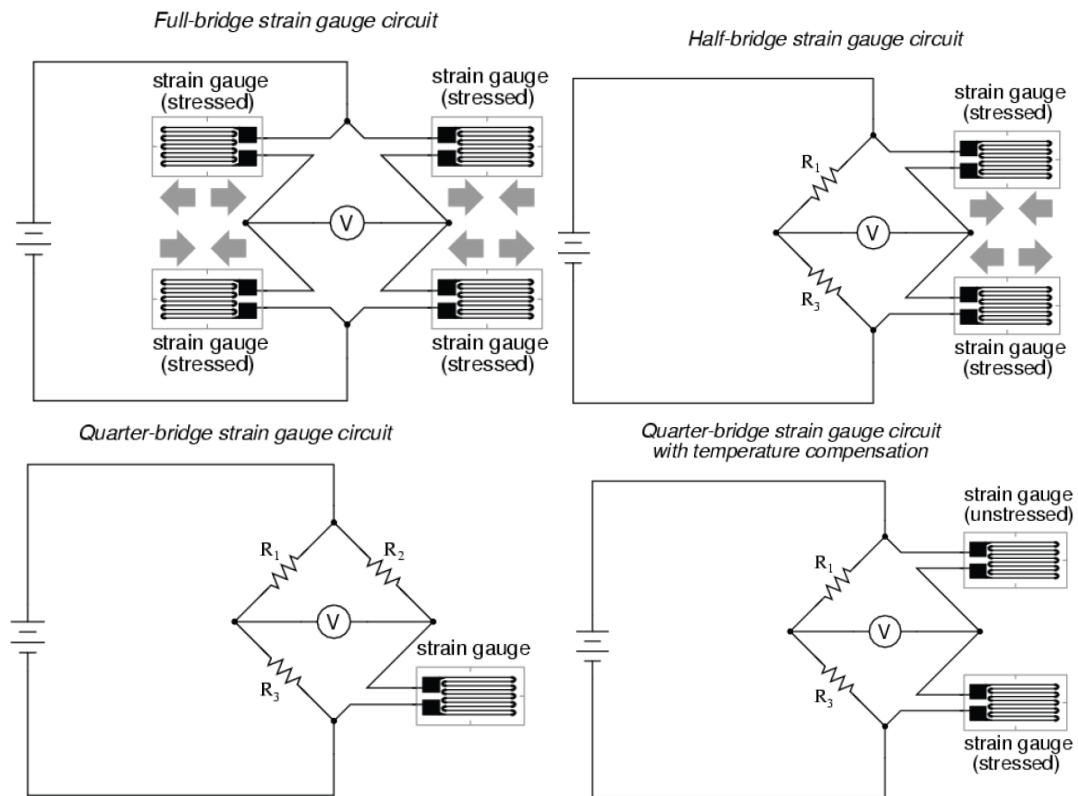


Figure 26. Wheatstone bridge alternatives [17]

The type of the bridge configuration to be chosen is related with several aspects. For instance, a quarter-bridge may not be efficient when thermal strains exist. For temperature compensation, at least two active strains should exist in the bridge.

The strain gauges are sensitive to temperature changes as well due to their metallic construction. If there is also a thermal change in the environment that the strain gauge is being used; additional to the mechanical strain measured, there will also be thermal strain which is called “apparent strain”. [18] Since a strain gauge directly gives one strain output, it is not possible to differentiate the mechanical strain from the thermal strain in such case. Thus, thermal effects cause an error in the strain measurements and should be compensated such that the actual value of the mechanical strain to be measured can be determined accurately. Temperature compensation can be achieved by using a bridge circuit instead of a single strain

gauge. In a bridge circuit, if there is another strain gauge at the adjacent arm of the active strain gauge, both of their measurements will include the thermal strain and their effects will cancel each other. This is possible in a half-bridge or a full-bridge. There is no way to cancel the temperature effect in a quarter-bridge unless a dummy strain gauge is included in the system.

For example, in a quarter-bridge compensation with a dummy resistor, there is an active strain gauge at R1, and a dummy strain gauge used for temperature compensation at R2, with strain outputs are ϵ_1 and ϵ_2 . Since both strain values include thermal strains ϵ_1^T and ϵ_2^T as well, equation (123) takes the following form:

$$\frac{V_O}{V_{Ex}} = \frac{GF}{4} (\epsilon_1 + \epsilon_1^T - \epsilon_2 - \epsilon_2^T) \quad (124)$$

Equal changes in adjacent arms of a Wheatstone bridge will cancel out. Since the environment and the material to be tested are the same for both gauges, values of ϵ_1^T and ϵ_2^T are the same, and will cancel each other out.

The type of bridge configuration to be used is not only related to temperature compensation, active strain gauge number will affect the output magnitude. With two strain gauges in adjacent arms (such as R1 and R3 active or R2 and R4 active), the output will be doubled. Therefore, half or full-bridges can be preferred for amplified output values.

The nature of the element tested and to which type of loading it is resisting also affects the strain gauge configuration. For instance, if an axial load carrying bar is tested, and there is no temperature based strains exist in the environment, a quarter-bridge will be enough for obtaining strain output. A half-bridge can be preferred for amplified output or temperature compensation. For a bending beam, since in the deformed configuration, one side will be in tension and one side in compression, a half-bridge will read opposite strain values (R1 and R2 or R3 and R4). To amplify these outputs, a full-bridge can be preferred. If it is needed, by placing the strain gauge in the transverse direction, elongation or contraction of the member can also be monitored. The most common cases for different Wheatstone bridge configurations are presented in the following Table 2.

Table 2. Different cases for Wheatstone bridge configurations

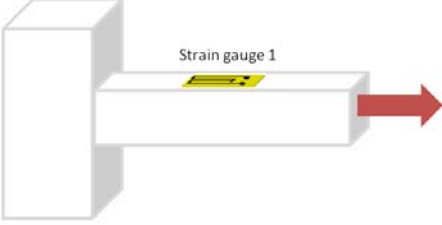
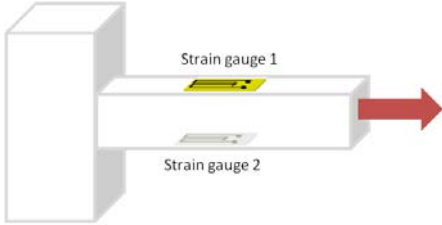
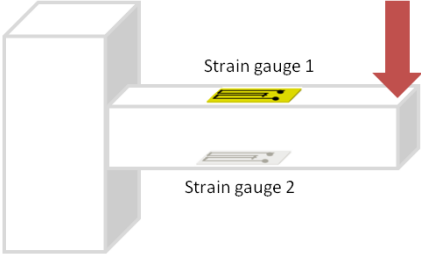
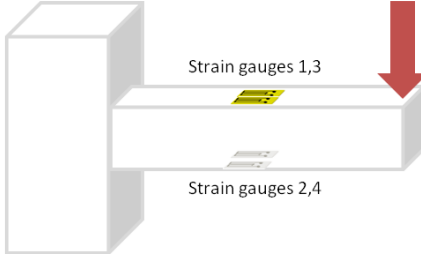
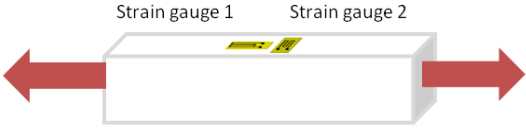
Bridge type	Loading type	Output
Quarter-bridge	<p style="text-align: center;">Axial tension or compression</p>  <p style="text-align: center;">Temperature compensation: No</p>	$\frac{V_o}{V_{Ex}} = \frac{GF}{4} (\epsilon_1)$ <p style="text-align: center;">Where,</p> $\epsilon_1 = +$
Quarter-bridge with dummy strain gauge or Half-bridge	<p style="text-align: center;">Axial tension or compression</p>  <p style="text-align: center;">Temperature compensation: Yes</p>	$\frac{V_o}{V_{Ex}} = \frac{GF}{4} (\epsilon_1 - \epsilon_2)$ <p style="text-align: center;">Where, in tension:</p> $\epsilon_1 = +, \epsilon_2 = +$ <p style="text-align: center;">In compression:</p> $\epsilon_1 = -, \epsilon_2 = -$
Half-bridge	<p style="text-align: center;">Bending beam</p>  <p style="text-align: center;">Temperature compensation: Yes</p>	$\frac{V_o}{V_{Ex}} = \frac{GF}{4} (\epsilon_1 - \epsilon_2)$ <p style="text-align: center;">Where,</p> $\epsilon_1 = +, \epsilon_2 = -$
Full-bridge	<p style="text-align: center;">Bending beam</p>  <p style="text-align: center;">Temperature compensation: Yes</p>	$\frac{V_o}{V_{Ex}} = \frac{GF}{4} (\epsilon_1 - \epsilon_2 + \epsilon_3 - \epsilon_4)$ <p style="text-align: center;">Where,</p> $\epsilon_1 = +, \epsilon_2 = -$ $\epsilon_3 = +, \epsilon_4 = -$

Table 2. (Continued)

Bridge type	Loading type	Output
Half-bridge	<p>Axial tension or compression</p>  <p>Temperature compensation: Yes</p>	$\frac{V_O}{V_{Ex}} = \frac{GF}{4} (\epsilon_1 - \mu\epsilon_1)$ <p>Where, in tension:</p> $\epsilon_1 = +, \epsilon_2 = -$ <p>In compression:</p> $\epsilon_1 = -, \epsilon_2 = +$

2.3 ANALYTICAL STUDIES FOR SENSOR DEVELOPMENT

To prove the strain gauges can monitor buckling deformations and critical loads, laboratory tests are conducted with both elastic and plastic buckling cases. The test setups and results are explained in detail in 2.4 and 2.5. In this section, the analytical studies conducted before preparing test setups are presented.

The laboratory tests are conducted with square hollow sections of dimensions 13.4x13.4x1.6 mm. The cross-sectional properties for this section are given as below.

Dimensions, $h = b = 13.4 \text{ mm}$, $t = 1.6 \text{ mm}$

Cross-sectional area, $A = 75.52 \text{ mm}^2$

Moment of inertia, $I = 1784.8 \text{ mm}^2$

Radius of gyration, $r = 4.86 \text{ mm}$

The theoretical elastic critical buckling load for this section with both ends pinned condition, are given as below.

Plastic buckling limit for S235 (St37) quality steel can be obtained by using the column constant equation as given by Johnson formula. If the slenderness ratio of a column is smaller than C_c value, then it is in the plastic limits.

$$C_c = \sqrt{\frac{2 * \pi^2 * E}{\sigma_y}} = \sqrt{\frac{2 * \pi^2 * 210000}{235}} = 131.4 \quad (125)$$

For a 1 meter of length, the slenderness ratio of the test profile 13.4x13.4x1.6 mm is given below.

$$\frac{kL}{r} = \frac{1.0 * 1000}{4.86} = 206 > C_c = 131.4 \quad (126)$$

The elastic buckling tests are conducted by using a 1 meter length of the considered profile, which is in the elastic buckling range. For this column, the elastic critical buckling load is calculated as:

$$P_{cr} = \frac{\pi^2 EI}{L^2} = \frac{\pi^2 * 210000 * 1784.8}{1000^2} = 3699 \text{ N} \quad (127)$$

For the plastic buckling case, the same profile with a smaller length will be used. It is seen that 400 mm of length is in the plastic buckling range, and also in the intermediate range as given in Johnson curve.

$$\frac{kL}{r} = \frac{1.0 * 400}{4.86} = 82 < C_c = 131.4 \quad (128)$$

For this case, the critical buckling load cannot be simply calculated from Euler buckling load as explained in detail in 2.1.3. The calculation of plastic buckling load should include the effects of tangent modulus and reduced modulus concepts. The plastic buckling load will be limited with tangent modulus load and reduced modulus load in the lower and upper bounds, respectively.

Before conducting tests, to approximate the buckling load for the plastic case, Johnson's formula for intermediate to short columns are used as a simpler approach. This is preferred due to its simplicity compared to constructing column curves for tangent and reduced modulus loads. Empirical Johnson formula directly calculates the buckling load for intermediate to short columns by taking into account the proportional limits of the column.

$$P_{cr} = A * \sigma_y \left[1 - \frac{\sigma_y \left(\frac{kL}{r} \right)^2}{4\pi^2 E} \right] = 75.52 * 235 \left[1 - \frac{235 \left(\frac{1.0 * 400}{4.86} \right)^2}{4\pi^2 * 210000} \right] \quad (129)$$

$$= 14340 \text{ N}$$

2.4 LABORATORY TESTS

Laboratory tests with buckling sensor consist of two separate test setups for elastic buckling case and plastic buckling case. Test setup preparation and steps followed in the tests for both cases are explained in detail in the following sections.

2.4.1 Elastic Buckling Test

Elastic buckling test is conducted with a S235 quality steel square hollow section of dimensions 13.4x13.4x1.6 mm, as also indicated in 2.3. About 1 meter length of this profile is used in the test. The tips of the profile are hammered and the tips are placed in the plates with welded horizontal guides for obtaining a closer result to the pin-pin end condition, see Figure 27. Due to this hammering, the actual unbraced length of the column measured from the un-hammered parts of the column ends as 920 mm. Therefore, the elastic critical buckling load for this actual unbraced length is modified as given in equation (130).

$$P_{cr} = \frac{\pi^2 EI}{L^2} = \frac{\pi^2 * 210000 * 1784.8}{920^2} = 4371 \text{ N} \quad (130)$$



Figure 27. Hammered tip of column and guide plates

Then, the strain gauges are installed on the column in half-bridge configuration. The gauge installation is conducted as described in 2.2.1.2 (see Figure 28). For the first

mode of buckling, strain gauges are placed at the mid-length of the column. The strain gauges used have $120\ \Omega$ resistances with a gauge factor of 2.0.

After strain gauges are installed and rested for a while for letting the glue get dry, the wiring of the strain gauges and passive resistors to the wiring panel, which can be seen in Figure 29, is conducted. For input voltage, a battery is used and the input voltage is supplied as 2.5 V.

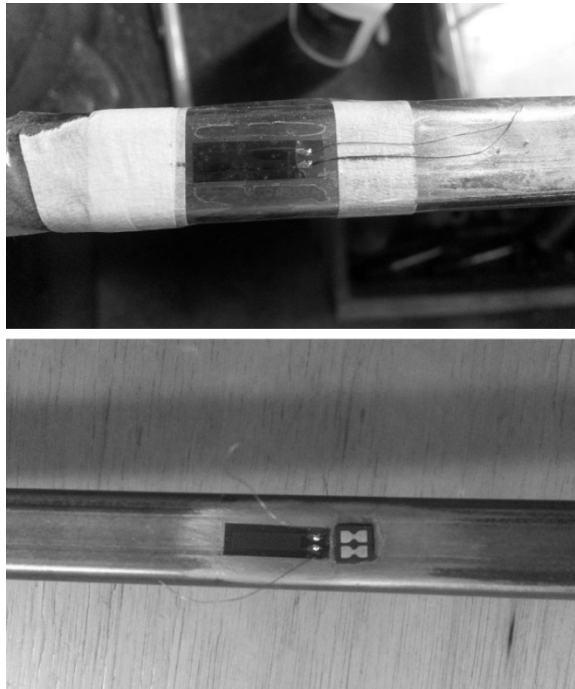


Figure 28. Strain gauge installation on the column

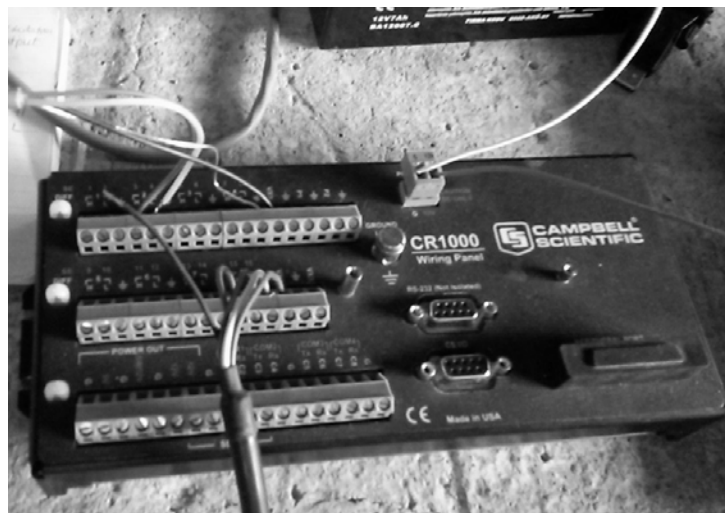


Figure 29. Wiring panel



Figure 30. Elastic buckling test setup

Finally, the setup is completed with a load cell and a hydraulic jack as seen in Figure 30. The 20-ton capacity load cell is also connected to the data acquisition system and

calibrated. A pancake type load cell is used for its easy adaptation to the test setup and high precision. Hydraulic jack used is a cylinder type with 10-tons capacity.

The loading and unloading is conducted with the hydraulic jack manually and compared with the load cell and strain gauge output data simultaneously from the computer that the test setup is connected. The column is loaded up to the theoretical buckling load calculated; however, actual buckling took place in a slightly higher load than the theoretical load. Possible reasons for this are explained in 2.5.

The column is unloaded and loaded again for several cycles and elastic buckling is observed each time. After each unloading phase, the column took its original shape. See Figure 31 for buckled shapes in two different cycles. The results for the test are presented in section 2.5.1.

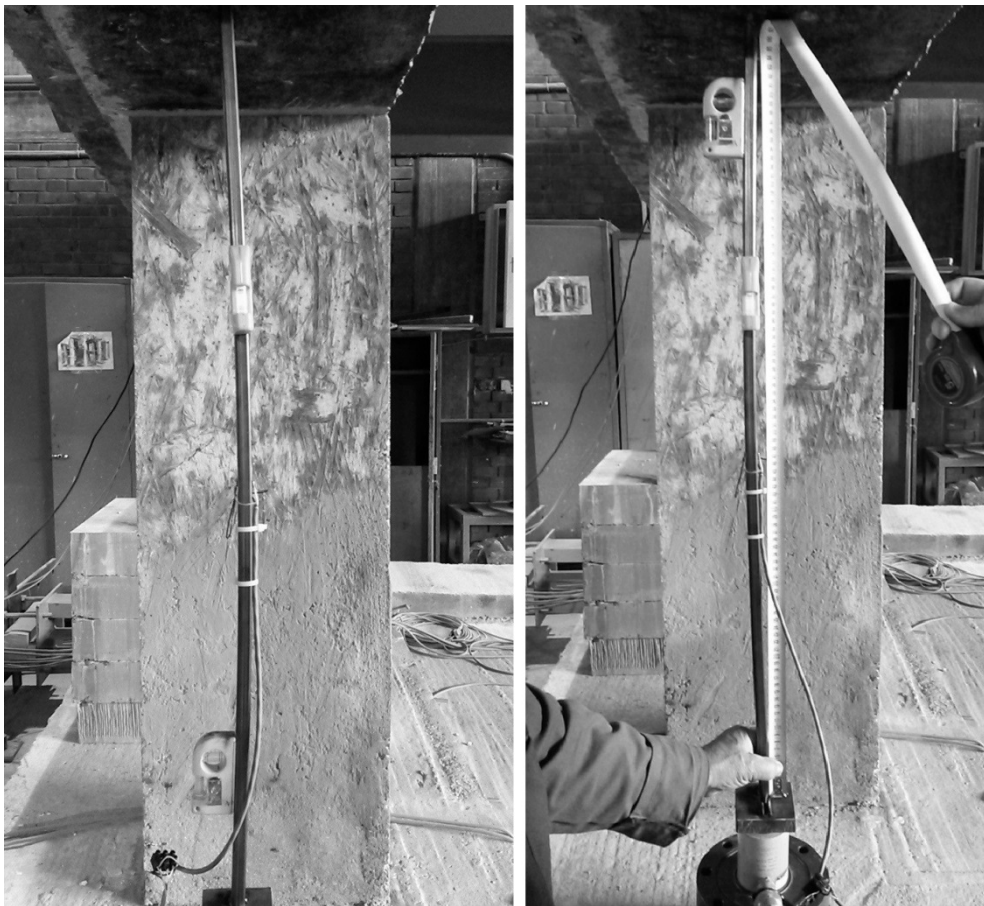


Figure 31. Elastically buckled column in two different cycles

2.4.2 Plastic Buckling Test

The plastic buckling case is conducted with a shorter column; the same profile with a 400 mm length is used. The same stages are followed for the strain gauge installation and preparation of the column ends for pin-pin connection in the test setup. The load cell and hydraulic jack from the previous test are used for this setup as well.

In this case, since the column length is smaller than the first setup, initially, the column is supported with a steel pedestal in the same spot that the first test is calculated as seen in Figure 32. However, after a trial, it is seen that the steel pedestal is not stable under the high loading.

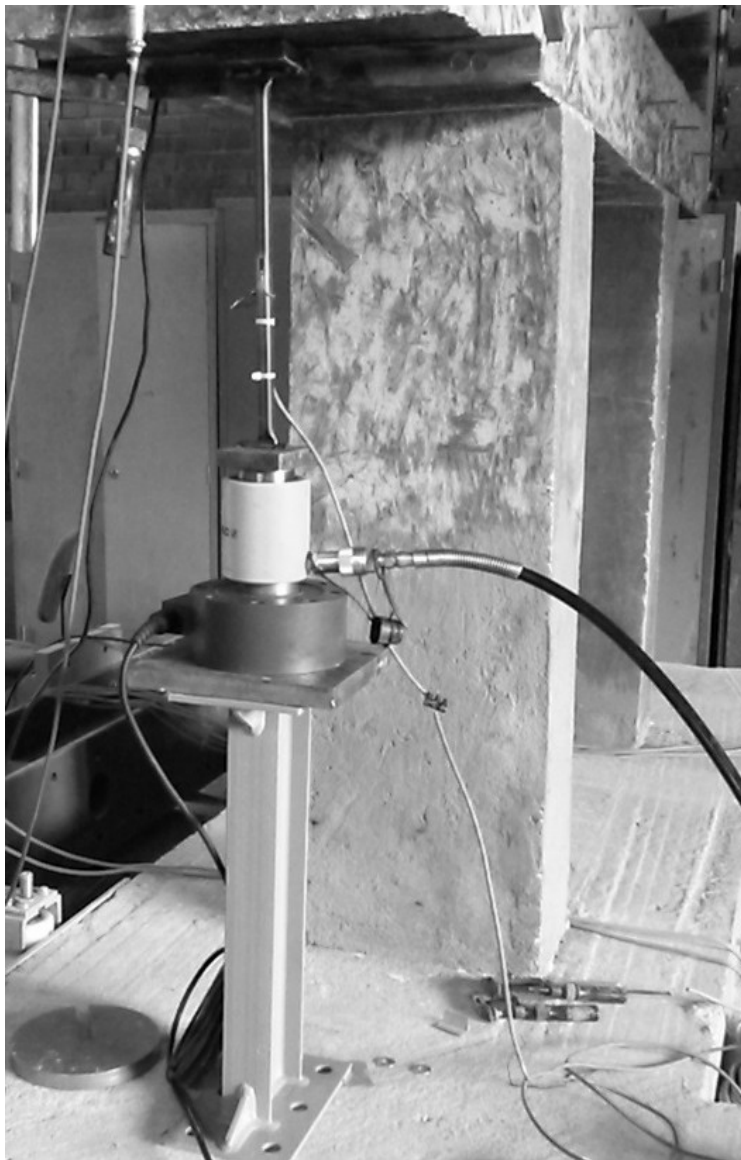


Figure 32. Initial test setup for plastic buckling

The next setup, which can be seen in Figure 33, is established on solid steel blocks which cannot be moved by the load necessary to plastically buckle the test column. The load is applied with the hydraulic jack and the load cell and strain gauge output results are simultaneously read from the computer.



Figure 33. Final test setup for plastic buckling

Before reaching to plastic buckling load, the column released some of the load at several stages. This is due to the fact that the hammered ends of the column crushed

at several stages before buckling, and this resulted in a stress release from the column. After the column ends were completely crushed, the axial load increased without any stress release, and the column buckled. Figure 34 shows the crushed ends of the column, and Figure 35 shows the buckled shape of the column. As it can be seen clearly when compared with a straight shape, the column could not return to its original shape after unloading. The results for the test are presented in section 2.5.2.



Figure 34. End crushing of the column before plastic buckling load is reached

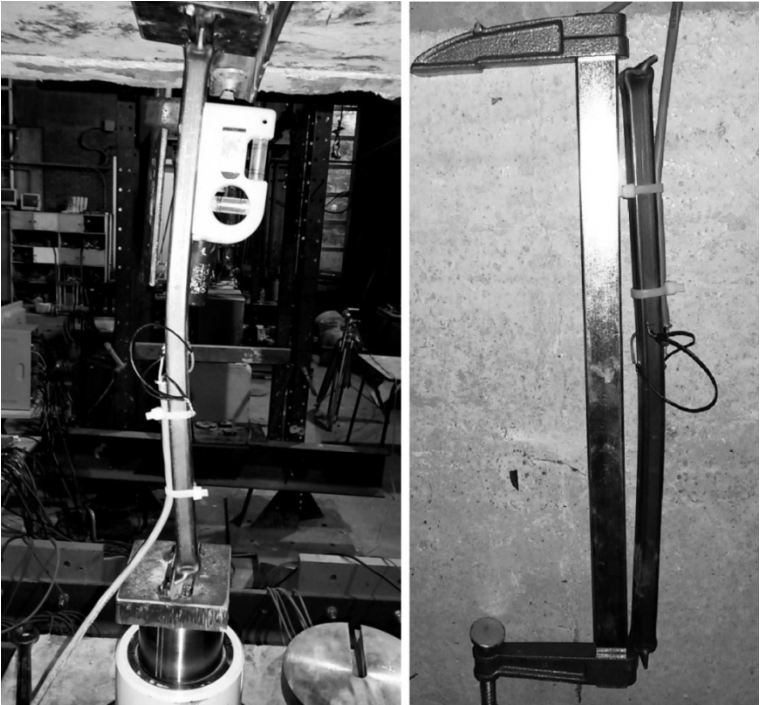


Figure 35. Plastically buckled column

2.5 DISCUSSION OF RESULTS

The results of the tests are presented in separate sections for elastic and plastic buckling in the following pages. These tests with the prototype of buckling sensor proved not only the measuring buckling with the help of strain gauges is possible, but also gave important hints about how to further develop the sensor to use in actual life with different types of columns.

2.5.1 Elastic Buckling Test Results

The elastic buckling tests are conducted for several different cycles since the column did not take any plastic deformation. In these cycles, the column is first buckled in one specific direction; then in the next cycle of loading, the buckling occurred in the opposite direction. However, to guide the column buckling in only one specific column axis, the hammered ends of the column played an important part.

Since the hammered ends were weaker along one axis of the column, buckling in different cycles occurred about this axis, even if it was in opposite directions. This was a preferred behavior since in the prototype column, half bridge configuration was used and the strain gauges were installed in only one axis of the column. If the buckling took part in the opposite direction of the sensors, then no data would be recorded. The sensor installation for different types of column cross-sections and bridge configurations will be discussed in the following paragraphs of this section.

The data collected from the load cell and the strain gauges are converted into axial load – moment, axial strain – bending strain, and axial stress – bending stress graphs for easier understanding.

For obtaining axial load – moment graph in Figure 36, the axial load values recorded from the load cell are used. For the moment values, a different approach is used. The test column specimen is placed on two supports as simply supported beam and two individual loading in the middle of the beam with 5 kg and 10 kg loads are taken. The maximum moments in the span are calculated under these loading. Then, the readings from the strain gauges and the corresponding moment values are used to obtain a moment per reading value. Bending moment values are calculated accordingly, for each sensor reading. See Table 3 below for detailed calculations.

Table 3. Moment per reading calculations

Sensor reading	Moment Value	Moment per reading
177 μV	<p> $L=920\text{ mm}$ 420 mm 500 mm $5\text{ kg}=50\text{ N}$ 27.2 N 22.8 N $M_{\text{max}}=11.4\text{ N.m}$ </p>	0.645 N.m
354 μV	<p> $L=920\text{ mm}$ 420 mm 500 mm $10\text{ kg}=100\text{ N}$ 54.4 N 45.6 N $M_{\text{max}}=22.8\text{ N.m}$ </p>	0.645 N.m

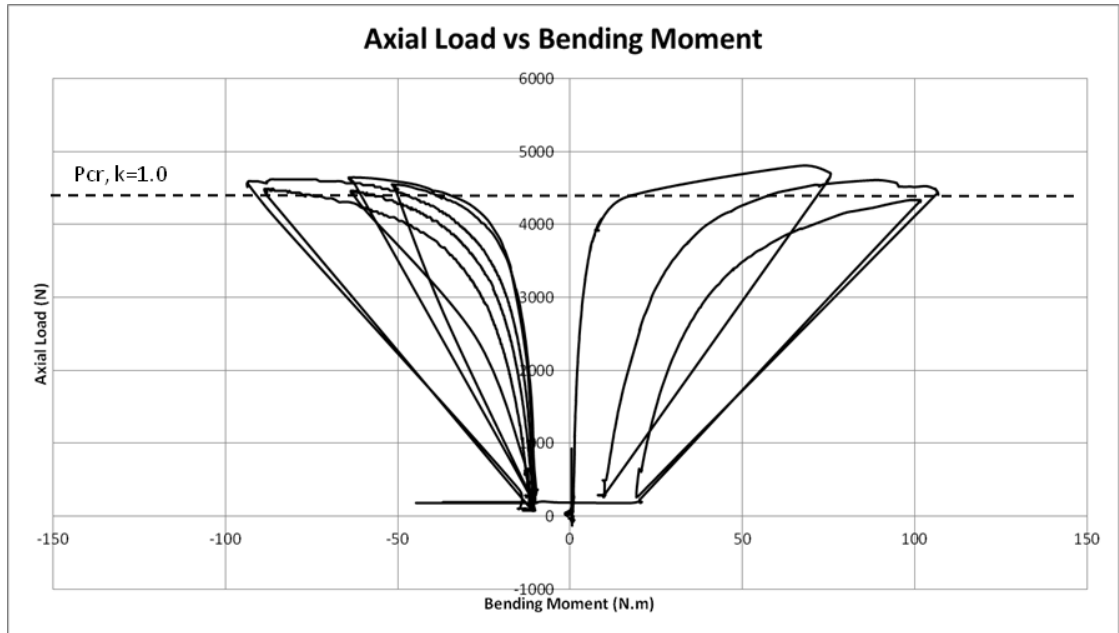


Figure 36. Axial load – bending moment graph for elastic buckling tests

For obtaining axial strain – bending strain graph in Figure 37, axial load values read from the load cell are divided by the cross-sectional area of the specimen. For the bending strain, equations (131) and (132) are used. The strain gauge voltage output values V_o , excitation voltage V_{Ex} , gauge factor GF are known parameters. Strain values ϵ_3 and ϵ_4 are zero since half-bridge configuration is used. Strain values ϵ_1 and ϵ_2 are same in magnitude but opposite in sign for a symmetrical loading. Therefore, the bending strain ϵ due to buckling of the column can be calculated as below:

$$V_o = V_{Ex} * \frac{GF}{4} * (\epsilon_1 - (-\epsilon_2)) = V_{Ex} * \frac{GF}{4} * (\epsilon_1 + \epsilon_2) \quad (131)$$

$$V_o = V_{Ex} * \frac{GF}{4} * 2\epsilon = 2500mV * \frac{2.0}{4} * 2\epsilon$$

$$\epsilon = V_o * \frac{10^{-3}}{2500mV} \quad (132)$$

Axial strain – bending strain graph is constructed accordingly. To check the column stress levels under buckling, also axial stress – bending stress graph is constructed. See Figure 37 and Figure 38 below for more detail.

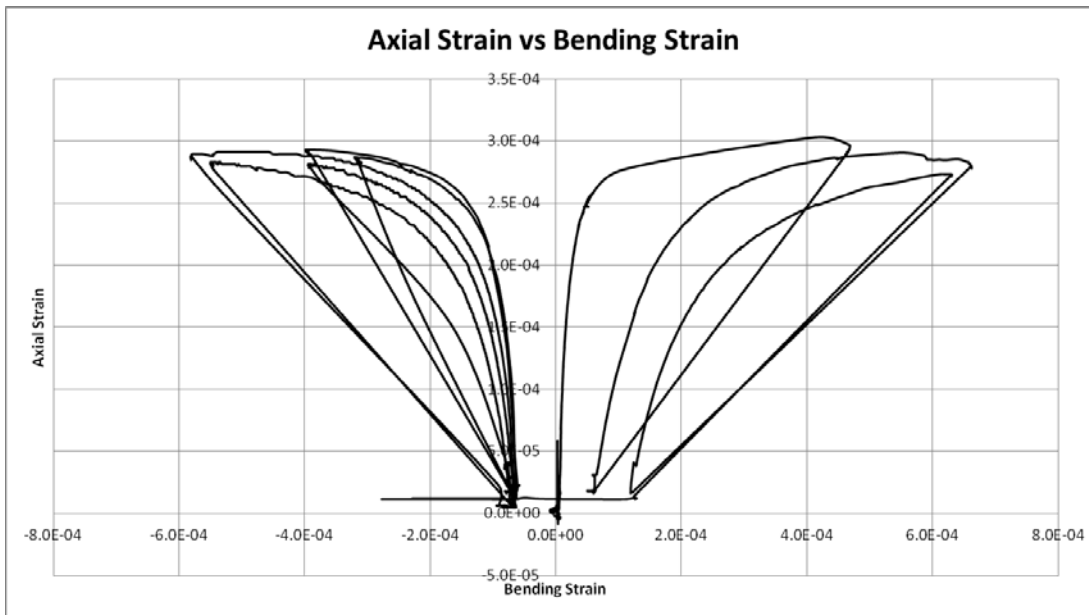


Figure 37. Axial strain – bending strain graph for elastic buckling tests

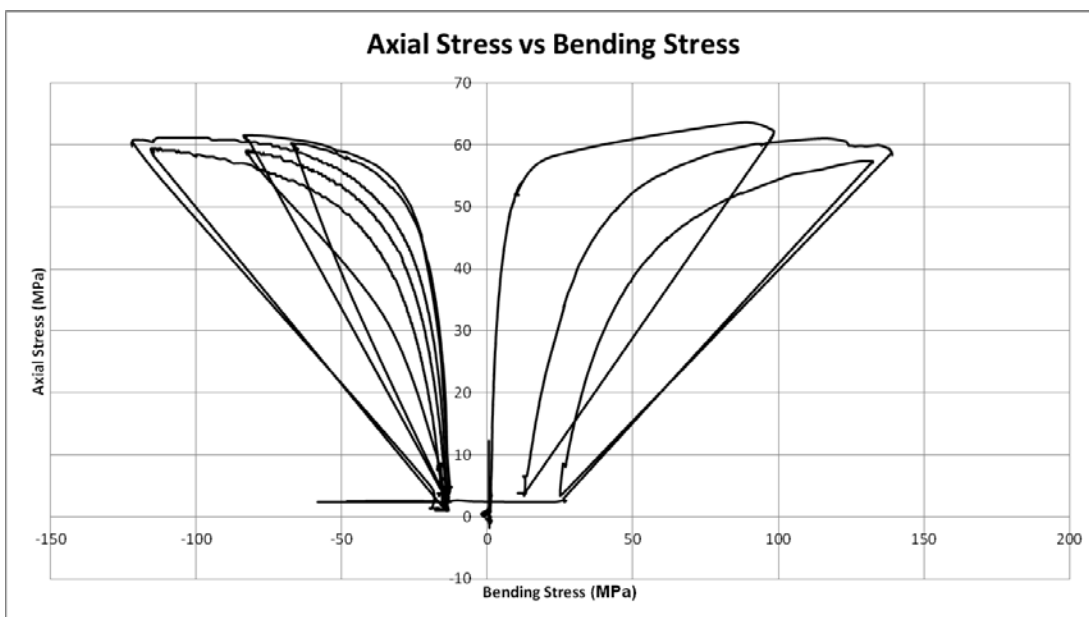


Figure 38. Axial stress – bending stress graph for elastic buckling tests

By examining the outputs, the following results are observed:

Initial imperfections: The slope shape of the graphs indicates that there is an eccentricity in loading. It was expected that the axial load value would increase without an insignificant change in lateral load, thus in secondary moment; and, after critical load was reached, the bending moment would dramatically increase with a slight change in axial load.

However, for the tested column, before reaching the critical load, bending moment also increase in small amounts with increasing axial load. This indicates either accidental eccentricity in loading or small initial imperfections in the test specimen.

Another reason for this may be the unloading of the column after buckling. The loading is conducted with a hydraulic jack by hand; and after buckling is observed, the unloading of the column is again controlled by hand, releasing the load slowly. However, to not let the column released from its position and got loose, the load on the column is not reset to zero. To keep it in position, a very small amount of compression is ensured even after unloading, which can also be observed in the graph in Figure 36. After the first loading/unloading cycle, if the column got out of its original position slightly, this might cause a small eccentricity in loading.

In the first set of tests, the eccentricity is higher; and in the second and third sets in the opposite column axis, the eccentricity is smaller. This can be related with the unloading again. After the first set of test, the column was unloaded fully and the second and third sets were conducted later. This shows that, after fully unloading, the column got back to its original shape and when it was loaded again, the eccentricity amount due to loading was smaller.

Decreasing the rate of unloading might generate better results in terms of eccentricity due to unloading.

Column stresses: As it can be seen from the axial stress – bending stress graph in Figure 38, the stresses in the column are smaller than yield stress 235 MPa for S235 steel. The greatest axial stress in the column is about 60 MPa, and the greatest bending stress is about 140 MPa. The elastic limits are not exceeded.

End conditions: When the shape of the buckled column in all test sets is examined, it can be seen that the maximum deflection is not in the middle of the column, but slightly closer to the upper end side. This may be caused due to the rigidity of the ends being slightly different than each other.

The upper end of the column was almost free to move when there is no compression in the system. It was hold in place by adding a small amount of compression to the system when the cylinder of hydraulic jack is ascended with the applied load. On the other hand, the lower end was placed inside the guide plate as seen in Figure 27. The

rigidity of the lower end is slightly greater than the upper end, and the maximum deflection being closer to the upper end supports this assumption. The column effective length k should be slightly smaller than 1.0 in this case.

It is a slight change in buckling load; however, it is important in indicating that how it is not possible to obtain a perfect pin-pin end condition in real life. In actual columns, due to connection types, flooring, etc. it is impossible to obtain a perfect pin end condition and the connection will always have some more rigidity than a theoretical pin restraint.

Wheatstone bridge configuration: The strain gauges in the test setup are in half-bridge configuration. This is mainly due to the fact that, for this specific test setup half-bridge configuration was sufficient to obtain the necessary output. However, for different column cross-sections and end conditions, different bridge configuration might be necessary.

The test column used has a square cross-section and it might buckle around one of its two axes, and it cannot be foreseen which side it will buckle. To overcome this, in the tests, the column ends are hammered and the buckling direction is predetermined. It may not be such simple in real columns, especially if it is an existing column of an already constructed structure.

For rectangular hollow sections or I-profiles, the buckling will occur in the weaker direction. Thus, Wheatstone bridge can be constructed in the weaker axis face of the column with half-bridge. In this case, the column will buckle only around the weaker axis, and the strain gauges on this face will be sufficient to measure the strain due to buckling. See Figure 39.

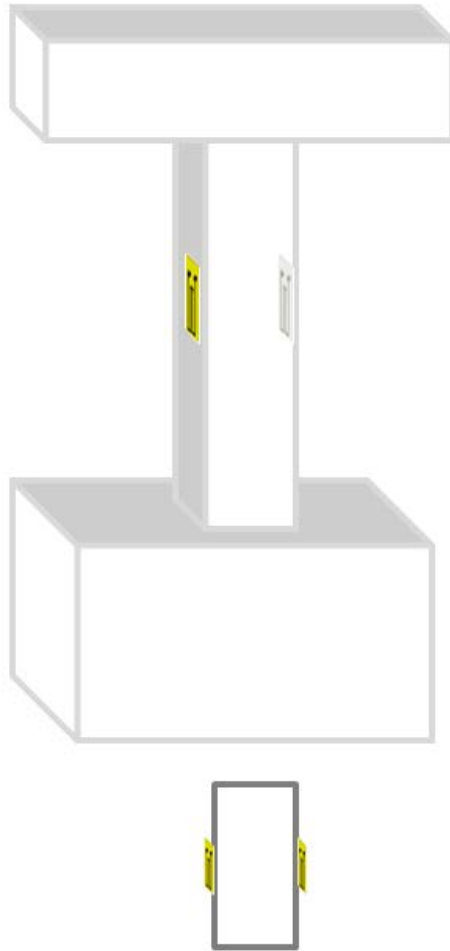


Figure 39. Rectangular hollow section column bridge configuration

For square hollow sections, as in the test specimen, if the end condition or lateral supports in one direction does not help determining the buckling direction, then two sets of separate half-bridges for each possible buckling direction can be used. See Figure 40.

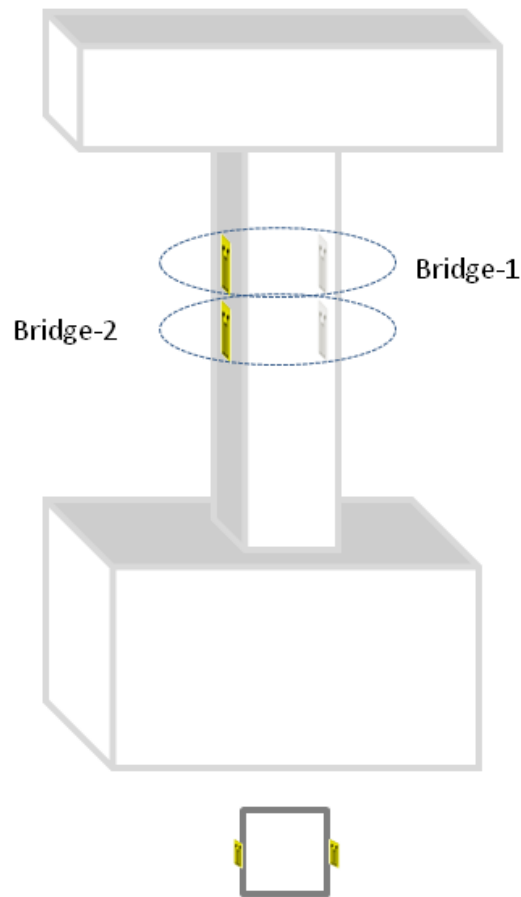


Figure 40. Square hollow section column bridge configuration

For a circular hollow section where the buckling might occur in any direction and it is not possible to use an internal lateral support due to circular face, the end condition is the determining factor to indicate buckling direction. For a pin-ended circular column, the direction of the pin connection generally indicates the possible buckling direction since it allows more rotation in one direction compared to other. See Figure 41 and Figure 42 for more detail.



Figure 41. Pin ended circular hollow section column [21]



Figure 42. Circular hollow section column bridge configuration

The existence of internal supports such as braces, internal beams etc. in the weaker axes of the columns also help determine the location of the strain gauges and bridge

configuration. Lateral supports increases the critical buckling load which means that, in the existence of lateral supports, higher buckling modes can be achieved. In this case, the strain gauges should be placed in the higher mode buckling nodes (which are the maxima of the sinusoidal shape).

Warning system: Another important issue to be discussed according to the results obtained is the sensor warning system. In fact, it is one of the main considerations of the sensor development.

The main concern in creating a warning system is the column existing load level. If the buckling sensor is to be installed on a new column in the construction stage, it is possible to observe the load levels from zero to any critical stage. For this case, it is easy to set a load limit for the sensor to give a warning. However, for an existing column where the load level is unknown, the warning system cannot work properly if it is set to give warning based on a load limit. Therefore, it is more preferable to design a warning system based on changes in strain levels or a ratio of elastic modulus to tangent modulus.

As it can be observed in axial strain – bending strain graph in Figure 37, when buckling occurs, bending strain dramatically increases. This property can be used to create a warning in the sensor since bending strain is calculated according to the strain gauge output voltage value as explained in equation (131). Of course, it would not be practical to give warning just as the buckling takes place since it is a sudden failure. In the test column, as it was discussed under initial imperfections title, it is observed that either the column was initially imperfect or a small eccentricity in loading existed. This is the case for most of the actual columns and even the design codes recognizes this issue, and lead the designer to use necessary factors in design to take into account the effect of imperfections.

Based on the assumption that actual columns always have initial imperfections based on manufacturing, construction/erection, or simply by accidental loading, the axial strain – bending strain relations will be similar to the test column. In this case, the increase in bending strain will be initiated with the increase in axial strain, but with small increments. Then the buckling will occur and the bending strain will sharply increase compared to the axial strain. The warning system can be based on the

increment of bending strain. It can be constructed such that when the increase rate in bending strain exceeds a certain predetermined value, it can give warning through data acquisition system.

For example, the strain graph from the first data set of the elastic buckling is given in Figure 43. In the graph, the tangent lines from initial bending strain value are drawn as well as the tangent lines at arbitrary strain values. The slope of the tangent lines, α can be calculated directly in the program inside the data accusation system based on the strain values as they are being measured. The data acquisition systems have their own software which allows the user to adjust the values to be measured and their properties. The computation of the tangent slope can be computed in the software by encoding the necessary formulas.

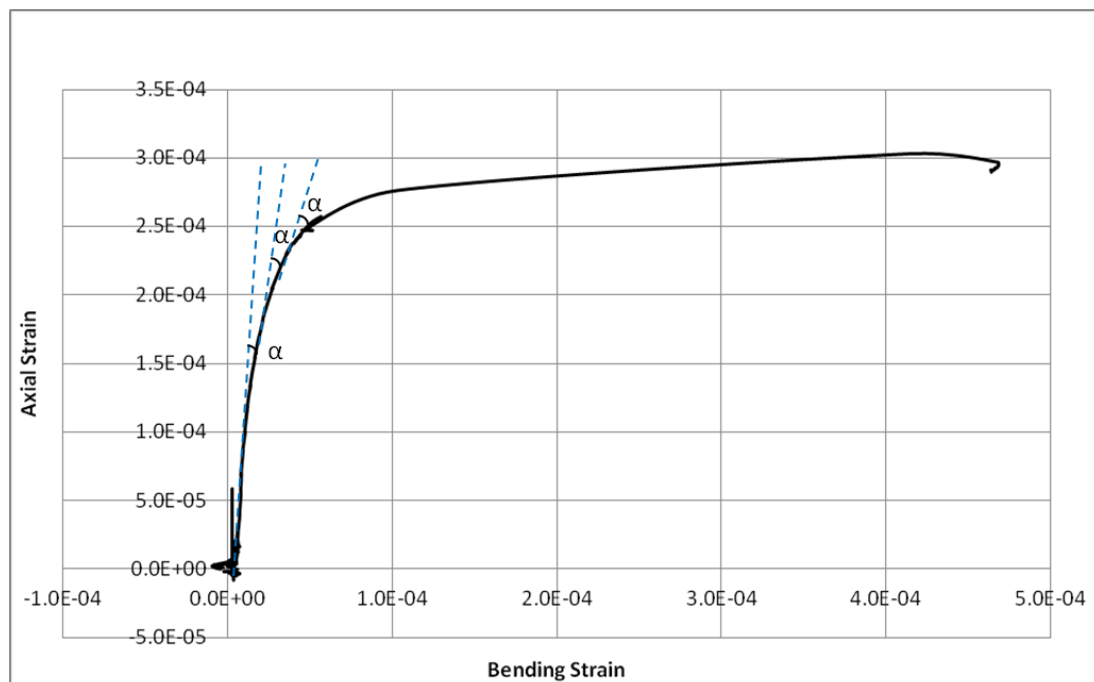


Figure 43. Bending strain change determination for buckling warning

In Figure 44 below, the warning system based on the slope of axial strain – bending strain is illustrated. The solid line passing through the curve represents the zero-point locations of the second derivative of the slope curve. At these locations, as it can also be observed from the curve itself, the slope α changes direction. It is proposed to use these locations to give warning in the system. It can be seen from Figure 44 that after slope curve changes direction, at around $P_{cr}=4300$ N theoretical load, buckling occurs.

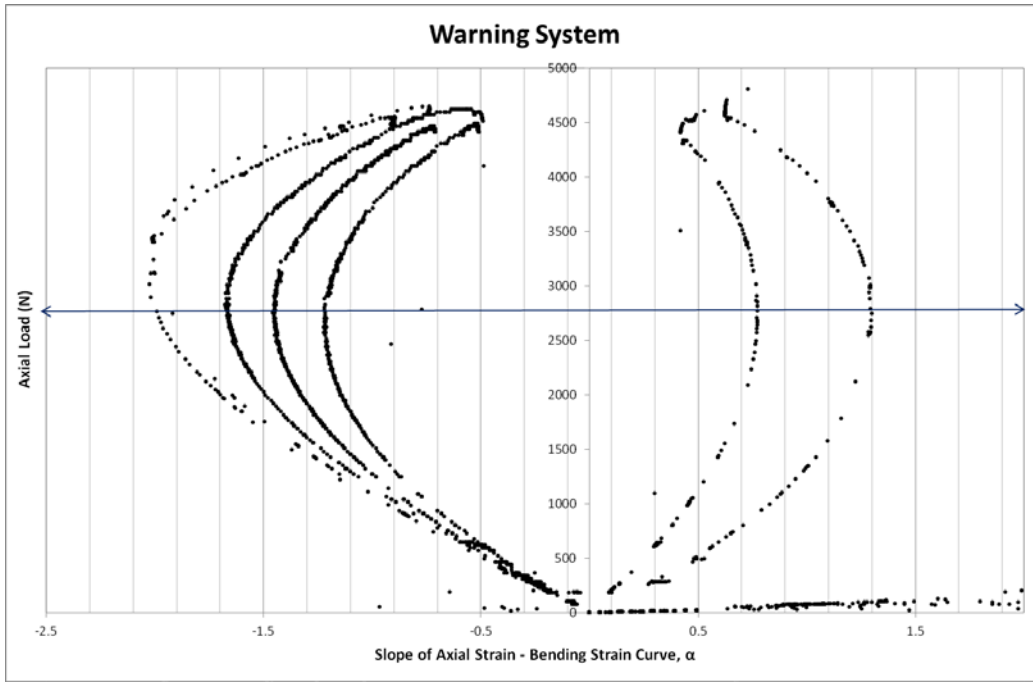


Figure 44. Warning system based on slope of axial strain – bending strain curve

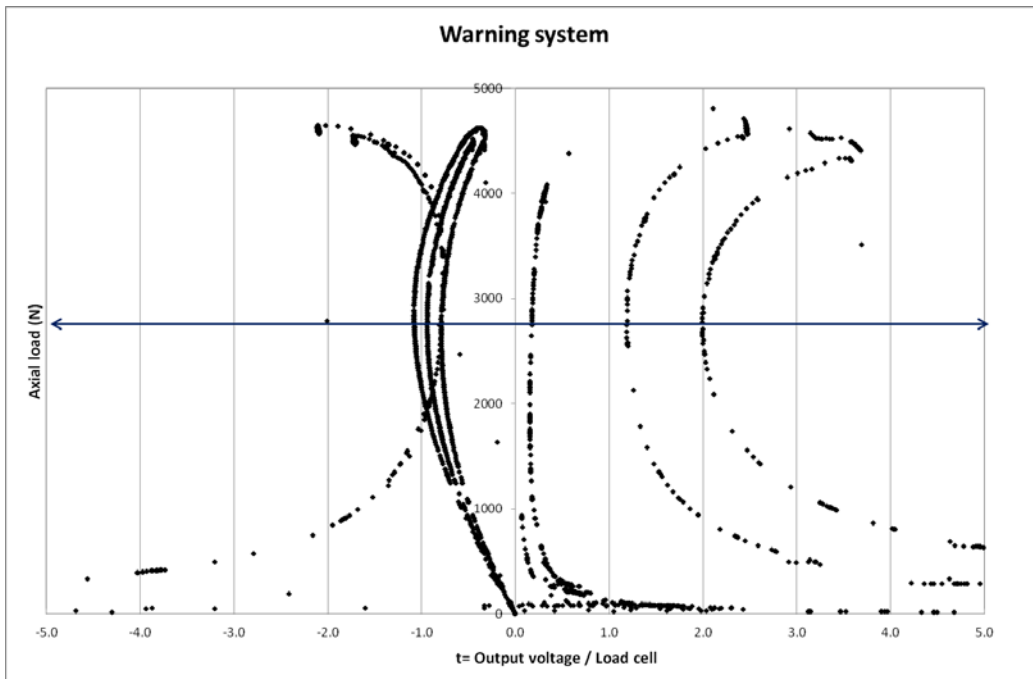


Figure 45. Warning system based on output voltage/load cell reading curve

In a similar manner, the ratio of output voltage to load cell readings, designated as t , can be plotted against axial load as in Figure 45. Similar to the slope curve, the locations as marked on Figure 45, which indicates the change of direction of t curve, can be used to give warning in the system.

In both curves in Figure 44 and Figure 45, the locations where the warning is given corresponds to a load limit of about 1.5 times smaller than the theoretical buckling load.

The main problem with the warning system might be time. Even if the warning at a strain value much lower than buckling strain is given, depending on the loading rate, it may still be too late until an action against buckling (such as strengthening the concerned column) is taken. In this case, if it is known that the loading rate is high, warning limit can be decreased to gain more time.

However, if the loading is sudden, such as an accidental loading, warning system may be useful not for preventing the overall buckling, but for tracing the rate of increase in loading of columns of a floor, and at which column the buckling may proceed after the first column buckles. This may be beneficial in determining which areas are still safe or which floors or parts of floors should be evacuated first.

2.5.2 Plastic Buckling Test Results

The plastic buckling test is conducted for the short column for once; since after being plastically deformed, the test specimen cannot be used anymore. As already mentioned in 2.4.2, the plastic buckling test setup was first contained a steel pedestal under the cylinder hydraulic jack and test column. However, this test setup was later changed since the steel pedestal was not stable under the loading. The second test setup was mounted on rigid steel blocks instead, and the stability problem of the supporting surface was solved.

The axial load – bending moment, axial strain – bending strain and axial stress – bending stress graphs of the plastic buckling test can be seen in Figure 46 and Figure 47. The idealized graphs can also be seen in Figure 48 and Figure 49. These idealized graphs shows a cleaner data excluding the noisy data due to end crushing effects which will be discussed in the next paragraphs. The buckling load, strain and stresses are the same in the both set of graphs.

End crushing: The main observation in the plastic buckling test is the end crushing. It was seen that while loading with the hydraulic jack proceeded, the load read from load cell started to decrease at some points. At these points, the loading was stopped to check the column and it was seen that the hammered ends of the column started to

crush before buckling load is reached. After the crushing was completed and the column ends became almost flat, the loading of the column continued in its normal phase and then the buckling occurred. The effect due to end crushing can also be seen in the axial load – bending moment and axial strain – bending strain graphs in Figure 46 and Figure 47.

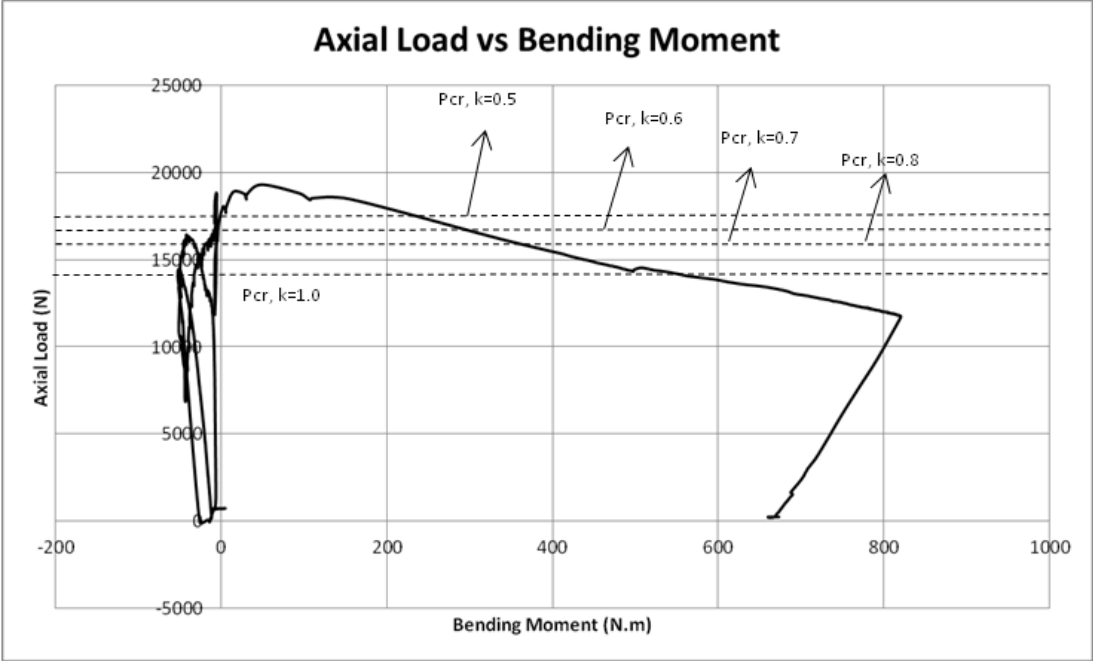


Figure 46. Axial load – bending moment graph for plastic test

It is observed from the axial load – bending moment graph that the column was strained in one direction, and then the decrease in axial load due to end crushing started. After the end crushing completed, the increase in axial load started; however, this time the column started to get strained in the opposite direction. This is due to the crushed end being not completely smooth and having an inclination towards one direction. This redirected the column buckling direction and the increase in loading continued with increased strain in the opposite direction. The idealized graphs with cleaned data implies that, if the buckling occurred in the direction the deformations started, then the data will be similar to Figure 48. The dashed lines in Figure 48 imply the possible axial load – bending moment graph not in terms of magnitude, but figuratively.

The end crushing started with one end and then after it is completely flattened, the crushing of the other end accelerated. The effective length and column end crushing relationship is discussed in the following paragraphs.

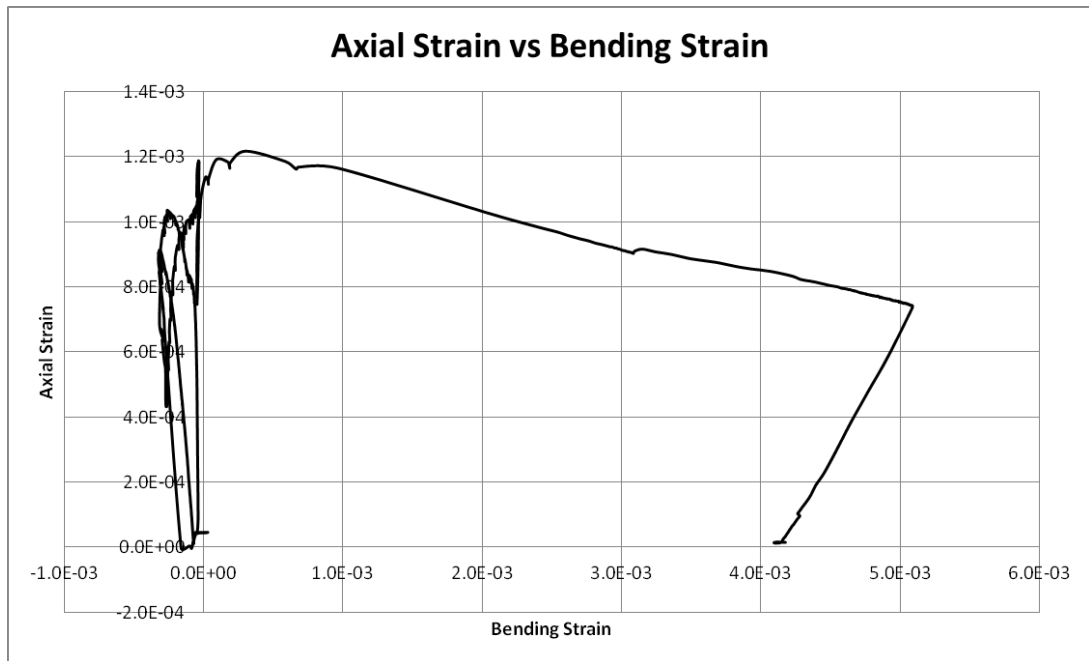


Figure 47. Axial strain – bending strain graph for plastic test

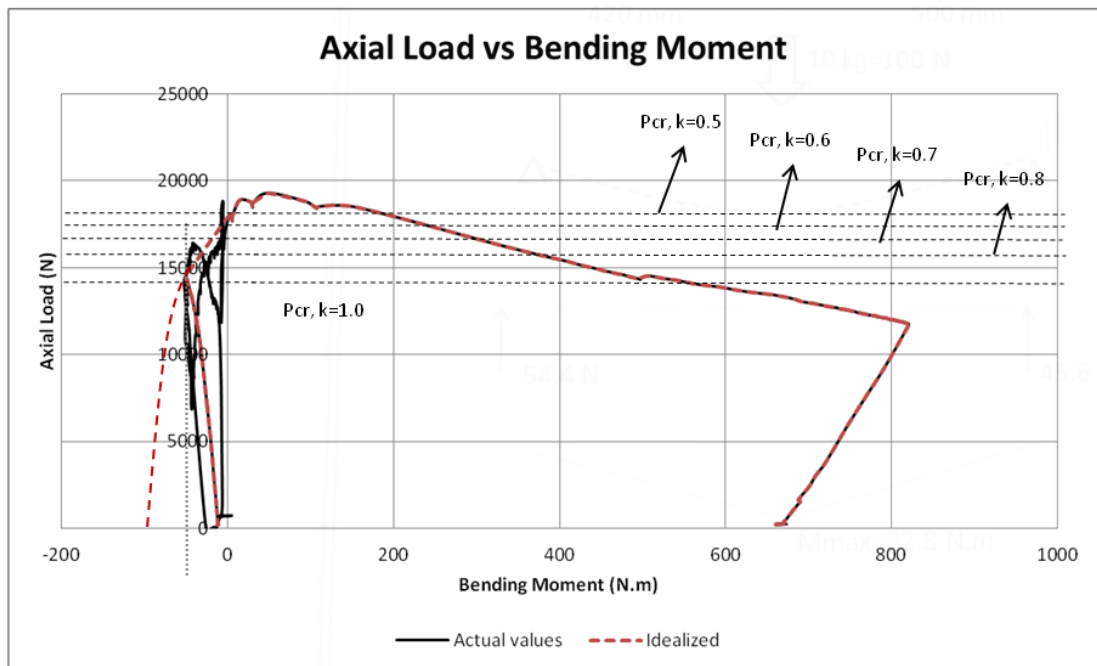


Figure 48. Axial load – bending moment idealized graph for plastic test

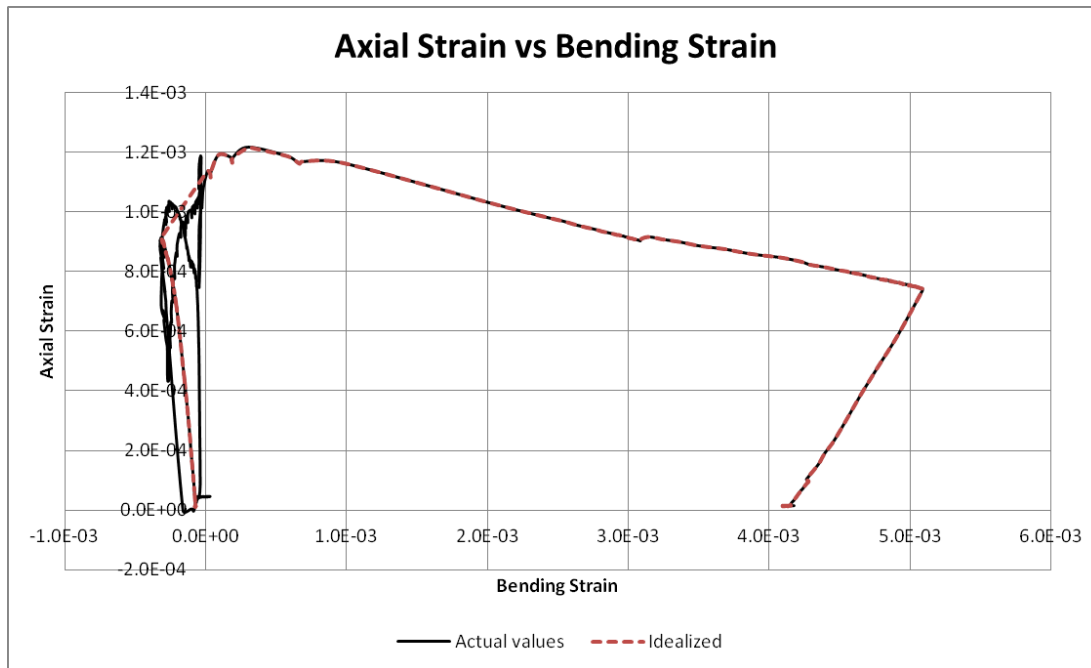


Figure 49. Axial strain – bending strain idealized graph for plastic test

Effective length factor: Due to the effect of end crushing, the column end conditions changed from pin to semi-rigid, since the flat bottom of the column cannot rotate as freely as a pin support. Therefore, the effective length factor is reconsidered for this case with different k factors, $k=0.8, 0.7, 0.6$ and 0.5 .

$$P_{cr} = A * \sigma_y \left[1 - \frac{\sigma_y \left(\frac{kL}{r} \right)^2}{4\pi^2 E} \right] = 75.52 * 235 \left[1 - \frac{235 \left(\frac{0.8*400}{4.86} \right)^2}{4\pi^2 210000} \right] \quad (133)$$

$$= 15566 \text{ N}$$

$$P_{cr} = A * \sigma_y \left[1 - \frac{\sigma_y \left(\frac{kL}{r} \right)^2}{4\pi^2 E} \right] = 75.52 * 235 \left[1 - \frac{235 \left(\frac{0.7*400}{4.86} \right)^2}{4\pi^2 210000} \right] \quad (134)$$

$$= 16077 \text{ N}$$

$$P_{cr} = A * \sigma_y \left[1 - \frac{\sigma_y \left(\frac{kL}{r} \right)^2}{4\pi^2 E} \right] = 75.52 * 235 \left[1 - \frac{235 \left(\frac{0.6*400}{4.86} \right)^2}{4\pi^2 210000} \right] \quad (135)$$

$$= 16520 \text{ N}$$

$$P_{cr} = A * \sigma_y \left[1 - \frac{\sigma_y \left(\frac{kL}{r} \right)^2}{4\pi^2 E} \right] = 75.52 * 235 \left[1 - \frac{235 \left(\frac{0.5 * 400}{4.86} \right)^2}{4\pi^2 210000} \right] \quad (136)$$

$$= 16895 \text{ N}$$

This result indicates that end crushing may affect the effective length for buckling and thus the previously approximated buckling load in a pin ended column. Therefore, even if in theory plastic buckling load of pin ended column can be calculated, in actual case, it will be closer to a case with semi-rigid end conditions.

Strain gauge locations: When the plastic deformations take place, the strain gauge material will also yield. Therefore, in this case, the strain gauges can be installed not exactly at the mid-span of the column but a small amount away from the mid-point. However, this location arrangement should be done such that the strain gauges can still measure the strain values from the nodal point. The optimal distance of the strain gauges should be the distance at which the plastic deformations not occur at the instant the buckling occurs, but also not very far away from column the mid-point. With further experiments on plastic buckling, this optimal distance can be obtained.

Another suggestion is to locate the strain gauges at mid-span but in lateral direction. This way, the strain measurements will also include the Poisson effect, and according to the column material, 25 to 30% of the actual strain will be measured in lateral configuration. This configuration allows the strain gauges to collect more strain measurements without reaching the yield point.

CHAPTER 3

CABLE TENSION MEASUREMENT DEVICE

In this chapter, the theory behind the cable working principles is first introduced. Then, the development stage of the cable tension measuring device based on this theory and its working principles are explained in detail. Finally, the prototype tests to prove that the device based on theory actually works are conducted. The observations and discussions of the test results are presented as well.

3.1 CABLE HISTORY, DEFINITIONS AND COMPOSITION

3.1.1 History of Modern Cables

Generally, the term *cable* and *wire rope* are used interchangeably in the bridge terminology. The evolution of steel chains and solid bars to wire ropes started in 1830s along with the mining hoist applications in the Harz Mountain silver mines in Germany.

The first versions of wire ropes developed were three simple wrought iron wires of same size which were twisted around each other by hand. Then these twisted strands were twisted around in groups of three or four to create a rope. All procedure was done by hand. These first versions of cables were named as Albert ropes after William Albert, the Harz mine official who introduced this technique.

Around the same time, Andrew Smith, a London based inventor who was experimenting with wire ropes to be used in ship rigging, manufactured various kinds of wire ropes. His wire ropes were manufactured by using the same techniques of hemp cordage. Moreover, Smith's wire ropes were also used in the Blackwell Railroad haulage instead of hemp ropes.

Meanwhile, Robert Newall who was also an Englishman like Smith, developed a method to twist the Albert ropes by machinery instead of hand-twisting. The wire ropes of Andrew Smith which were used in Blackwell Railroad haulage were manufactured by this method. Newall's machine twisted cables were composed of six strands twisted around a fiber core, which will later dominate the market. Newall and Smith merged their companies later.

The success of wire rope development in Europe also led to its highlight in the United States, especially in railroad industry. John Roebling, a surveyor, developed his own wire ropes which were twisted by hand like Albert ropes, but consisted of a wire core like Smith and Newall's ropes. The difference of Roebling's ropes was they were composed of entirely wires including the core unlike the strands made of twisted wires with a fiber core used in Albert, Smith and Newall's ropes. Roebling's ropes included six outer strands and an identical inner core each made of 19 wires. After realizing that 19-twisted wires resulted in a hexagonal shape rather than a round shape, Roebling experimented on machined-twisted wires for making the wire rope shape rounder. He then opened his own factory in 1848.

Roebling also developed the three-size construction of wires to overcome the defects caused by the six same sized strands. He used different wire sizes in combination for creating a strand. The three-sized ropes are composed of a seven-wire strand made of same wire sizes wrapped up of an outer layer of twelve wires consisting of two different wire sizes. This new wire ropes not only became rounder in shape, but also overcame the negative effect of internal crossovers due to hollow space left in the equal size strands. Since there was less hollow space left in between the strands, it provided a stronger support, later known as equal-lay principle.

Around the same time, Andrew Smith's son who had moved to California, U.S. worked in wire rope industry and dedicated himself to developments in the industry.

Changing his name to A. S. Hallidie, he developed his own method of equal-lay stranding named California Cable, consisting of triangular shaped wires. In terms of equal-lay concept, his technique was superior to Roebling's; however, it was difficult and more costly to manufacture.

The wire lay configurations evolved in time according to the needs in the different industries the wire ropes were used such as cable cars, railroads and mining. For example, Thomas Seale developed a new lay configuration for cable car wires to increase the wire wear resistance. Later, James Stone developed the 6 small size filler wires for cushioning, wrapped up with 19 wires of nearly the same size. His wires were not only almost round in shape, but also stronger in terms of wear resistance. Stone's wire is still the most widely used configuration in the world for different industries. [22]

3.1.2 Definitions and Construction

As briefly mentioned in the historical development of the wire ropes, a wire rope is basically composed of strands of wires twisted around each other which are surrounding an inner core.

Wire ropes are divided into two main categories in terms of construction: Spiral ropes and stranded ropes. Spiral ropes are basically round strands which are helically layered on each other. There are several layers of strands in a spiral wire rope some of which are in the opposite direction to the outermost layer. The main advantage of spiral rope is that it can be dimensioned so that there is no rope torque exists under tensile loads. [23] Figure 50 shows the typical spiral rope cross-sections.

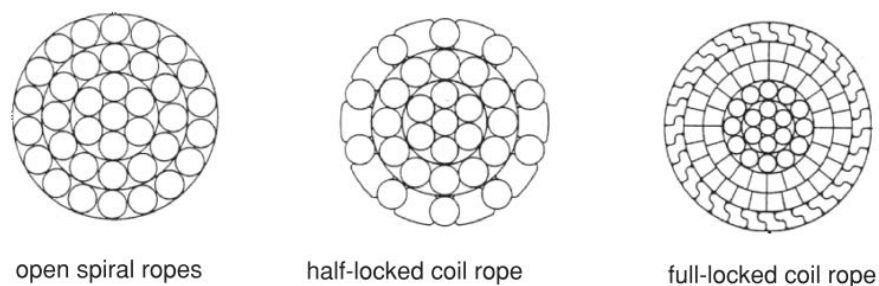


Figure 50. Typical spiral wire rope cross-sections [23]

The stranded wire ropes have a fiber or wire core which is wrapped up with several layers of strands. The lay direction of a stranded wire rope is also important. The wire lay configuration is evolved throughout the wire rope history. To construct the most efficient lay of wires with minimum hollow zone and rounder shape, the wire and strand sizes as well as the lay angle and lay direction are important. Figure 51 illustrates the elements of a typical stranded wire rope.

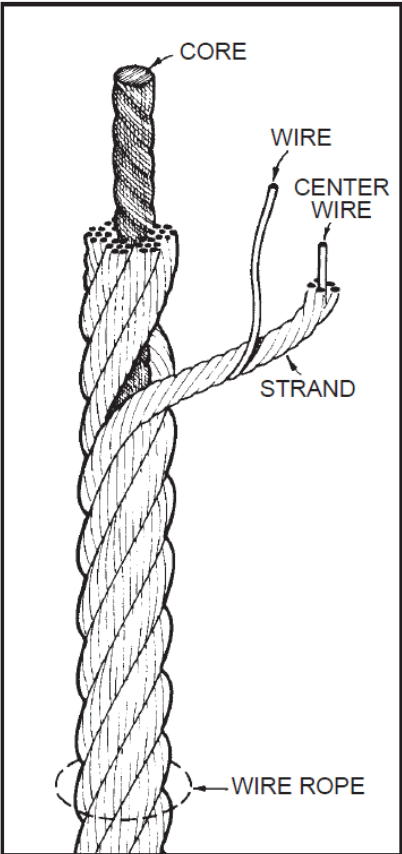


Figure 51. Elements of a typical stranded wire rope [24]

The lay length h_w is the strand length which makes a complete turn. The wire winding radius r_w is the center to center distance between the two outermost strands in the same plane. These definitions are also described figuratively in Figure 52. The lay angle α is given by the equation below:

$$\alpha = \tan^{-1} \left(\frac{2\pi * r_w}{h_w} \right) \tag{137}$$

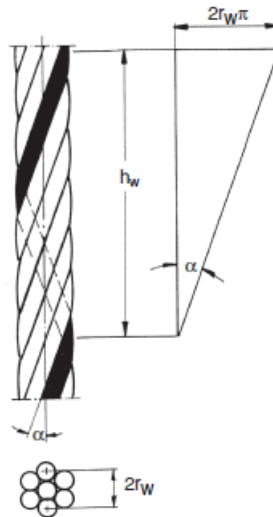


Figure 52. Definition of lay length, lay angle and winding radius [23]

The lay direction is a definitive property of a wire rope as much as the number of strands in a rope. There are five common lay configuration used in the modern industry of wire ropes as illustrated in Figure 53.

The first lay configuration in Figure 53 is a *right hand lay*, in which the strands are laid into rope to the right. The second configuration is a *left hand lay*, where the strands are laid into the left side of the rope. The right and left hand lays can be understand better with an analogy of bolt threads. Right hand lay resembles a right hand threaded bolt; on the other hand, left hand lay is similar to the threading in a left hand bolt with threads against the left hand side.

The first two lay configurations are also called *regular lay*. The regular lay occurs when the lay directions of the wires in a strand and the strands in the rope are in the opposite direction.

The third and fourth configurations in Figure 53 are called *Lang lay* in which the lay directions of the wires in a strand and the strands in the rope are in the same direction. In this configuration, unlike regular lay, there is an angle between the wires in the strands and rope axis. The Lang lay ropes are more resistant to axial bending of individual wires of strands since they are at an angle from the rope axis. On the other end, if the end fixations of a Lang lay rope are not adequate, it will rotate enormously under applied load.

The final lay configuration is *alternate lay*, which consists of regular and Lang lay strands at the same time. [24]



Figure 53. Strand lay configurations [24]

Wire ropes are designated by their strand number and the number of wires in an individual strand. For example, a 6x7 rope consists of 6 strands where each has 7 wires. Whenever the wire size in a strand differs, the designation includes specific names as well as numbers. Below, Figure 54 illustrates the different wire configurations commonly used in practice.

According to their usage, wire ropes are classified into several groups which can be seen in Figure 55. For instance, ropes bent over sheaves or drums are called *running ropes* and these are mainly resisting to bending. Wire ropes used in bridges are called *stay cables* and mainly resisting tensile stresses. *Track ropes* are used as rail in aerial tracks or elevator cabins as well as cable cranes. The ropes which are used to carry goods are called *rope slings*, and even though they are mainly resisting tension, the edges of the sling ropes are under bending loads. [23]

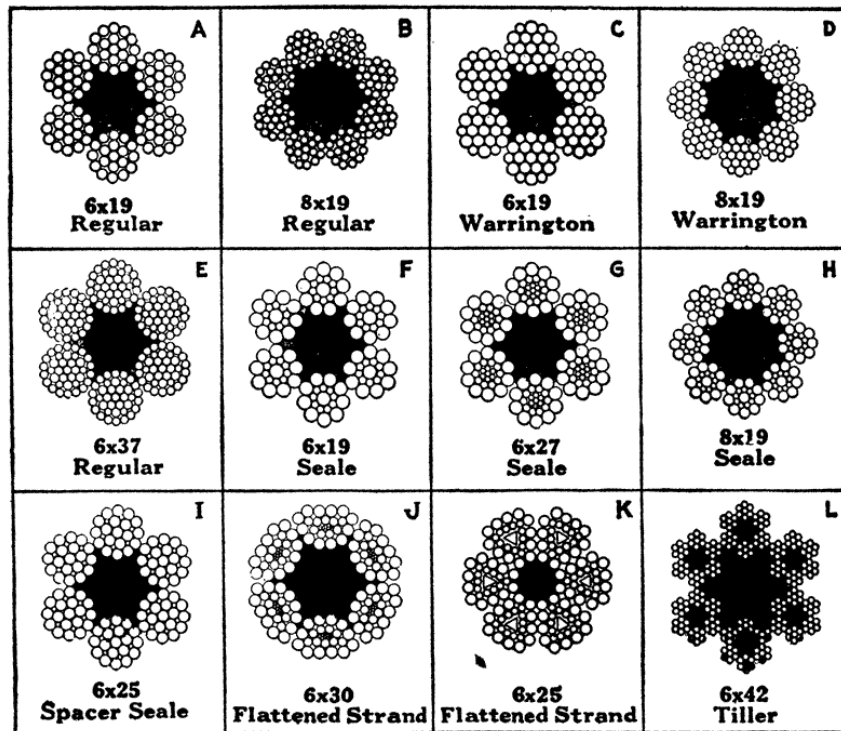


Figure 54. Cross sections of commonly used wire ropes [25]

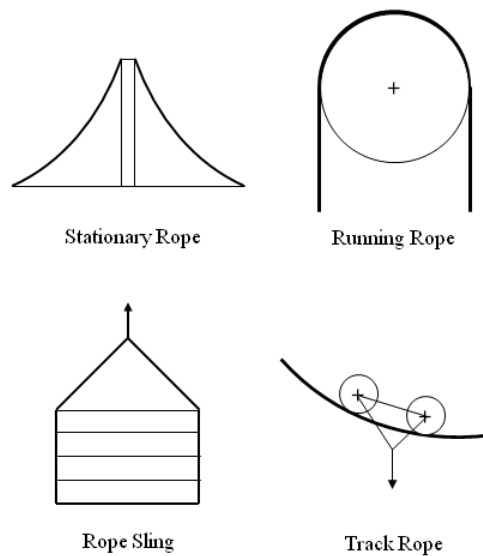


Figure 55. Wire rope classification according to usage

In this thesis, the wire ropes resisting mainly to tension will be investigated. These kinds of wire ropes are generally named as “cables”.

3.2 CABLES UNDER TENSION

A wire rope is a tensile stress resisting element consisting of tension resisting wires and strands. Therefore, the global tensile resisting of a wire rope is the sum of tensile resistances of combined wires.

$$\sigma_z = \frac{S}{A} \quad (138)$$

$$A = \frac{\pi}{4} \sum \delta_i^2 \quad (139)$$

Where, S is the rope tensile load and δ_i is the diameter of an individual wire in a strand.

Wires in ropes are stressed differently due to lay angle; this is an expected systematic stress difference. On the other hand, an unsystematic stress difference may also exist in wires and strands if they lie loose and do not start to take the load from the start. This causes an increase in the tensile load in the rope. However, in the calculations of wire rope stresses, unsystematic stresses will be ignored. Also, it is assumed that all the stresses are in elastic range, and turning of strands are prevented.

3.2.1 Tensile Force in a Wire

The outer forces, tensile strand force S_i along the axis of the rope, and circumference force U_i for each wire, must be in balance with the inner forces, wire tensile force F_i and wire shear force Q_i . by assuming outer forces S_i and U_i are known, inner forces F_i and Q_i are calculated as follows by using the lay angle α_i and wire winding radius r_i . [23] Figure 56 also illustrates the forces in the individual wires of a strand.

$$F_i = \frac{S_i - Q_i * \sin \alpha_i}{\cos \alpha_i} \quad (140)$$

$$Q_i = \frac{\sin \alpha_i}{r_i} * (M_{b,i} \cos \alpha_i - M_{tor,i} \sin \alpha_i) \quad (141)$$

$$F_i = \frac{S_i}{\cos \alpha_i} - \frac{\sin^2 \alpha_i}{r_i * \cos \alpha_i} * (M_{b,i} \cos \alpha_i - M_{tor,i} \sin \alpha_i) \quad (142)$$

$M_{b,i}$ is the bending moment around the binormal axis and $M_{tor,i}$ is the torsional moment.

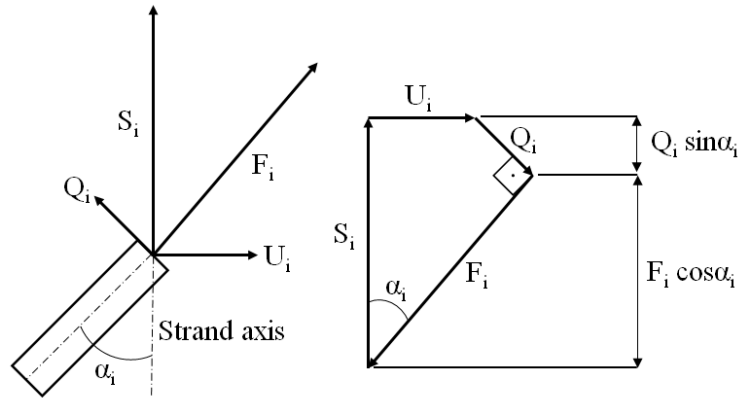


Figure 56. Forces in the individual wires of a strand

$$M_{b,i} = E_i * J_i * \left(\frac{\sin^2 \alpha_i}{r_i} - \frac{\sin^2 \alpha_{0i}}{r_{0i}} \right) \quad (143)$$

$$M_{tor,i} = G_i * J_{pi} * \left(\frac{\sin \alpha_i * \cos \alpha_i}{r_i} - \frac{\sin \alpha_{0i} * \cos \alpha_{0i}}{r_{0i}} \right) \quad (144)$$

Where, E_i is the modulus of elasticity, G_i is the shear modulus, J_i and J_{pi} are the equatorial and polar moments of inertia respectively of a wire in layer i . The subscript 0 stands for the unstressed state of wire. Other parameters without subscript 0 , are stands for the stressed state of wire. Since lay angle does not change much under tensile loads, both moments are insignificantly small and can be neglected from the equations. [23] Therefore, equation (142) can be simply rewritten as:

$$F_i = \frac{S_i}{\cos \alpha_i} \quad (145)$$

$$U_i = F_i * \sin \alpha_i = \frac{S_i}{\cos \alpha_i} \sin \alpha_i = S_i \tan \alpha_i \quad (146)$$

The portion of the strand torque in layer i :

$$M_i = F_i * r_i * \sin \alpha_i = S_i * r_i * \tan \alpha_i \quad (147)$$

3.2.2 Tensile Force in a Strand or Wire Rope

In 3.2.1, the tensile force in a wire is written in the form of the tensile force in a strand, assuming that the strand force is known. To calculate strand tensile force, the force in the wires should be known. The calculation of wire tensile force, and then the strand tensile force, is given separately for spiral ropes and stranded ropes in 3.2.2.1 and 3.2.2.2.

3.2.2.1 Tensile Force in a Strand or a Spiral Rope

The strand tensile force is the sum of wire tensile stresses S_i in the considered strand which will be calculated according to relations described in 3.2.1. z_i is the number of wires in a strand and n is the number of wire layers. In this case $n=0$ is used for center wire.

$$S = \sum_{i=0}^n S_i * z_i = \sum_{i=0}^n z_i * F_i * \cos \alpha_i \quad (148)$$

To calculate the total strand tensile force, first the individual forces in the wires should be calculated. Wire tensile force can be calculated from the elongation in the wire. [23]

$$F_i = \frac{\Delta l_i}{l_i} * E_i * A_i \quad (149)$$

$$\varepsilon_i = \frac{\Delta l_i}{l_i} \quad (150)$$

Where, l_i is the wire length, Δl_i is the change in wire length, E_i is the modulus of elasticity, A_i is the cross-sectional area of the wire and ε_i is the extension of the wire. Wire length l_i can be written in terms of strand length l_s .

$$l_i = \frac{l_s}{\cos \alpha_i} \quad (151)$$

$$\Delta l_i = \Delta l_s * \cos \alpha_i - \Delta u_i * \sin \alpha_i \quad (152)$$

The change in wire length Δl_i is calculated according to the Figure 57 below. u_i is the winding circumference, Δu_i is the change in the winding circumference, and ν_i is the equivalent of Poisson's ratio in a wire helix.

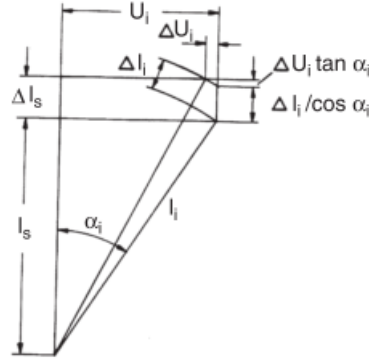


Figure 57. Wire elongation in a strand [23]

$$\Delta u_i = \varepsilon_i * \nu_i * u_i = \varepsilon_i * \nu_i * l_i * \sin \alpha_i \quad (153)$$

$$\nu_i = \frac{\Delta u_i / u_i}{\Delta l_i / l_i} \quad (154)$$

$$\Delta l_i = \Delta l_s * \cos \alpha_i - \varepsilon_i * \nu_i * l_i * \sin^2 \alpha_i \quad (155)$$

$$\Delta l_i + \Delta l_i * \nu_i * \sin^2 \alpha_i = \Delta l_s * \cos \alpha_i \quad (156)$$

$$\Delta l_i (1 + \nu_i * \sin^2 \alpha_i) = \Delta l_s * \cos \alpha_i \quad (157)$$

$$\Delta l_i = \frac{\Delta l_s * \cos \alpha_i}{1 + \nu_i * \sin^2 \alpha_i} \quad (158)$$

By substituting equation (158) into equation (149) the tensile force in a wire is calculated as below:

$$F_i = \frac{\Delta l_s * \cos \alpha_i * E_i * A_i}{l_i * (1 + \nu_i * \sin^2 \alpha_i)} = \frac{\Delta l_s * \cos^2 \alpha_i * E_i * A_i}{l_s * (1 + \nu_i * \sin^2 \alpha_i)} \quad (159)$$

Now that the tensile force in the wire is known, the tensile force in a strand can be calculated. [23]

$$S_i = \frac{\Delta l_s * \cos^2 \alpha_i * E_i * A_i}{l_s * (1 + \nu_i * \sin^2 \alpha_i)} \quad (160)$$

$$S = \sum_{i=0}^n z_i * \frac{\Delta l_s * \cos^3 \alpha_i * E_i * A_i}{l_s * (1 + \nu_i * \sin^2 \alpha_i)} \quad (161)$$

3.2.2.2 Tensile Force in a Stranded Rope

The tensile force in a strand of a stranded rope is derived in the same manner as 3.2.2.1. Index i is used for a wire layer in a strand; while for a strand itself, indices j and l are used. The total number of wire layers in a strand is n_w , and the total number of strands is n_s . The wire rope tensile force and strand tensile force are calculated according to equations (162) and (163), respectively. [23]

$$S = \sum_{j=0}^{n_s} z_j * F_j * \cos \beta_j \quad (162)$$

$$F_j = \sum_{i=0}^{n_{wj}} z_{ij} * F_{ij} * \cos \alpha_{ij} \quad (163)$$

$$S = \sum_{j=0}^{n_s} z_j * \cos \beta_j * \sum_{i=0}^{n_{wj}} z_{ij} * F_{ij} * \cos \alpha_{ij} \quad (164)$$

The wire tensile force in the wire layer i of the strand layer j is calculated as:

$$F_{ij} = \frac{\Delta l_j * \cos^2 \alpha_{ij} * E_{ij} * A_{ij}}{l_j * (1 + \nu_{ij} * \sin^2 \alpha_{ij})} \quad (165)$$

For wire rope length $L = l_j * \cos \beta_j$,

$$\frac{\Delta l_j}{l_j} = \frac{\Delta L}{L} * \frac{\cos^2 \beta_j}{1 + \nu_j * \sin^2 \beta_j} \quad (166)$$

Then, equation (165) can be rewritten as:

$$F_{ij} = \frac{\Delta L}{L} * \frac{\cos^2 \beta_j}{1 + \nu_j * \sin^2 \beta_j} * \frac{\cos^2 \alpha_{ij} * E_{ij} * A_{ij}}{1 + \nu_{ij} * \sin^2 \alpha_{ij}} \quad (167)$$

The wire rope tensile force is:

$$S = \frac{\Delta L}{L} \sum_{j=0}^{n_s} z_j * \frac{\cos^3 \beta_j}{1 + \nu_j * \sin^2 \beta_j} \sum_{i=0}^{n_{wj}} z_{ij} * \frac{\cos^3 \alpha_{ij} * E_{ij} * A_{ij}}{1 + \nu_{ij} * \sin^2 \alpha_{ij}} \quad (168)$$

3.2.3 Effect of Poisson's Ratio

The effect to Poisson's ratio of the wires, winding radius and circumference is not very large compared to the stresses in the wires. For strands, as the number of wires increase, this effect reduces even more.

For example, consider a spiral rope strand consisting of 19 wires. If the Poisson's ratio is to be neglected, the tensile stress in the outer wires is greater by 2% at most, and the stress in the wire center is by 3% less than the stresses calculated taking into account the Poisson's ratio. Similarly, for a stranded rope with a steel core where the Poisson's ratio for steel can be used as $\nu_j = 0.3$, this is also true. However, for a stranded rope with fiber core, since Poisson's ratio is greater than 0.3, the effect of the Poisson's ratio is much greater due to greater contraction of the core. Still, the total effect on the wire rope is not significant. [23]

The transverse contraction of the wire helix in stranded ropes is not very easy to calculate, especially for the ones with fiber cores. Considering the small Poisson effects, one can consider ignoring the Poisson's ratio in stress calculation of wire ropes. However, since it plays a significant role in the calculation of parameters such as additional stresses, rope elongation and modulus of elasticity, the Poisson's ratio ν_j should be calculated as precisely as possible.

Below equations show the effect in tensile forces if the Poisson's ratio was neglected. As it can be clearly seen, the equations become way simpler without Poisson effect. Equation (169) gives the tensile force in a strand of a spiral rope with neglecting Poisson's ratio:

$$S = \frac{\Delta l_s}{l_s} \sum_{i=0}^{n_w} z_i * \cos^3 \alpha_i * E_i * A_i \quad (169)$$

For a stranded rope, by neglecting Poisson's ratio, the tensile force in a strand and the wire rope tensile force are given in equations (170) and (171), respectively.

$$F_j = \frac{\Delta L}{L} \sum_{i=0}^{n_{wj}} z_{ij} * \cos^2 \beta_j * \cos^3 \alpha_{ij} * E_{ij} * A_{ij} \quad (170)$$

$$S = \frac{\Delta L}{L} \sum_{j=0}^{n_s} z_j * \cos^3 \beta_j \sum_{i=0}^{n_{wj}} z_{ij} * \cos^3 \alpha_{ij} * E_{ij} * A_{ij} \quad (171)$$

3.2.4 Wire Rope Modulus of Elasticity

Even though the modulus of elasticity of a wire rope depends on the modulus of elasticity of the wire material, it is a different phenomenon describing the elongation of wire rope. Moreover, the stress-extension curve of a wire rope is not linear and thus, the modulus of elasticity is not constant.

The nonlinearity is not significant for strands and spiral wire ropes and therefore, their modulus of elasticity can be calculated analytically. On the other hand, for stranded wire ropes, due to nonlinear stress-extension curve, it is very hard to analytically calculate the modulus of elasticity. It can only be estimated with measurements and a very precise definition of loading. [23]

The modulus of elasticity for strands of a spiral rope (or spiral wire rope itself) can be calculated as shown below; where, σ_z is the wire rope tensile stress and ε is the extension of the rope or strand.

$$\sigma_z = \frac{S}{A} \quad (172)$$

$$E_s = \frac{\sigma_z}{\varepsilon} \quad (173)$$

$$\varepsilon = \frac{\Delta l_s}{l_s} \quad (174)$$

$$E_s = \frac{1}{A} * \sum_{i=0}^n z_i * \frac{\cos^3 \alpha_i * E_i * A_i}{1 + \nu_i * \sin^2 \alpha_i} \quad (175)$$

3.3 VIBRATIONAL ANALYSIS METHOD

As it can be seen from the previous chapter, the theoretical calculation of the tensile load in a cable depends on the lay angle, wire number and arrangement, and elongation in the wire rope itself. Instead of obtaining the tensile load by calculating the tension in each wire and strand, other methods such as vibrational analysis can be used to directly obtain the global tensile load.

To explain vibrational analysis method, guitar string theory can be used as an analogy. [2] The axial force in a stressed string depends on its dynamic properties such as natural frequency, f_n and mode shape, n , as well as sectional properties such as mass per unit length, m and cable length, L .

$$f_n = \frac{n}{2L} \sqrt{\frac{T}{m}} \quad (176)$$

$$T = \frac{4 * m * L^2}{n^2} f_n^2 \quad (177)$$

Sensors which are capable of measuring the vibrations, such as vibrating wire strain gauge or accelerometer, are needed to obtain the natural frequency, f_n of the cable.

Özerkan (2005) used vibrating wire strain gauges and accelerometer to collect vibrational data from the pedestrian bridge near METU exit in Eskişehir Road (Dumlupınar Boulevard). [26] Wandji (2014) used a collective data obtained by Özerkan in 2005 and data obtained by METU Structural Health Monitoring class students from years 2011, 2012 and 2013, to prepare a comparative study of the same pedestrian bridge vibrational analysis. [2] Even though the METU pedestrian bridge cables are not wire ropes as mainly targeted in this thesis, but solid steel wires, still the same study can be used for either type of cable in determining the cable tension.

After the vibrational data of the cables are collected, the data is converted to frequency domain and the Fast Fourier Transform (FFT) is conducted. The FFT analysis yields to absolute and imaginary values. To determine the natural frequency, peak values at absolute and imaginary values should be investigated. The peak frequency value common for both absolute and imaginary parts is the natural frequency value of the subject concerned. For a cable, the natural frequency f_n can be obtained by analyzing the vibrational data with FFT and determining peak values. Then this value for the considered mode can be input in equation (177) to obtain the cable tension.

However, equation (177) underestimates the dynamic behavior of a real cable system since it is based on string. [26] This is due to the fact that real cables have more complicated properties such as modulus of elasticity as aforementioned in 3.2.4, a greater cross-sectional area, moment of inertia, etc. compared to a simple string. Thus, Zui et al. (1996) modified this equation to include more properties of cables. [27]

$$T = \frac{4w(L * f_n)^2}{n^2 * g} \left[1 - 2.20 \frac{c}{f_n} - 0.550 \left(\frac{c}{f_n} \right)^2 \right] \quad (178)$$

for $\xi \geq 17$

$$T = \frac{4w(L * f_n)^2}{n^2 * g} \left[0.865 - 11.6 \left(\frac{c}{f_n} \right)^2 \right] \quad (179)$$

for $6 \leq \xi \leq 17$

$$T = \frac{4w(L * f_n)^2}{n^2 * g} \left[0.828 - 10.5 \left(\frac{c}{f_n} \right)^2 \right] \quad (180)$$

for $0 \leq \xi \leq 6$

$$T = \frac{4w(L * f_n)^2}{n^2 * g} \left[1 - 4.40 \frac{c}{f_n} - 1.1 \left(\frac{c}{f_n} \right)^2 \right] \quad (181)$$

for $\xi \geq 60$

$$T = \frac{4w(L * f_n)^2}{n^2 * g} \left[1.03 - 6.33 \frac{c}{f_n} - 1.58 \left(\frac{c}{f_n} \right)^2 \right] \quad (182)$$

for $60 \leq \xi \leq 17$

$$T = \frac{4w(L * f_n)^2}{n^2 * g} \left[0.882 - 85 \left(\frac{c}{f_n} \right)^2 \right] \quad (183)$$

for $0 \leq \xi \leq 17$

$$c = \sqrt{EIg/wL^4} \quad (184)$$

$$\xi = L\sqrt{T/EI} \quad (185)$$

By using these modified equations, cable tension force can be calculated more realistically. However, this method is still based on a more comprehensive data collecting and analysis. The cable tension measuring device developed is a simpler device for in-situ use and direct results. See 3.4 and 3.5 for more detail on development of the device.

3.4 DEVICE WORKING PRINCIPLES

The cable tension measurement device working principle is simply based on beam deflection theory. When a slender and easy to deflect beam is connected from the ends to a stressed cable, if there is an obstacle attached to beam, it will cause to beam and cable to deflect at the attachment point in opposite directions. Since the circular obstacle limits the maximum deflection in the middle, it can be said that the total deflection in the middle is the sum of beam maximum deflection at mid-span and cable deflection. Moreover, the laser pointer attached at one end will project onto the ruler, which is attached to the other end of the beam in perpendicular orientation. The laser point on the ruler will make it possible to calculate of the deflected beam's slope at the ends. The tensile force in the cable can be calculated by using i) the compatibility equation at the mid-span, ii) beam slope, and iii) force relations from the free-body diagram. Figure 58 below gives a figurative description of the setup in free and attached states.

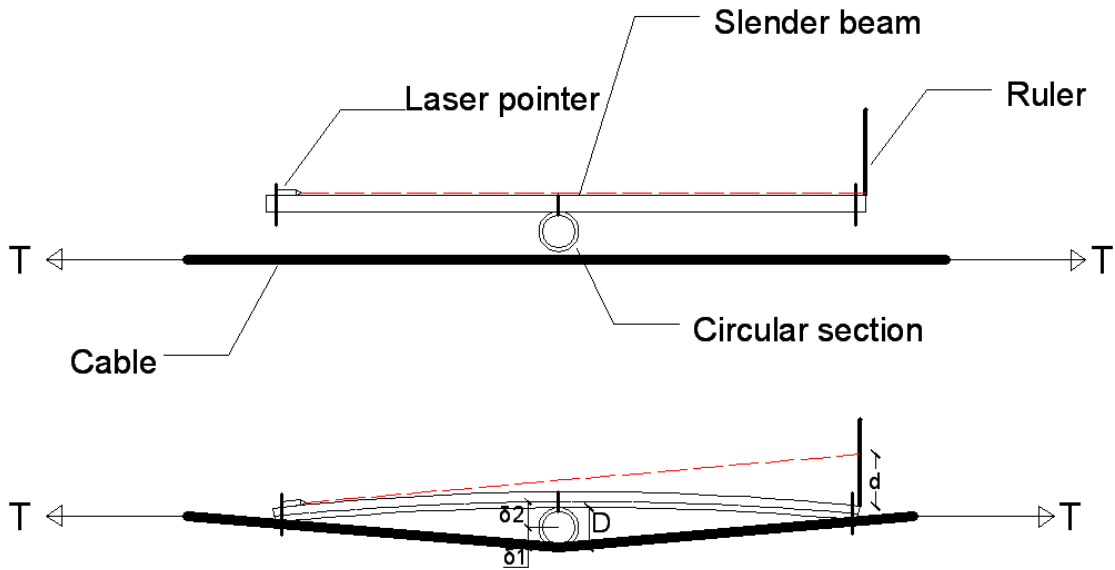


Figure 58. Cable tension measurement device at free and attached states

3.4.1 Governing Equations

The equations of the cable tensile force are obtained as given in the following equations. First, the free-body diagrams of the beam and cable in beam-attached state are obtained, as given in Figure 59.

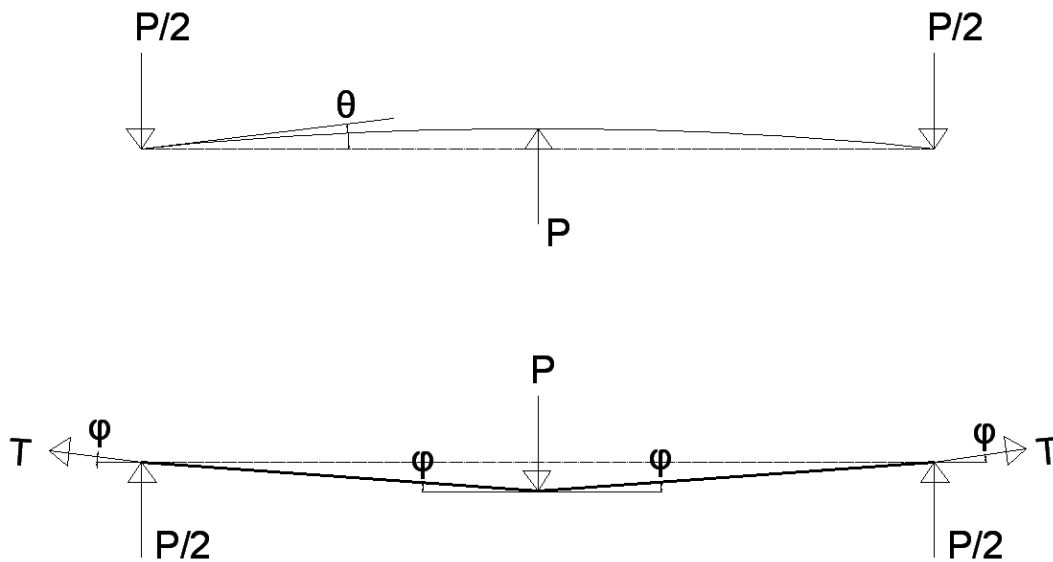


Figure 59. Free-body diagrams of beam and cable

As it can be seen from Figure 59, the total deflection at the mid-span of the setup is equal to circular section diameter. This is the first compatibility equation.

$$\delta_1 + \delta_2 = D \quad (186)$$

Where, δ_1 is the cable deflection and δ_2 is the beam deflection. Cable deflection δ_1 can be directly calculated through force relations from free-body diagram. P is the force applied at mid-point due to circular section, and T is the cable tension.

$$\frac{\delta_1}{L/2} = \tan \varphi \quad (187)$$

$$\tan \varphi = \frac{P/2}{T} \quad (188)$$

$$P = \frac{\delta_1 * 4T}{L} \quad (189)$$

$$\delta_1 = \frac{PL}{4T} \quad (190)$$

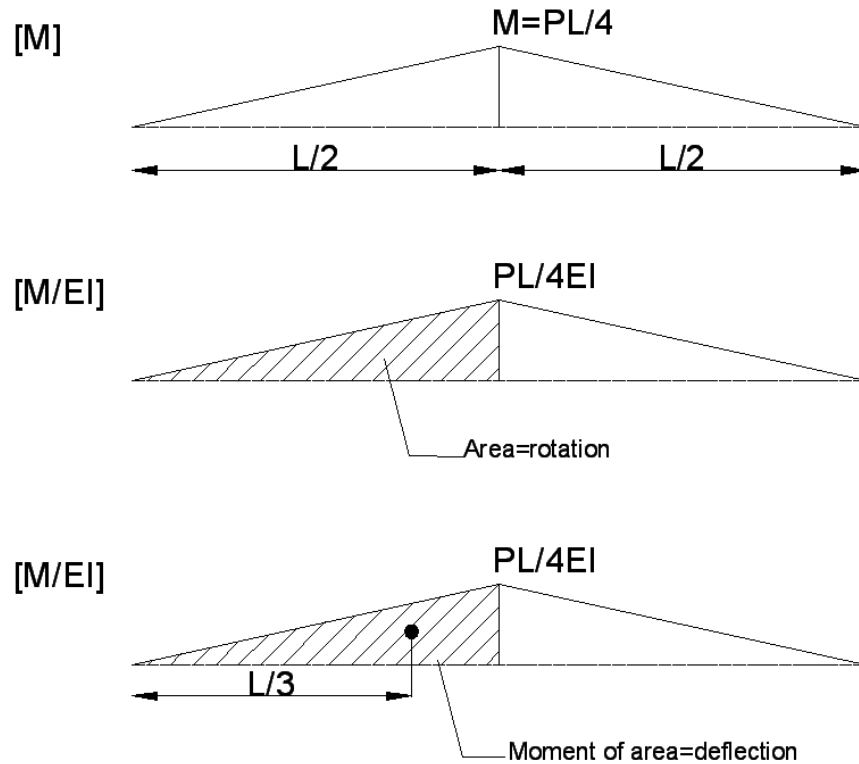


Figure 60. Calculation of beam deflection from moment-area theorem

The rotation of the beam at one end, as well as the slope, can be calculated through moment-area theorem (see Figure 60). Area under moment/curvature, M/EI , graph gives the deflection at the concerned end. If small angle theory can be used, then the slope is equal to rotation multiplied by the distance, since rotation angle is small. Moreover, maximum beam deflection can be calculated by taking the moment of the

area under M/EI diagram according to the considered reference point. [28] This way, beam deflection δ_2 can be calculated.

$$\theta = \left(\frac{PL}{4EI}\right) * \left(\frac{L}{2}\right) * \frac{1}{2} = \frac{PL^2}{16EI} \quad (191)$$

$$\theta = \frac{d}{L}, \quad d = \theta * L \quad (192)$$

$$d = \frac{PL^3}{16EI} \quad (193)$$

$$P = \frac{16EI}{L^3} d \quad (194)$$

$$\delta_2 = \left[\left(\frac{PL}{4EI}\right) * \left(\frac{L}{2}\right) * \frac{1}{2} * \frac{L}{3}\right] = \frac{PL^3}{48EI} \quad (195)$$

By rewriting equation (186):

$$\delta_1 + \delta_2 = \frac{PL}{4T} + \frac{PL^3}{48EI} = D \quad (196)$$

$$\frac{\left(\frac{16EI}{L^3} d\right) L}{4T} + \frac{\left(\frac{16EI}{L^3} d\right) L^3}{48EI} = D \quad (197)$$

$$\frac{4EI}{L^2} d \frac{1}{T} + \frac{d}{3} = D \quad (198)$$

$$d \left(\frac{4EI}{L^2} \frac{1}{T} + \frac{1}{3}\right) = D \quad (199)$$

$$T = \frac{4EI/L^2}{\left(\frac{D}{d} - \frac{1}{3}\right)} \quad (200)$$

Equation (200) gives the cable tension as a function of beam stiffness, beam length, circular section diameter and laser measurement.

3.4.2 Modification of equations by real dimensions

The calculations shown in the previous section are valid for 1-D beam and cable sizes. However, in actual case, the center-to-center distances should be used for 2-D case. Thus, the equations above should be modified for real beam and cable dimensions, as well as the initial distance between the cable and beam ends.

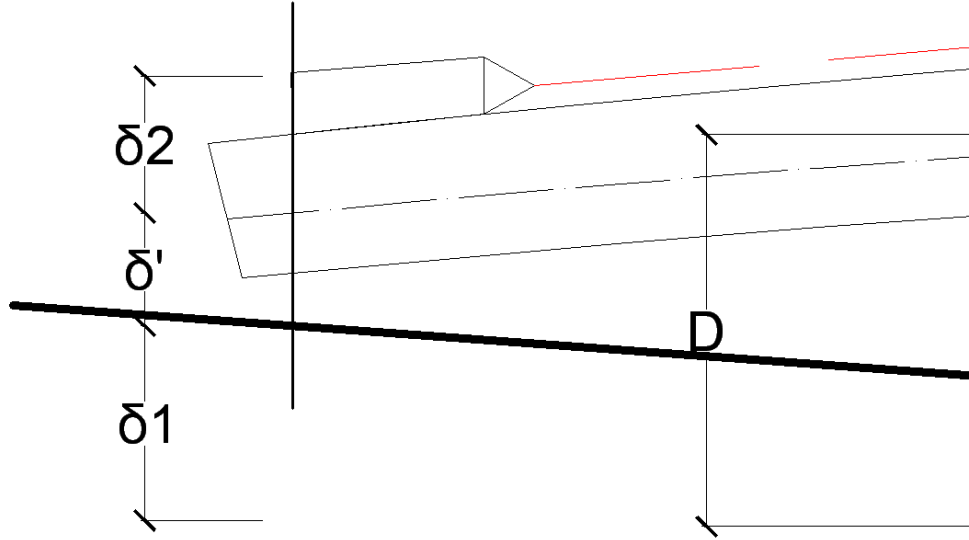


Figure 61. Distance between beam and cable in test setup

The modification should be applied such that the equations given in 3.4.1 will also include the real dimensions of the beam and cable. This is also illustrated with Figure 61. Here, δ' is the distance between beam and cable.

$$\delta_1 + \delta_2 + \delta' = D + \frac{d, \text{cable}}{2} + \frac{h, \text{beam}}{2} \quad (201)$$

$$D = \delta_1 + \delta_2 + \delta' - \frac{d, \text{cable}}{2} - \frac{h, \text{beam}}{2} \quad (202)$$

$$\frac{PL}{4T} + \frac{PL^3}{48EI} = D + \frac{d, \text{cable}}{2} + \frac{h, \text{beam}}{2} - \delta' \quad (203)$$

$$\frac{\left(\frac{16EI}{L^3}d\right)L}{4T} + \frac{\left(\frac{16EI}{L^3}d\right)L^3}{48EI} = D + \frac{d, \text{cable}}{2} + \frac{h, \text{beam}}{2} - \delta' \quad (204)$$

$$\frac{4EI}{L^2}d \frac{1}{T} + \frac{d}{3} = D + \frac{d, \text{cable}}{2} + \frac{h, \text{beam}}{2} - \delta' \quad (205)$$

$$d \left(\frac{4EI}{L^2} \frac{1}{T} + \frac{1}{3} \right) = D + \frac{d, \text{cable}}{2} + \frac{h, \text{beam}}{2} - \delta' \quad (206)$$

$$T = \frac{4EI/L^2}{\left(\frac{D + \frac{d, \text{cable}}{2} + \frac{h, \text{beam}}{2} - \delta' - \frac{1}{3}}{d} \right)} \quad (207)$$

3.5 ANALYTICAL STUDIES

In this section, the sizing of the beams and circular section and material choosing for prototype test is explained.

3.5.1 Optimization of member dimensions

The optimum dimensions of the prototypes were determined by considering the following factors:

- Beam yielding
- Mobility of the device
- Maximum tension which can be measured

As it can be seen from the calculations in 3.4.1 and 3.4.2, the tensile load which can be measured depends on the beam stiffness and length, diameter of the circular section and laser measurements. From these variables, the ones which can be optimized to obtain better results are circular section and beam properties.

The circular section diameter D affects the tensile load such that if a small diameter circular section is used, a greater tension value can be measured corresponding to the same applied load P .

The beam length L also affects the tensile load and also beam moments created due to P . Moreover, the length of the beam is also the length of the device, and for easy installation and mobility, L is limited between 1 to 1.5 meters.

The beam dimensions are effective in determining both the tensile force through stiffness EI , and also in the beam bending strength. It is preferable for the beam to be as slender as possible so that it can deflect easily and the cable force measurement can be easily made. However, if it becomes too slender and yields due to bending before the measurements are completed, it would be useless. Therefore, beam dimensions are optimized by considering these two aspects.

The beam material quality is another factor to be considered. For increasing the yield strength of the beam without increasing the beam dimensions too much, high strength steel materials (e.g. S355) can be preferred.

First optimization study was conducted for a number of rectangular hollow section profiles for beam; first fixing the beam length and circular section diameter, and then fixing the beam material quality and circular section diameter. In these preliminary calculations, a circular section diameter of $D = 48.3 \text{ mm}$ pipe profile was selected. The beam lengths $L = 1000 \text{ mm}$ and $L = 1500 \text{ mm}$ were tried first for different beam sections. Then, the beam material qualities of S235 (St37) and S350 (St52) were tried.

In these preliminary optimization trials, applied load due to installation of the device, P was limited to 15 kN since it would be very difficult to fix the beam onto the cable even without a hydraulic jack. Also, another limitation was the beam yield strength as also explained above. Informative graphs showing the applied load P versus the measured tension T for preliminary optimization are given in the Appendix B.

The optimization was done by considering the factors explained above and the data obtained from the P vs T graphs for the first optimization. The final prototype dimensions and the forces obtained are explained graphically in the following section.

3.5.2 Prototype calculations

After the optimization of the member dimensions, the final member sizes are fixed as:

- Beam length, $L = 1500 \text{ mm}$. After cutting the full length profile, the final length used in the prototype tests is $L = 1415 \text{ mm}$.
- $D = 80 \text{ mm}$, $D = 43 \text{ mm}$, for the first and the second prototype tests, respectively.
- Beam material quality: S235 (St37).
- Beam profile: $40 \times 40 \times 2 \text{ mm}$ rectangular hollow section. However, after checking the profile dimensions, the actual dimensions were obtained as: $40.5 \times 40.09 \times 2 \text{ mm}$. These measured dimensions are used in the tests for better accuracy. The dimension 40.09 mm is the beam major bending dimension used in the calculations.
- Cable diameter used in the tests: $d_{cable} = 9.6 \text{ mm}$

- The distance between the beam and cable in the test setup is measured as $\delta' = 30 \text{ mm}$ in both setups since the end connections are the same.

Numerical calculations for each prototype are presented in the following pages.

3.5.2.1 Prototype 1: D=80 mm

Data used in calculations are provided in Table 4 for the first prototype.

Table 4. Prototype-1 Data

Beam	Cable	Circular Section
L = 1415 mm 40.09x40.5x2 mm I = 74482 mm ⁴ E = 210000 MPa EI = 15.6x10 ⁶ kN.mm ² $\sigma_y = 235 \text{ MPa}$	d _{cable} = 9.6 mm	D = 80 mm

Applied load P versus measured tension T, and measured tension T versus laser reading d are presented below in tabular format. For laser reading in the analytical calculations, a data range starting from 1 mm until the beam yielding point is used.

Table 5. Analytical calculation results for Prototype-1

d	P	T	M	$\sigma = My/I$
mm	kN	kN	kN.mm	MPa
1	0.09	0.42	31.2	8.4
2	0.18	0.84	62.5	16.8
3	0.26	1.27	93.7	25.2
4	0.35	1.70	125.0	33.6
5	0.44	2.13	156.2	42.0
6	0.53	2.57	187.5	50.5
7	0.62	3.01	218.7	58.9
8	0.71	3.46	250.0	67.3
9	0.79	3.91	281.2	75.7
10	0.88	4.36	312.5	84.1
11	0.97	4.82	343.7	92.5
12	1.06	5.28	375.0	100.9
13	1.15	5.75	406.2	109.3
14	1.24	6.22	437.5	117.7
15	1.32	6.70	468.7	126.1
16	1.41	7.18	500.0	134.6

Table 5. (Continued)

17	1.50	7.66	531.2	143.0
18	1.59	8.15	562.5	151.4
19	1.68	8.65	593.7	159.8
20	1.77	9.15	625.0	168.2
21	1.85	9.65	656.2	176.6
22	1.94	10.16	687.5	185.0
23	2.03	10.67	718.7	193.4
24	2.12	11.19	749.9	201.8
25	2.21	11.72	781.2	210.2
26	2.30	12.25	812.4	218.6
27	2.38	12.78	843.7	227.1
28	2.47	13.32	874.9	235.5 > σ_y

The data presented in Table 5 shows that, for this member configuration, a tensile load of $T=12.78$ kN can be measured by applying a load $P=2.38$ kN in the installation of the device. The device installation can be done by the help of a simple floor hydraulic jack. This issue will be discussed in detail in 3.7.

3.5.2.2 Prototype 2: $D=43$ mm

Data used in calculations are provided in Table 6 for the second prototype.

Table 6. Prototype-2 Data

Beam	Cable	Circular Section
$L = 1415$ mm $40.09 \times 40.5 \times 2$ mm $I = 74482$ mm ⁴ $E = 210000$ MPa $EI = 15.6 \times 10^6$ kN. mm ² $\sigma_y = 235$ MPa	$d_{\text{cable}} = 9.6$ mm	$D = 43$ mm

Applied load P versus measured tension T graph, and measured tension T versus laser reading d are presented below. For laser reading in the analytical calculations, a data range starting from 1 mm until the beam yielding point is used.

Table 7. Analytical calculation results for Prototype-2

d	P	T	M	$\sigma=My/I$
mm	kN	kN	kN.mm	MPa
1	0.09	0.83	31.2	8.4
2	0.18	1.67	62.5	16.8
3	0.26	2.53	93.7	25.2
4	0.35	3.41	125.0	33.6
5	0.44	4.30	156.2	42.0
6	0.53	5.21	187.5	50.5
7	0.62	6.13	218.7	58.9
8	0.71	7.07	250.0	67.3
9	0.79	8.04	281.2	75.7
10	0.88	9.01	312.5	84.1
11	0.97	10.01	343.7	92.5
12	1.06	11.03	375.0	100.9
13	1.15	12.07	406.2	109.3
14	1.24	13.12	437.5	117.7
15	1.32	14.20	468.7	126.1
16	1.41	15.31	500.0	134.6
17	1.50	16.43	531.2	143.0
18	1.59	17.58	562.5	151.4
19	1.68	18.75	593.7	159.8
20	1.77	19.95	625.0	168.2
21	1.85	21.17	656.2	176.6
22	1.94	22.42	687.5	185.0
23	2.03	23.69	718.7	193.4
24	2.12	25.00	749.9	201.8
25	2.21	26.33	781.2	210.2
26	2.30	27.70	812.4	218.6
27	2.38	29.09	843.7	227.1
28	2.47	30.52	874.9	235.5 > σ_y

The data presented in Table 7 shows that, for this member configuration, a tensile load of T=29.09 kN can be measured by applying a load P=2.47 kN in the installation of the device. The device installation can be done by the help of a simple floor hydraulic jack. This issue will also be discussed in detail in 3.7.

3.6 LABORATORY TESTS

Two prototypes were set up and tested in the laboratory to verify the analytical studies. In both of the prototypes, same beam section and length was used, but the circular section diameter is changed. For the first setup, a circular section with diameter $D = 80 \text{ mm}$ was used; while, for the second test setup, the circular section was changed to $D = 43 \text{ mm}$. Installation and test procedure is the same for both tests. The results for both tests will be given in detail, separately.

The cable used was at first free. It was tied to S-type load cell attached to the cylinder hydraulic jack and this assembly was connected with a pin support to laboratory floor. Figure 62 shows this assembly when cable is loose. Figure 63 shows the whole setup when cable was loose and beam was not installed yet. The both ends of the cable were connected with pin supports, one to the floor and the other to the wall.

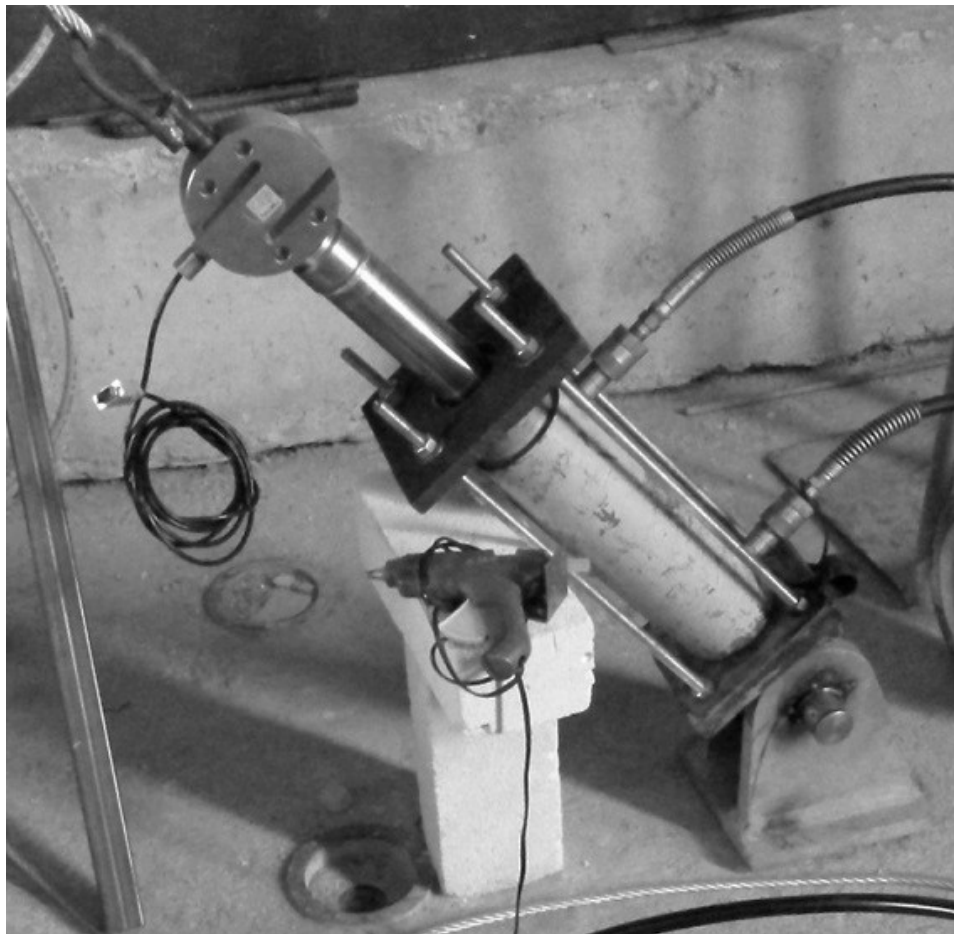


Figure 62. Cable - load cell - hydraulic jack assembly

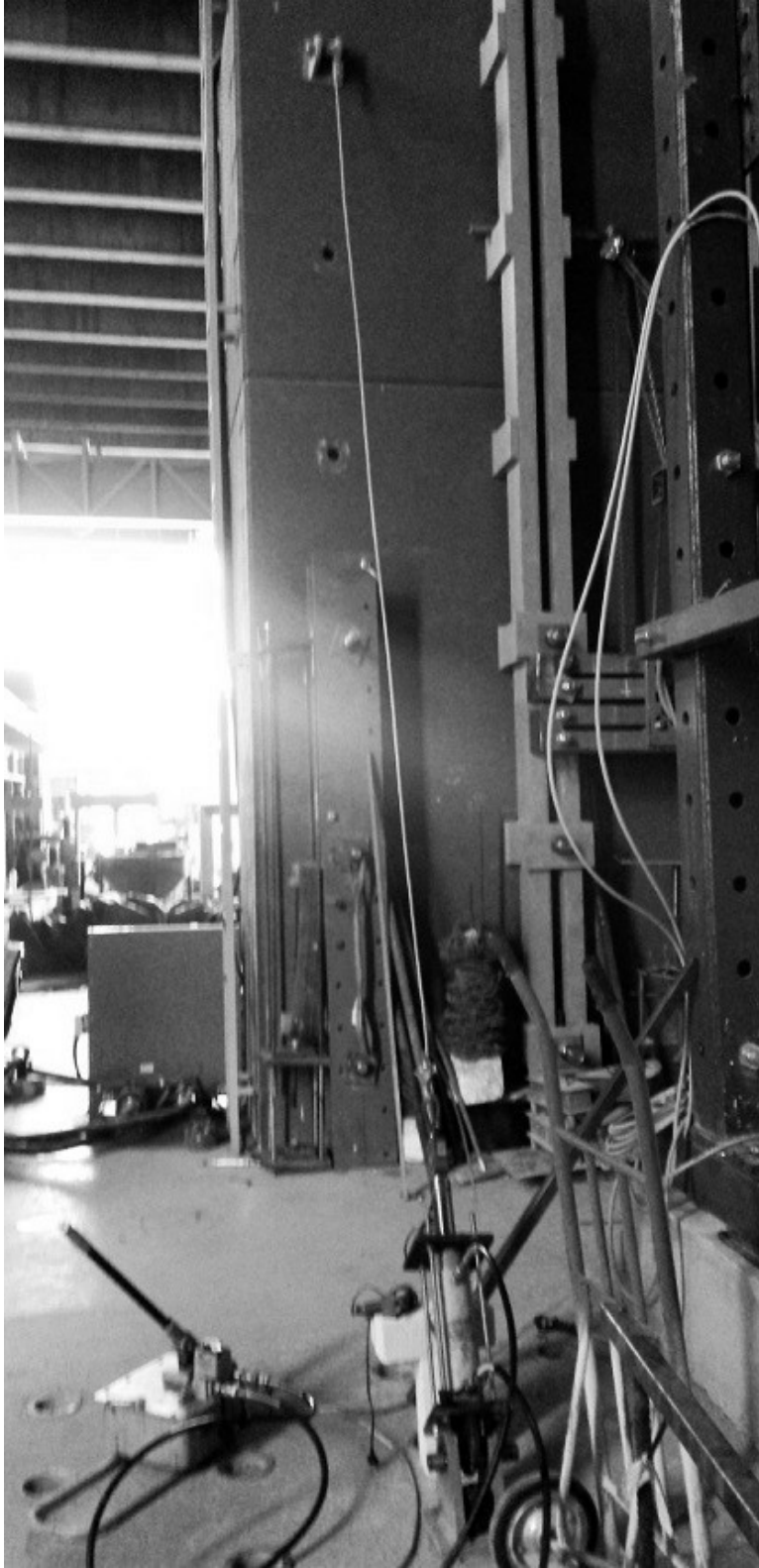


Figure 63. Test setup with beam not yet installed

After the installation of the cable - load cell - hydraulic jack assembly was completed, the slender beam with circular section attached was connected to the

cable with horseshoe connectors as seen in Figure 64. The detail of the circular section and the horseshoe connectors can be seen in Figure 65 and Figure 66, respectively. The beam ends were tightly fit into these connectors which did not allow the slipping of beam when the cable was stressed. Also, the connector fixation pins were engraved a niche with the turning machine to allow free slipping of the cable on this niche. This way, the beam end were fixed to the connectors, but since the connectors allowed free movement of the cable the cable is only stressed in the middle where the circular section was attached. The end connectors were attached very close to the beam ends so as not to change the analytically calculated behavior of the beam, as it can be seen from Figure 67.

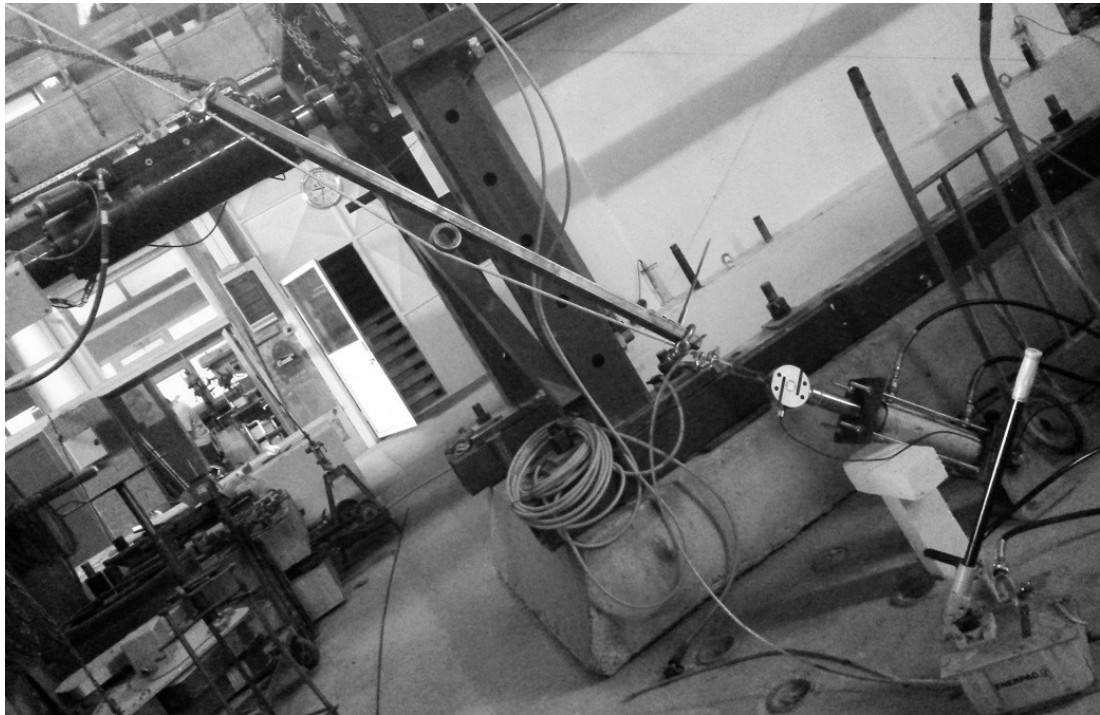


Figure 64. Test setup with beam installed

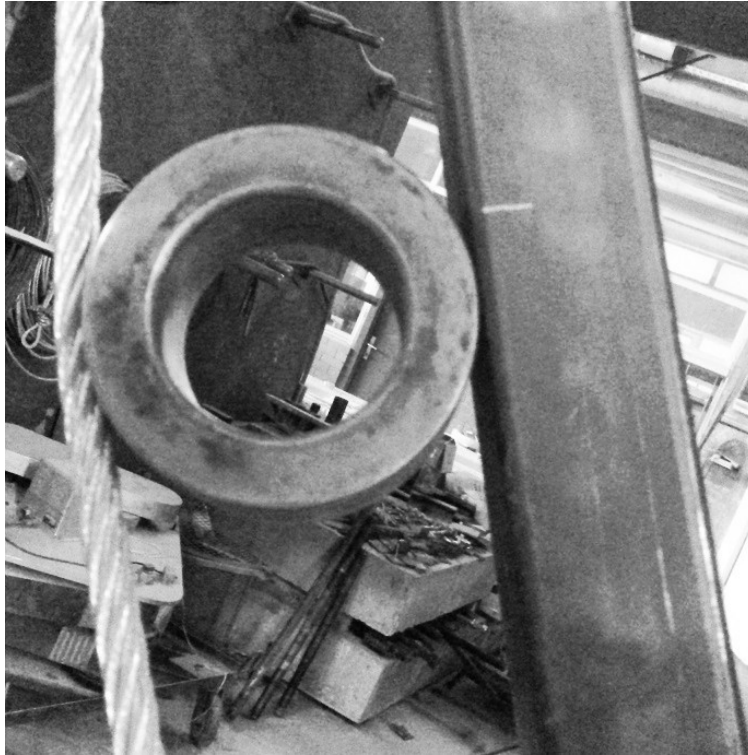


Figure 65. Detail of circular section in the middle

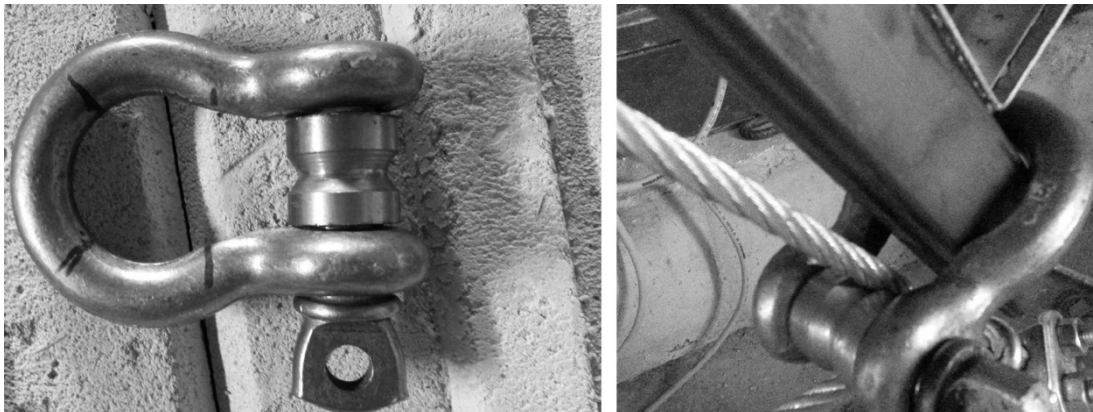


Figure 66. End connectors

After the installation, the cable was loaded through the floor hydraulic jack which was connected to the cylinder hydraulic jack. The floor jack was loaded and it compressed the cylinder jack and thus, the cable was stressed. The tensile load values read from the load cell were recorded. Meanwhile, the laser pointer measurements on the ruler were also recorded for corresponding tensile loads. See Figure 68 and Figure 69 for the laser pointer and ruler connection details.

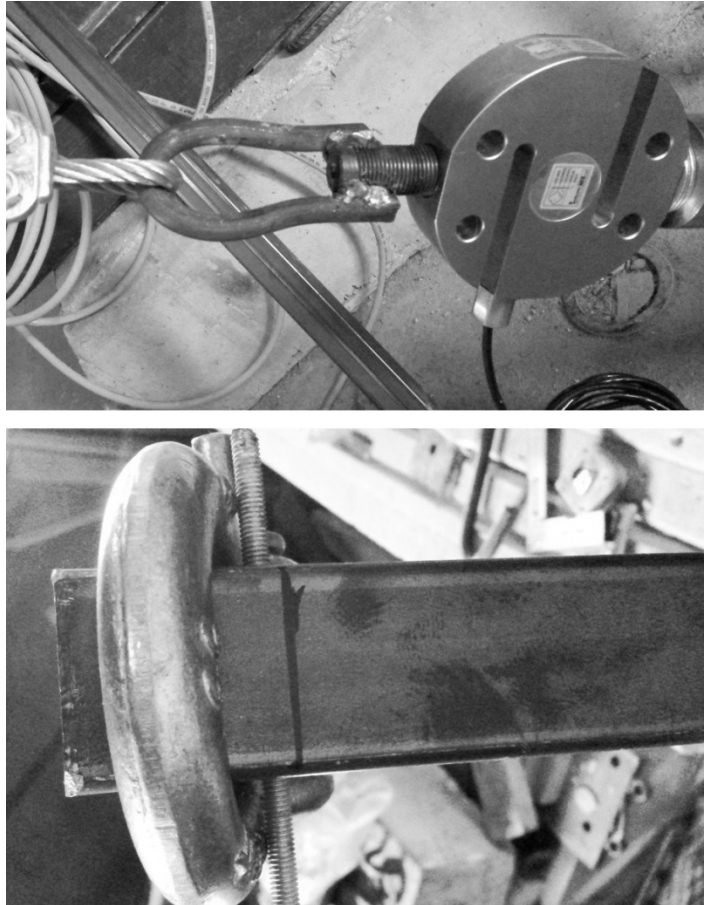


Figure 67. Top – connection of cable to load cell, Bottom – connection of beam to horseshoe connector

The loading was increased near the theoretical tensile load point where the beam can deflect without yielding, as calculated in the analytical studies. The recorded tensile load – laser measurement data were plotted to be later verified with the analytical data.

The same procedure then repeated with a different circular beam section. This time a rod with diameter $D = 43 \text{ mm}$ was used. As explained in the analytical studies, when the circular section diameter gets smaller, greater tension values can be measured. However, there are other shortcomings of the smaller diameter section in the middle which will be discussed in detail in 3.7.

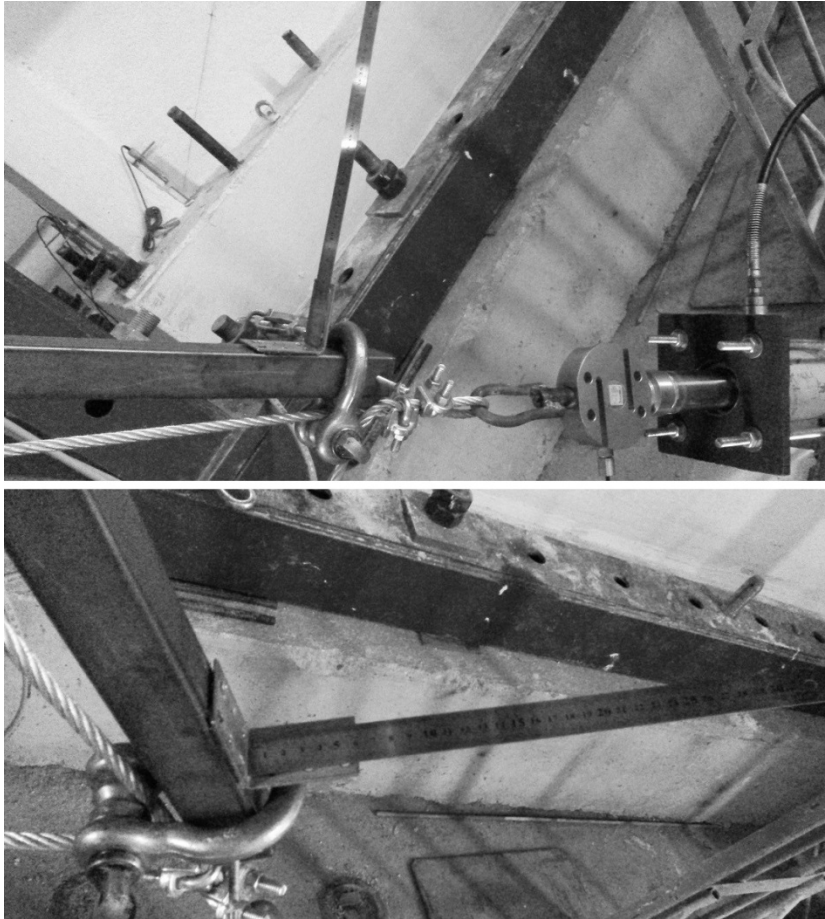


Figure 68. Top – Ruler at one end of beam, Bottom – Ruler connection detail

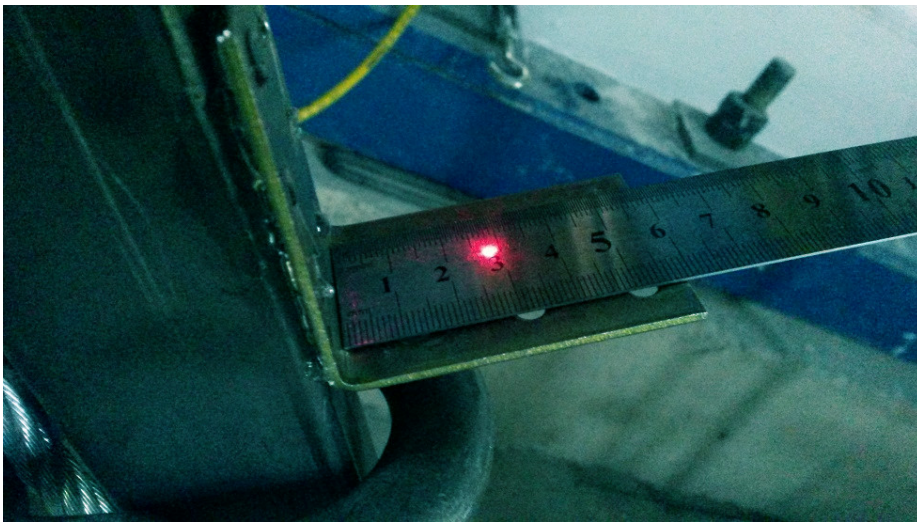


Figure 69. Laser pointer marking on ruler

3.6.1 Test results

The results obtained from the tests are presented here graphically for cable tension versus laser measurement. Measurements from tests and the analytically calculated data are drawn on the same graph for comparison, for both tests. The laser

measurement readings start from 30 mm since initially the laser reading for non-stressed cable was 30 mm due to the dimensions of setup.

3.6.1.1 Prototype 1: D=80 mm

Figure 70 shows the relation between the measurement and theoretical calculations. The measured and calculated data is very close to each other and shows linearity. As it can be seen from Figure 70, the maximum tensile load which can be measured is almost the same with the analytically calculated values.

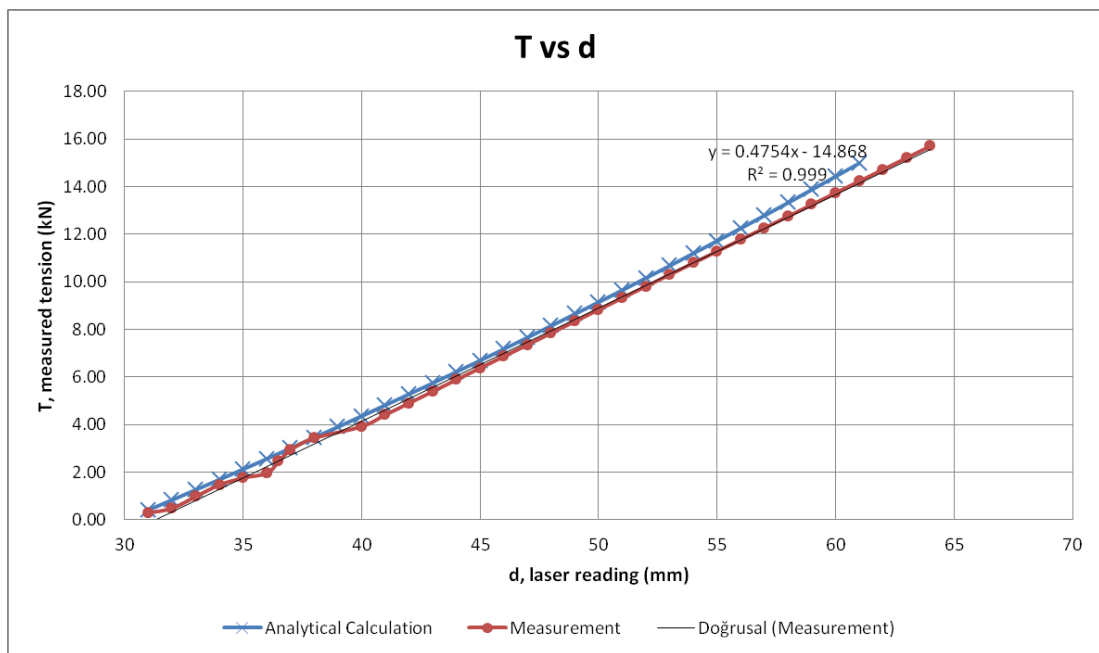


Figure 70. Test results versus theory, D=80 mm

3.6.1.2 Prototype 1: D=43 mm

Figure 71 shows the relation between the measurement and theoretical calculations. The measured and calculated data diverges from each other as the load increases. The divergence in the data will be discussed in 3.7.

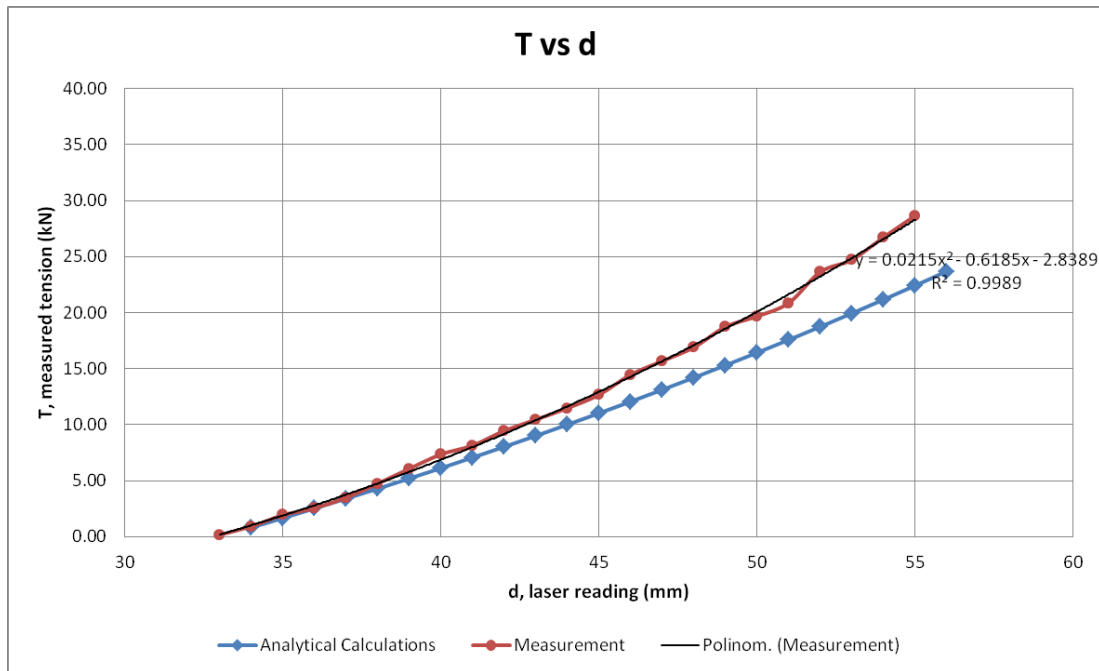


Figure 71. Test results versus theory, D=43 mm

3.7 DISCUSSION OF RESULTS

The results of the tests are presented in 3.6.1 for both prototypes. The discussion of results of tests and the comparison between the tests and analytical calculations are presented in this section.

As it can be seen from Figure 70 and Figure 71, the test results and analytical calculations are consistent with each other, especially for the first test with $D = 80 \text{ mm}$. However, for the second test with $D = 43 \text{ mm}$, as the load in the cable increased, the measured data diverged from the analytically calculated data. The main reason for this difference can be the end effects due to connection. A modification factor for end effects is applied which will be discussed in the following paragraphs.

End moment effect: The analytical calculations were conducted assuming the end connections of the beam are perfect pin. However, the horseshoe connectors at the ends, as it can be seen from Figure 66, were not allowing the full rotation of the beam ends. This is due to the fact that the beam ends were perfectly fitting inside the

horseshoe connectors. Therefore, at the connection points the beam ends were observed to be more rigid by a small amount than the analytical model.

It can be said that, this small end rigidity may have caused small end moments in the beam which was not taken into account in the analytical calculations. However, the exact end moment magnitude cannot be estimated since the rigidity of the connection is unknown. Therefore, a modification factor α_m is introduced. $\alpha_m \leq 1.0$ is applied to the rotation formula to decrease it by a small amount and thus, the slope and the maximum deflection were also decreased by α_m .

$$\theta = \frac{PL^2}{16EI} * \alpha_m \quad (208)$$

$$d = \frac{PL^3}{16EI} * \alpha_m \quad (209)$$

$$P = \frac{16EI}{L^3} * \frac{d}{\alpha_m} \quad (210)$$

When this modification factor is applied to the analytical data, the graphs showing the comparison between the test results and the analytical data took the form in Figure 72 and Figure 73, as seen below.

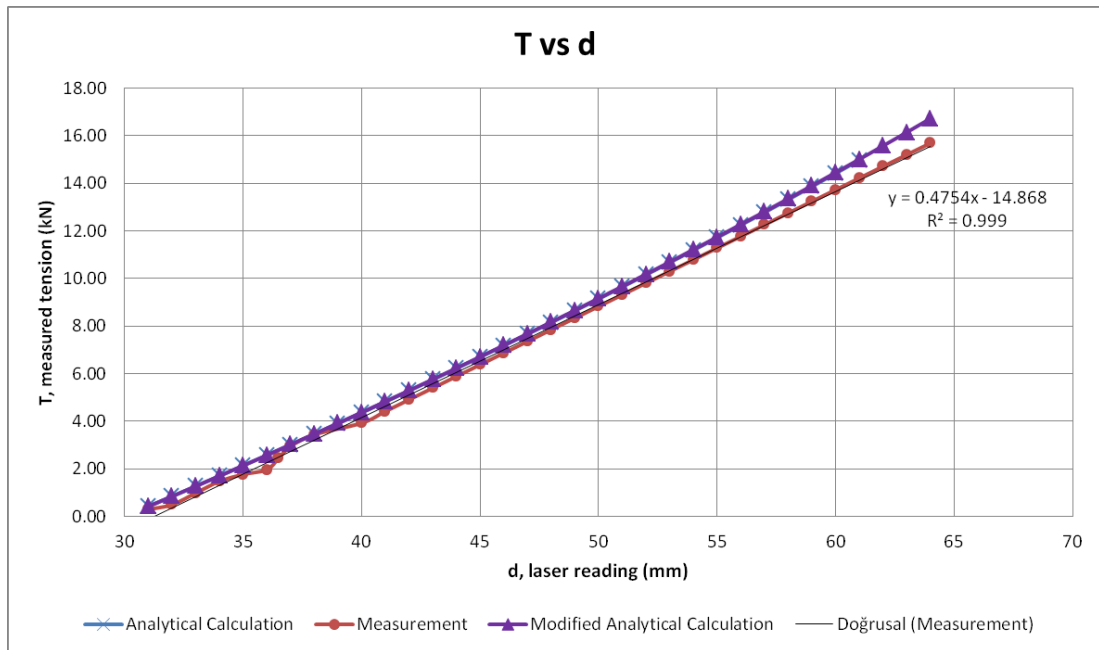


Figure 72. Test results versus modified theory, D=80 mm

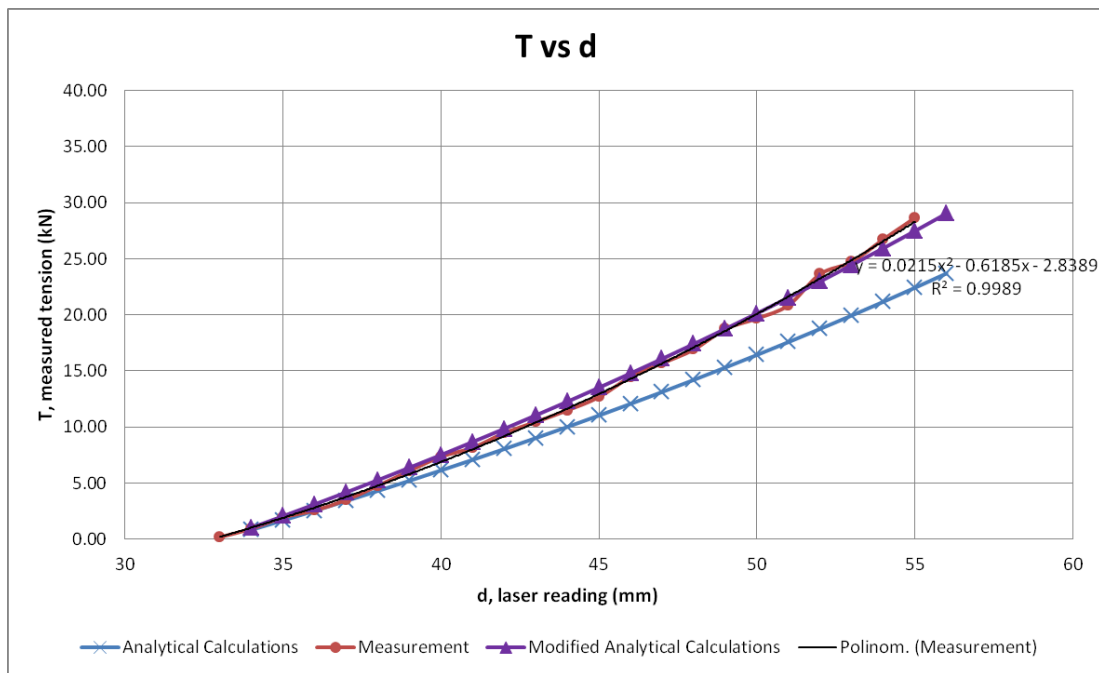


Figure 73. Test results versus modified theory, D=43 mm

As it can be seen from Figure 72, since the analytical tension value and the measured tension value are almost the same, no modification was necessary for the first prototype with $D = 80 \text{ mm}$. However, for the second test prototype with $D = 43 \text{ mm}$, modification factor of $\alpha_m = 0.82$ is applied. Modified results for the second test can be seen in Figure 73.

These results imply that the larger diameter circular section works better and affected less from the end effects. This may be due to the fact that the amount of tensile force which can be measured is smaller with larger diameter section. As the tensile force increases, the load P , and thus, the end moments become greater. This can also be observed in Figure 73. The divergence of the measurement and analytical data starts and proceeds at greater tensile force values. It should be noted that modification factor would not be necessary for a system with a constant weight connected to it, such as an elevator, since in this case the cable can move in the direction of hanged weight.

Fixation of the beam on cable: This issue concerns both the end connection detail, and the load which should be applied in installation procedure. As previously discussed, horseshoe connectors might cause small end moments if the tensile force on cable is high. Another issue about fixation is that a load P should be applied to

install the beam onto the cable. Figure 74 and Figure 75 show the applied load versus measured tension relation.

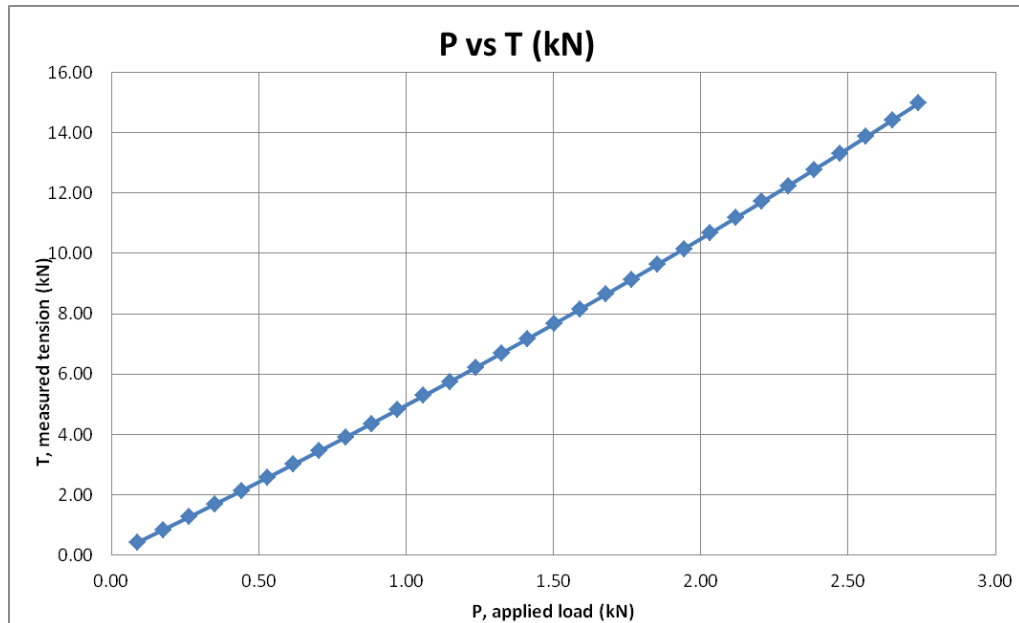


Figure 74. Applied load versus Measured Tension, D=80 mm

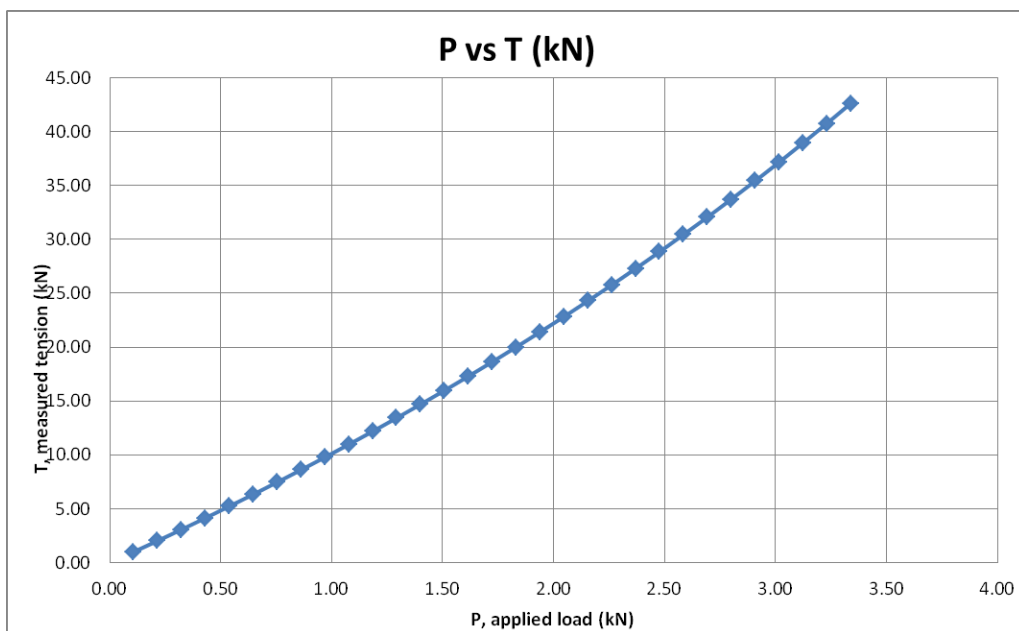


Figure 75. Applied load versus Measured Tension, D=43 mm

In the prototype tests, since the setup is installed when the cable was loosely attached and the cable was stressed later on, this issue was not a problem. However, for installing the device onto an already stressed cable, especially if the cable tensile force is high, it is suggested to use a supplementary tool. For example, a hydraulic jack can be used. Another suggestion is a system with pitched rods and nuts which

can be screwed tight. A similar system is used to fix the cylinder hydraulic jack into the cable pin end connection in Figure 62.

Resolution and accuracy: Resolution of the device in both prototypes is described as the minimum laser reading on the ruler which can be distinguished by eye, which is accepted as 0.5 mm. For this resolution, the accuracy of the readings for both tests is estimated by two methods. The first is the force based relation which is the ratio of load difference in two consecutive tensile load values to the average of these values. The second is the ratio of the resolution to the real laser measurement value. The comparison of these two measurements is presented in Figure 76 and Figure 77.

For the both tests, up to 5 mm reading, the error in readings is less than 10%; and from 10 mm reading and on, the error becomes less than 5%.

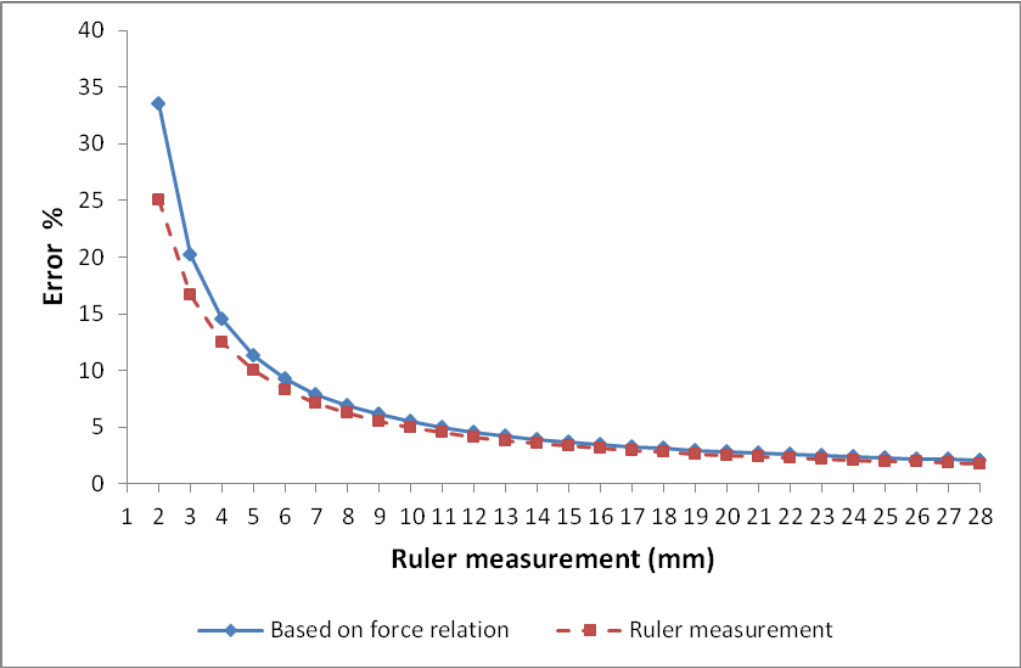


Figure 76. Accuracy of measurements in the first test with D=80 mm

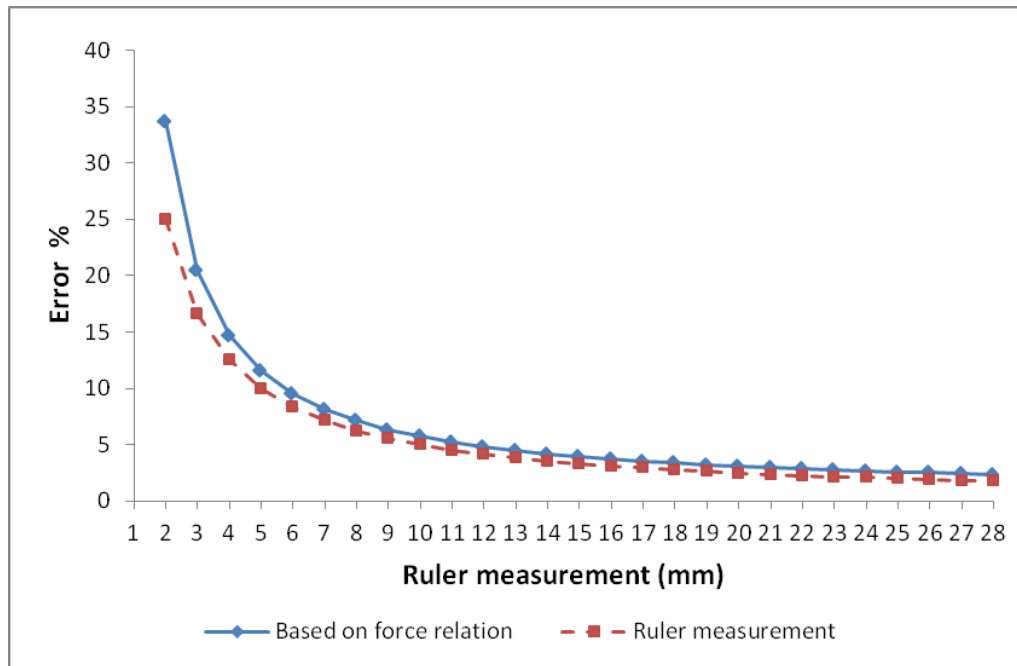


Figure 77. Accuracy of measurements in the second test with $D=43$ mm

Additional tension: Due to installation of the device, additional tension may be applied on the cable. The measurement device gives the total tension on the cable; however, it is necessary to distinguish the existing tension to be measured from the additional tension due to installation. Figure 78 below illustrates the mechanism of creating additional tension at installation.

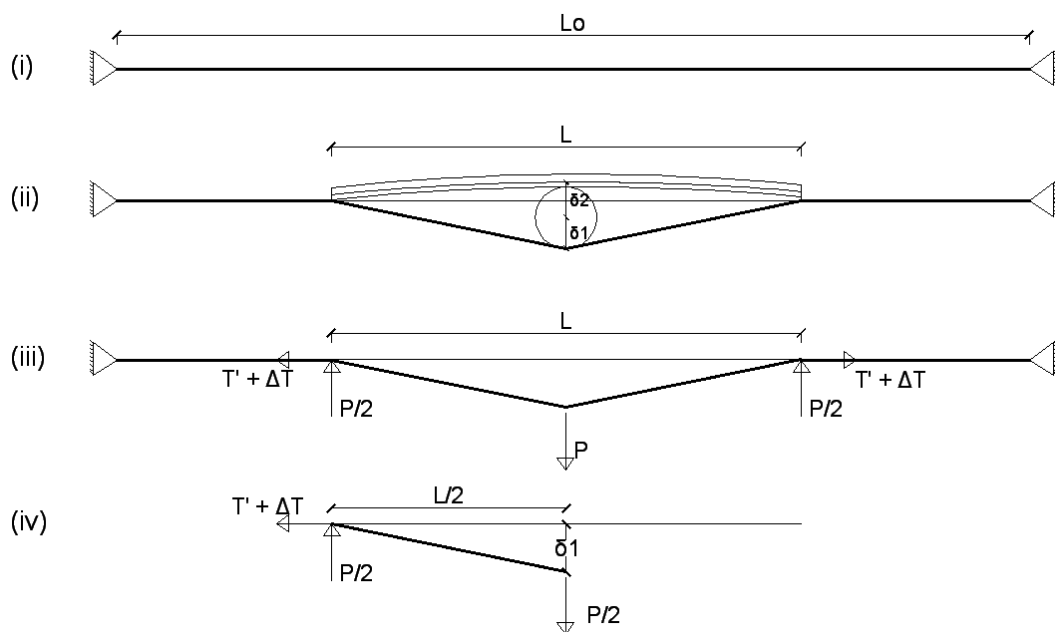


Figure 78. Additional tension relations

In Figure 78, (i) shows the full length of the cable before device installation. In (ii), after beam of length L and circular section of diameter D are installed, beam and cable deforms by an amount of δ_2 and δ_1 , respectively. By inspecting the deformed shape of cable, from (iii) and (iv), equation can be written.

$$\frac{\delta_1}{L/2} = \frac{P/2}{T + \Delta T} \quad (211)$$

A small amount of elongation will be observed in cable due to applied force P . This elongation can be obtained by using the similar triangles in Figure 78, (ii). Here, L_o is the total length of the cable used.

$$\text{Elongation} = \frac{[\sqrt{(\delta_1)^2 + (L/2)^2} - L/2] * 2}{L_o} \quad (212)$$

$$\Delta T = \frac{[\sqrt{(\delta_1)^2 + (L/2)^2} - L/2] * 2}{L_o} * E * A \quad (213)$$

$$T = T' + \Delta T = \frac{[\sqrt{(\delta_1)^2 + (L/2)^2} - L/2] * 2}{L_o} * E * A + \Delta T \quad (214)$$

Another relation can be obtained for beam deflection δ_2 .

$$P/2 = \delta_2 * 4EI/L^3 \quad (215)$$

$$\delta_2 = P/2 * \frac{L^3}{4EI} \quad (216)$$

Recall from equation (201) that;

$$\delta_2 = D + \frac{d, \text{cable}}{2} + \frac{h, \text{beam}}{2} - \delta_1 - \delta' \quad (217)$$

$$\delta'' = D + \frac{d, \text{cable}}{2} + \frac{h, \text{beam}}{2} - \delta' \quad (218)$$

$$\delta_2 = \delta'' - \delta_1 \quad (219)$$

$$P/2 = (\delta'' - \delta_1) * \frac{4EI}{L^3} \quad (220)$$

By rearranging equation (211);

$$\frac{(\delta'' - \delta_1) * \frac{4EI}{L^3}}{T' + \frac{\left[\sqrt{(\delta_1)^2 + \left(\frac{L}{2}\right)^2} - \frac{L}{2} \right] * 2}{L_0} * E * A} - \frac{\delta_1}{L/2} = 0 \quad (221)$$

Equation (221) can be solved for different cable deflection values δ_1 . Total tension $T' + \Delta T$ can be calculated by solving equations (213) and (221). Total measured tension versus existing tension graphs for Prototype-1 and Prototype-2 can be seen in Figure 79 and Figure 80.

It can be seen from Figure 79 and Figure 80 that the additional tension (ΔT) applied onto the cable due to device installation decreases as the cable existing tension becomes higher in magnitude. For higher tension values, existing tension (T') and total tension (T) values converge to each other. Another important note is that the nonlinear relationship between the measured tension and ruler measurement values in test prototypes decreases when the effect of additional tension is removed from the cable force (Figure 79 and Figure 80).

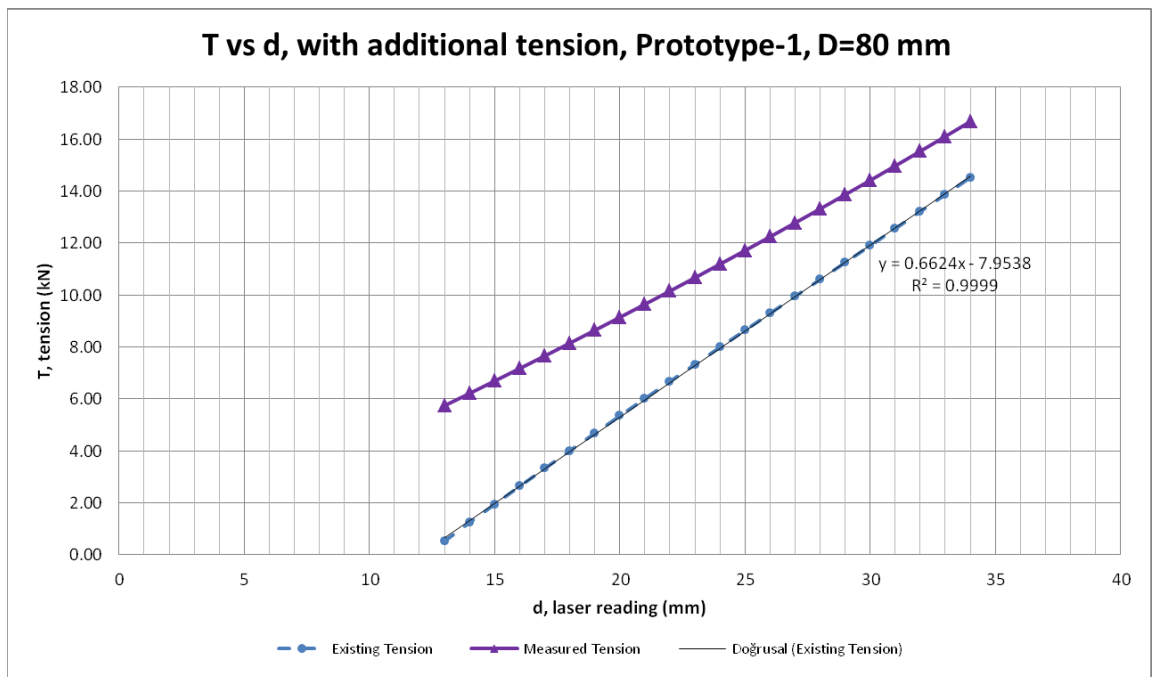


Figure 79. Measured tension and existing tension, D=80 mm

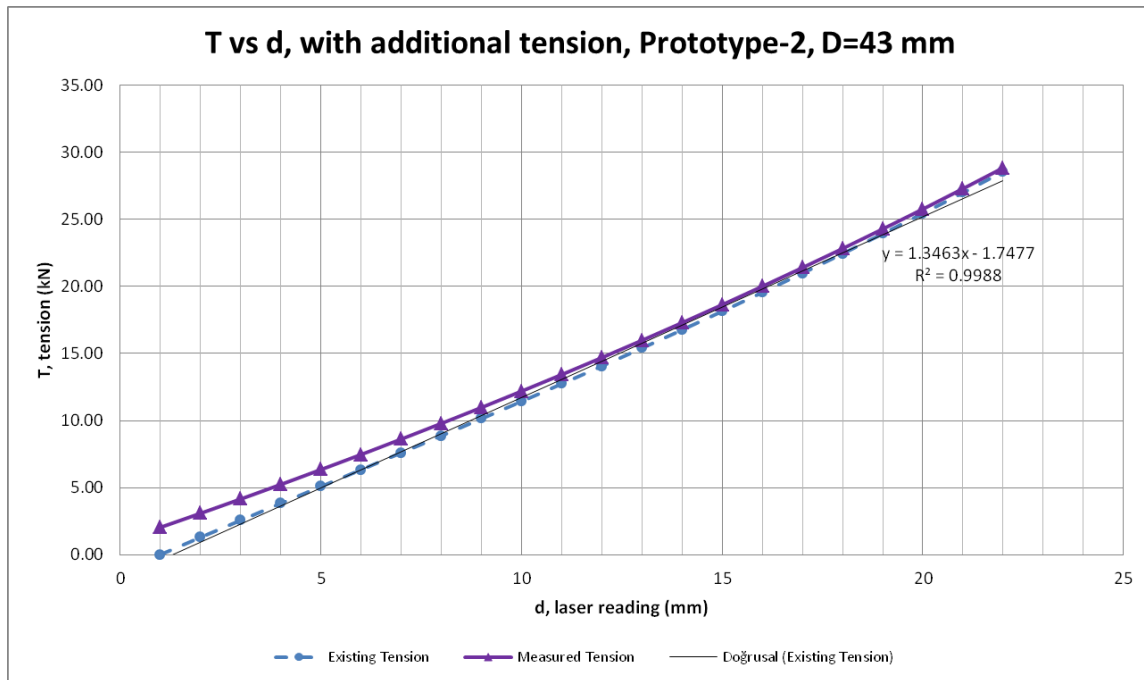


Figure 80. Measured tension and existing tension, D=43 mm

Circular section diameter effect: As also mentioned in the previous discussion, the circular section diameter affects the tensile force magnitude that can be measured. Accordingly, it is also related with the end moments created due to horseshoe connectors. As explained in the previous discussion, this effect is related with the greater tensile forces which can be observed when using a larger diameter section in the middle.

Therefore, it can be said that using large diameter circular section is preferable in end moment effect; in this configuration almost no end moments are observed. On the other hand, with a smaller diameter circular section, larger tensile forces can be measured compared to a larger diameter section. This result shows that, in optimization process, this effect should be also taken into account.

Table 8 shows the comparison of using different circular section diameters for same beam profile and cable. In this table, following properties are fixed for comparison study: beam profile of 40x40x2 mm in S235 quality, a cable of diameter $d_c=9.6$ mm and total length $L_o=10$ m, and a beam length of $L=1500$ mm. By using these properties, the values of maximum measured tension T , maximum existing tension T' , maximum additional tension ΔT , and resolution of measurement for 0.5 mm laser

reading are presented. These values can also be found in the data chart presented in Table 9 in Appendix B.

Table 8. Comparison of different circular section diameters

Circular section diameter	Max existing tension	Max total measured tension	Max applied load	Resolution of measurement	Max additional tension
D (mm)	T' (kN)	T (kN)	P (kN)	T _{res} (kN)	ΔT (kN)
20	190.08	190.09	2.26	1.00	0.18
43	30.79	30.91	2.26	0.40	1.08
80	11.80	13.17	2.26	0.20	3.33

As it can be seen from Table 8, as the circular section diameter increases, higher tensile load values can be achieved. However, the resolution of the measurement will decrease as the diameter increases. For example, for a diameter of 20 mm, the resolution (which is the tensile load which can be measured per 0.5 mm laser reading increment) is 1.00 kN while for a diameter of 80 mm, it decreases up to 0.20 kN.

On the other hand, for larger diameters, applied additional tension due to device installation increases. Smaller diameters give better results in terms of additional tension due to installation. Note that, applied load does not change with circular section diameter since it depends on the beam stiffness.

CHAPTER 4

CONCLUSIONS AND FUTURE WORK

This thesis includes analytical and experimental studies on development of two different structural health monitoring sensors for axial load carrying members. The main aim of the thesis is to establish methodology for low-cost and easy-to-use devices. The proof of concept studies developed in this thesis can be further improved and used as a guide to manufacture these sensors.

The first device developed is column buckling sensor, which consists of strain gauges in Wheatstone bridge circuit. The theoretical development stage of the buckling sensor and analytical studies were explained. Prototypes were tested in the structural mechanics laboratory to validate the theoretical design.

Tests were conducted for a pin-ended rectangular hollow section steel column both for elastic and plastic ranges. The obtained test results were close to the theoretical values of buckling with small deviations. The differences between the theoretical and experimental values were investigated and it was concluded that the end conditions in the tests were not perfect pin supports. Nevertheless, the analytical and elastic buckling test results had close agreement with each other. Different Wheatstone bridge configurations and strain gauge installation locations were proposed for different end conditions and buckling modes.

For plastic buckling tests, the test setup was improved due to instability of the supporting pedestal and this was considered as complicated end resistance and effective lengths found in actual cases and noted for possible further studies. The

main highlight of the plastic buckling tests was the end crushing before buckling. The hammered ends of the column yielded and deformed before the column buckled itself. Due to end crushing, column released some stress while loading and this delayed buckling and polluted experimental data. The analytically calculated plastic buckling load was modified to include the imperfect end conditions due to end crushing; factors of $k=0.8$ to $k=0.5$ were used to calculate the buckling load and plotted in axial load bending graphs for comparison with the experimental counterparts as seen in Figure 46 and Figure 48. There were overall good agreement between analytical and experimental values for plastic column testing. Another issue realized during plastic buckling load test is that the axial load level becomes increasingly close to the yielding force, in turn putting high levels of strain on the strain gauges. Due to this result, it is noted for future work that the strain gauges can be installed away from the mid-point or can be placed perpendicular to the loading direction just to measure transverse strains imposed by the Poisson's effect, which will be about 25% to 30% of the original strain.

As a future study for buckling sensor, different end conditions and cross-sections can be tested. The warning system can be improved, especially for existing columns. The second derivative of bending strain versus axial strain graph found to be changing sign from negative to positive or vice versa which was used to be a parameter for buckling warning.

The second device developed is cable tension measuring device, which consists of a slender beam with a circular section connected to it at the mid-point, a laser pointer at one end, and a ruler or a scale at the other end. A datasheet was prepared for different rectangular beam sections, midpoint circular section diameter, beam length, and beam material qualities. These properties were optimized by considering the mobility and installation of the device and the maximum tensile force, which can be measured. Prototypes with two different circular sections and the same beam profile and material were developed to verify the analytical studies. These prototypes were tested in laboratory to compare the results with the analytical studies.

The analytical calculations were modified to include the center-to-center distances of beam and cable in the setup. Since the beam and cable were considered as 1-D lines

in analytical calculations, the results with the tests were not exact in the beginning. When the analytical equations were modified to take into account the beam and cable dimensions and distance between these two at connection points, the results became consistent. Moreover, it was observed that the end clamps did not fully allow rotation as a simply supported beam and some end moments would be developing when the beam deforms and beam ends rotate. A modification factor was included in the calculations to take into account these end effects.

It is observed that by considering the optimized properties of the device and the test results, the cable tension measurement device may be more suitable to be used for moderately stressed cables. For higher tension values, more conventional measuring systems such as vibrating wire method or load cell in series with the cable can be used. Even if the tension range is limited to small or moderate, the device is advantageous for its own range since it can be easily used for in-situ measurement, does not have complicated electronics, robust, and the result can be directly obtained without a data analysis process. It can also be used for preliminary testing of tensile load in a cable before installing a more complicated setup.

An example data chart is given in Appendix B for different parameters such as beam dimensions, cable length, circular section diameter, etc. This chart gives the total measured tension, additional tension, and applied load for laser reading increments of 1 mm with different parameters. Intervals of 0.5 mm can be simply interpolated. Similar charts can be prepared for desired parameters for choosing device to measure tension on different cable conditions. In preparation of these charts, the procedure given in Appendix B can be used.

The end connections of the cable tension measuring device can be improved to minimize the effect of unintended end moments. Moreover, it can be investigated if it is possible to obtain larger tensile force measurements by changing the location of the circular element from mid-point to any other arbitrary points. This would also decrease the P force required to attach the beam to the cable.

REFERENCES

- [1] Types of Steel Structures - Tension Members, Compression Members, Trusses Shell etc. <http://www.aboutcivil.org/steel-structure-types-tension-compression-trusses-shell.html>, last visited on 18.08.2015
- [2] Wandji, W.N. et Türer, A. “METU Footbridge : Cable Force Determination and Dynamic Properties.” *Istanbul Bridge Conference*. Istanbul, Turkey: N.p., 2014.
- [3] Liao, W. H., D. H. Wang, and S. L. Huang. “Wireless Monitoring of Cable Tension of Cable-Stayed Bridges Using PVDF Piezoelectric Films.” *Journal of Intelligent Material Systems and Structures* 12.5 (2001): 331–339.
- [4] Vayas, I. *Stability and Ductility of Steel Elements*. J. Construct. Steel Res. Vol. 44, Nos. 1-2, pp. 23-50, 1997.
- [5] Strand Tensionmeter. <http://gmptools.com/nf/70046.htm>, last visited on 20.08.2015
- [6] CTM2 Cable Tension Meter, Data Sheet. <http://www.checkline.com/product/CTM2>, last visited 20.08.2015
- [7] Rope Tension Gauge. <http://www.qualityelev.com/main/tool/ropega.htm>, last visited 20.08.2015
- [8] World Trade Center 7 NIST Collapse Simulation Figures. http://91encyclopedia.com/wiki/index.php/World_Trade_Center_7_NIST_Collapse_Simulation, last visited on 09.05.2015
- [9] Galambos, T.V. et Surovek, A.E. *Structural Stability of Steel: Concepts and Applications for Structural Engineers*. John Wiley and Sons, Inc., 2008.
- [10] Berlin, A.A., “Active Control of Buckling Using Piezo-Ceramic Actuators.” *Smart Structures and Materials: Industrial and Commercial Applications of Smart Structures Technologies*. Vol. 2447. San Diego, CA, 1995. pp.141–154.
- [11] Ravet, F. et al. “Detection of Buckling in Steel Pipeline and Column by the Distributed Brillouin Sensor.” *Optical Fiber Technology* 12.4 (2006): 305–311.
- [12] Yoo, C.H. et Lee, S.C. *Stability of Structures Principles and Applications*. Butterworth-Heinemann, Imprint of Elsevier, 2011.
- [13] Bazant Z.P. et Cedolin, L. *Stability of Structures Elastic, Inelastic, Fracture, and Damage Theories*. World Scientific Publishing, 2010.

- [14] Johnston, B.G. *Behavior of an Inelastic Buckling Model between the Tangent Modulus and Shanley Loads*, The University of Michigan, June 1961.
- [15] Das, M.M. et Das, B.M. *Structural Analysis*. Prentice-Hall of India Pvt.Ltd, p.129-133,2011.
- [16] Walter, P. L. “Chapter 3 Bridge Transducers.” *Mechanical Engineers’ Handbook: Instrumentation, Systems, Controls, and MEMS*. 3rd ed. Vol. 2. John Wiley & Sons, Inc., 2006. pp.69–115.
- [17] Strain Gauges, Chapter 9 – Electrical Instrumentation Signals. <http://www.allaboutcircuits.com/textbook/direct-current/chpt-9/strain-gauges/>, last visited 20.08.2015
- [18] Wilson, E.J. “Chapter 17 Strain-Gage Instrumentation.” *Shock and Vibration Handbook*. Ed. Harris, C. M. McGraw-Hill, 1988. 17.1 – 17.15.
- [19] Noltingk, B. E. “Measurement of Strain.” *Instrumentation Reference Book*. Ed. Walt Boyes. 4th ed. Butterworth-Heinemann, 2009.
- [20] Kalantar-zadeh, K. *Sensors An Introductory Course*. Springer, pp. 24-31, 2013.
- [21] Pin Connector Figure. https://secure.ifai.com/sfreview/articles/0913_ss31_pin_connector.html, last visited on 01.08.2015
- [22] Modern History of Wire Rope. <http://atlantic-cable.com//Article/WireRope/Sayenga/wirerope4.htm>, last visited on 15.07.2015
- [23] Feyrer, K. *Wire Ropes*. Springer, pp.24-27, 61-130, 2007.
- [24] Wire Rope Catalog, Yarbrough LLC. http://www.yarcable.com/products/2-YCS_2015_Catalog_WireRope.pdf, last visited on 15.07.2015
- [25] Cross-Sectional Arrangements of Different Types of Wire Ropes. http://thediagram.com/13_1/crosssectional.html, last visited on 20.08.2015
- [26] Özerkan, T. *Instrumented Monitoring and Dynamic Testing of METU Cable Stayed Pedestrian Bridge and Comparisons against Analytical Model Simulations*, MSc Thesis, METU: Turkey, 2005.
- [27] Zui H., Shinke T., and Namita Y. “Practical Formulas for Estimation of Cable Tension by Vibration Method.” *ASCE Journal of Structural Engineering* 1996; 122 (6): 651-656.
- [28] Beer, F., Johnston, Jr, E.R., DeWolf, J.T., “Chapter 9 – Deflection of Beams” *Mechanics of Materials* 4th ed. McGraw-Hill, 2006. pp.569-603.

APPENDIX A

CABLE AXIAL LOAD MEASUREMENT DEVICE SUPPLEMENTARY DATA FOR OPTIMIZATION

In this part, the preliminary optimization results for different beam sections, circular sections, beam material quality and beam length are presented as supplementary information to the data given in Section 3.4 and 3.5.

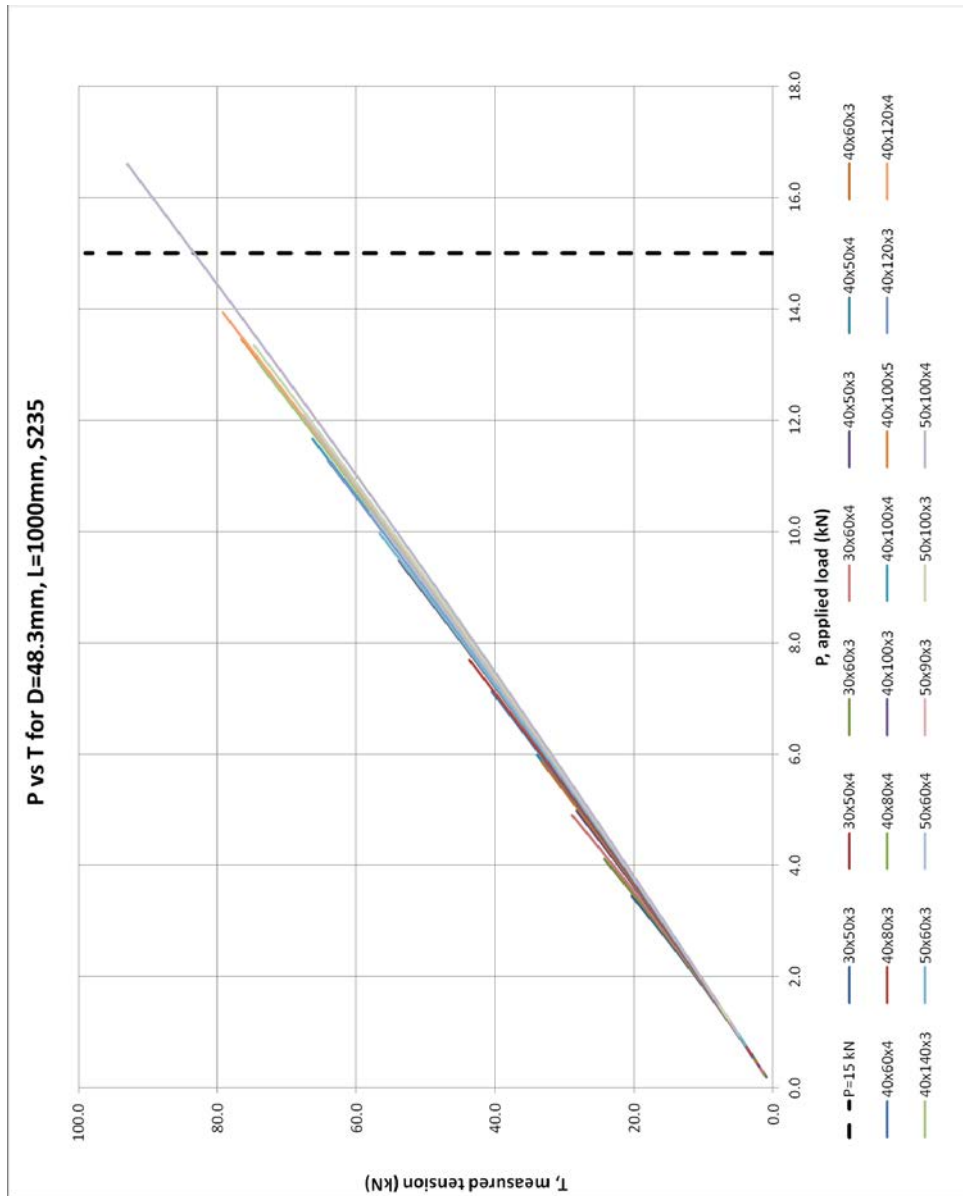


Figure 81. Preliminary optimization, L=1000 mm, S235

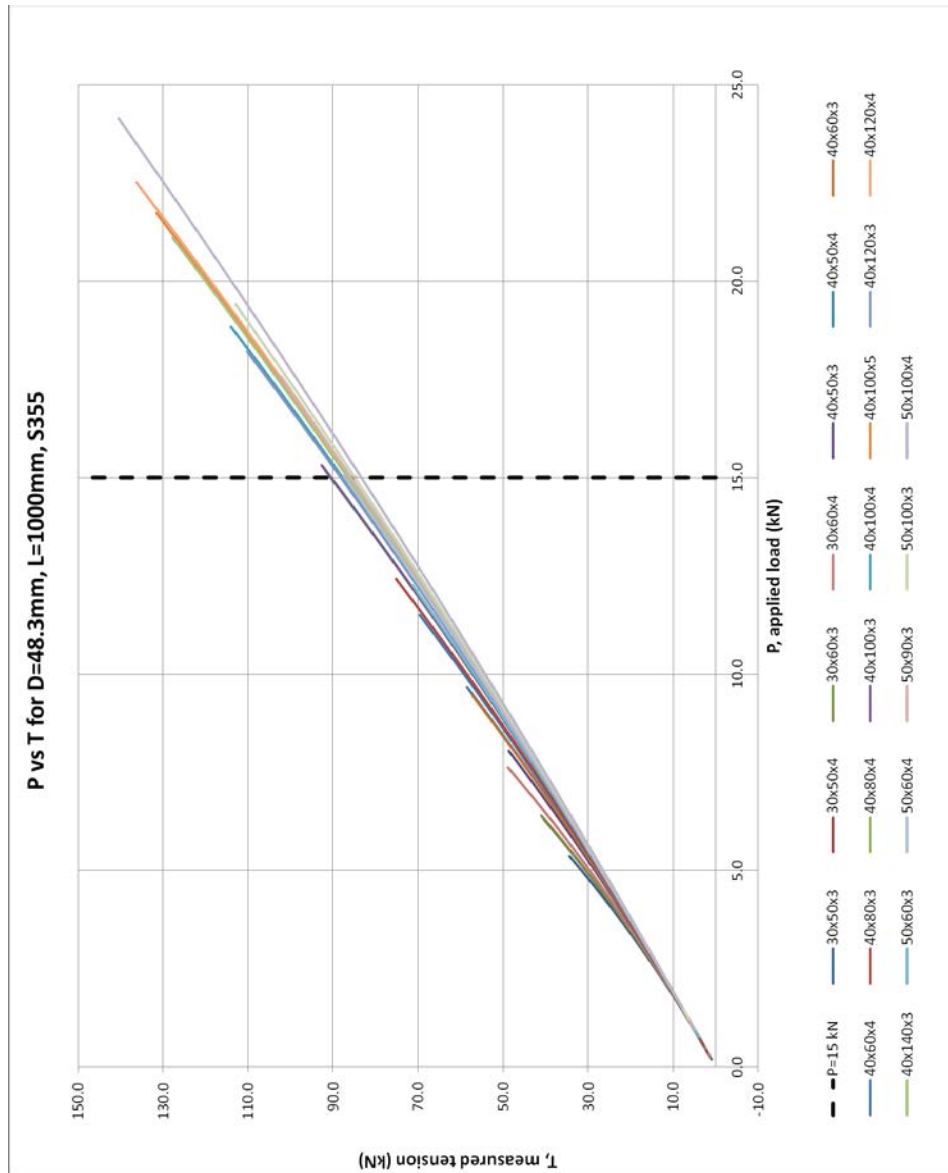


Figure 82. Preliminary optimization, L=1000 mm, S355

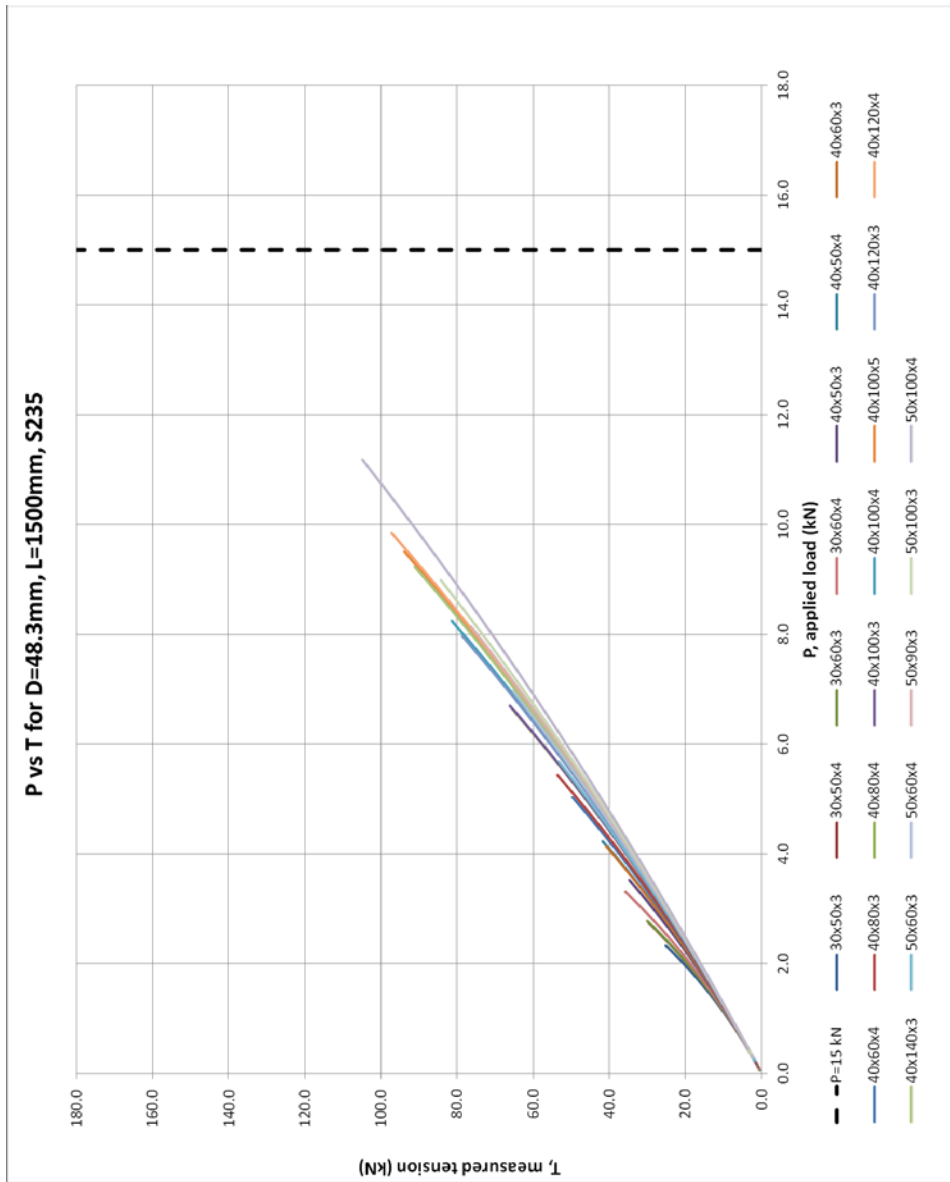


Figure 83. Preliminary optimization, L=1500 mm, S235

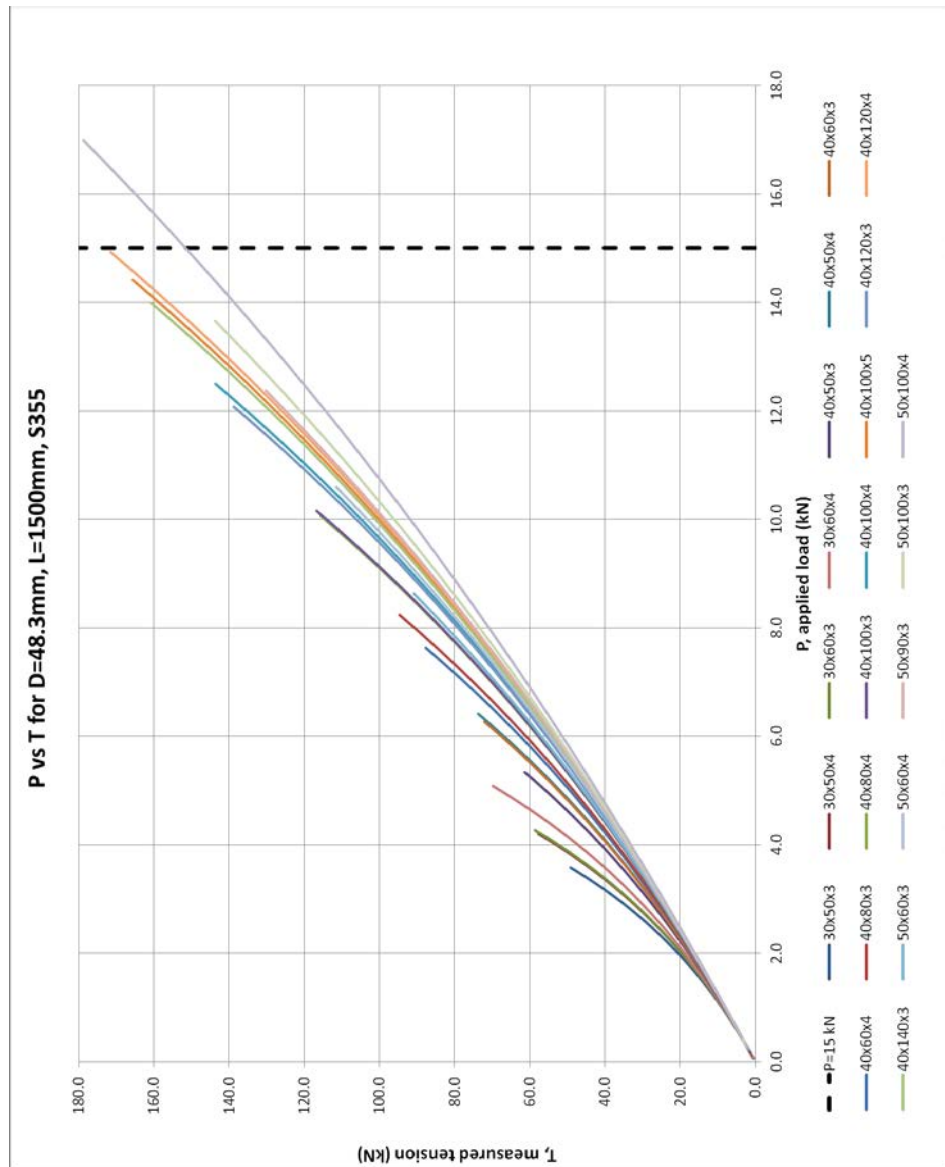


Figure 84. Preliminary optimization, L=1500 mm, S355

APPENDIX B

CABLE AXIAL LOAD MEASUREMENT DEVICE DATA CHARTS FOR DIFFERENT PARAMETERS

Data chart for cable axial load measurement device with different parameters is presented below in Table 9. This chart is prepared by using the parameters below:

- t : cross-section thickness (mm)
- L : beam length (mm)
- L_0 : cable total length (mm)
- σ_y : beam material yield strength (MPa)
- d_c : cable diameter (mm)
- D : circular section diameter (mm)
- d : laser measurement reading (mm)
- P : applied load in installation (kN)
- T : measured tension in cable (kN)
- T' : existing tension in cable (kN)

For this chart, some parameters are fixed and some others are changed to obtain different device configurations. For instance, beam length is fixed to $L=1500$ mm and cable diameter is fixed to $d_c=9.6$ mm. Beam material is used as S235 where $\sigma_y=235$ MPa.

If it is desired to obtain different parameters, the procedure below can be used to create a similar chart.

Procedure for preparing data chart for different parameters:

- For “applied load” P , (see equation ((194)) and “measured total tension” T (see equations ((214), ((207) and Figure 59) indicated relevant equations should be respectively used.
- For existing tension value T' with excluding the additional tension effect due to installation of device, equations (213) and (221) should be solved together.
- These parameters depend on beam cross-section properties, material quality and length, cable diameter and length, and circular section diameter. By changing these parameters, the desired configuration is checked for possibility of using for a specific cable.

Table 9. Cable axial load measurement device data chart for different parameters

D	Lo	b	h	t	d	1	2	3	4	5	6	7	8	9	10	11	12	13	14	15	16	17	18	19	20	21	22	23	24	25				
20	5000	40	40	2.0	P	0.1	0.1	0.2	0.3	0.4	0.4	0.5	0.6	0.7	0.7	0.8	0.9	0.9	1.0	1.1	1.2	1.2	1.3	1.4	1.5	1.5	1.6	1.7	1.8	1.8				
					T	1.9	3.9	6.0	8.1	10.4	12.8	15.4	18.1	20.9	23.9	27.1	30.4	34.0	37.8	41.9	46.3	51.0	56.0	61.5	67.4	73.7	80.7	88.3	96.7	105.9				
					T'	1.6	3.6	5.8	8.0	10.3	12.7	15.3	18.0	20.8	23.8	27.0	30.4	34.0	37.8	41.9	46.3	51.0	56.0	61.5	67.3	73.7	80.7	88.3	96.7	105.9				
20	5000	40	40	2.5	P	0.1	0.2	0.3	0.4	0.4	0.5	0.6	0.7	0.8	0.9	1.0	1.1	1.1	1.2	1.3	1.4	1.5	1.6	1.7	1.8	1.8	1.9	2.0	2.1	2.2				
					T	2.3	4.7	7.2	9.8	12.5	15.4	18.5	21.7	25.1	28.7	32.6	36.6	40.9	45.5	50.4	55.7	61.3	67.4	74.0	81.0	88.7	97.1	106.3	116.3	127.4				
					T'	2.0	4.4	7.0	9.6	12.4	15.4	18.4	21.7	25.1	28.7	32.5	36.6	40.9	45.5	50.4	55.7	61.3	67.4	74.0	81.0	88.7	97.1	106.3	116.3	127.4				
20	5000	40	40	3.0	P	0.1	0.2	0.3	0.4	0.5	0.6	0.7	0.8	0.9	1.0	1.1	1.2	1.3	1.4	1.5	1.6	1.7	1.8	1.9	2.0	2.1	2.2	2.3	2.4	2.5				
					T	2.6	5.4	8.3	11.3	14.5	17.8	21.4	25.1	29.0	33.2	37.6	42.3	47.3	52.6	58.3	64.3	70.9	77.9	85.4	93.6	102.5	112.2	122.7	134.4	147.2				
					T'	2.3	5.2	8.1	11.2	14.4	17.8	21.3	25.0	29.0	33.2	37.6	42.3	47.3	52.6	58.3	64.3	70.8	77.9	85.4	93.6	102.5	112.2	122.7	134.4	147.2				
43	5000	40	40	2.0	P	0.1	0.1	0.2	0.3	0.4	0.4	0.5	0.6	0.7	0.7	0.8	0.9	0.9	1.0	1.1	1.2	1.2	1.3	1.4	1.5	1.5	1.6	1.7	1.8	1.8				
					T	0.7	1.5	2.2	3.0	3.8	4.6	5.4	6.2	7.1	7.9	8.8	9.7	10.6	11.6	12.5	13.5	14.5	15.5	16.5	17.6	18.7	19.8	20.9	22.1	23.2				
					T'	0.0	0.0	0.3	1.2	2.2	3.1	4.0	5.0	5.9	6.9	7.8	8.8	9.8	10.8	11.8	12.8	13.9	14.9	16.0	17.1	18.2	19.3	20.5	21.7	22.9				
43	5000	40	40	2.5	P	0.1	0.2	0.3	0.4	0.4	0.5	0.6	0.7	0.8	0.9	1.0	1.1	1.1	1.2	1.3	1.4	1.5	1.6	1.7	1.8	1.8	1.9	2.0	2.1	2.2				
					T	0.9	1.8	2.7	3.6	4.6	5.5	6.5	7.5	8.5	9.6	10.6	11.7	12.8	13.9	15.1	16.2	17.4	18.7	19.9	21.2	22.5	23.8	25.2	26.5	28.0				
					T'	0.0	0.0	0.8	1.9	3.1	4.2	5.3	6.4	7.5	8.6	9.8	10.9	12.1	13.3	14.5	15.7	16.9	18.2	19.5	20.8	22.1	23.4	24.8	26.2	27.7				
43	5000	40	40	3.0	P	0.1	0.2	0.3	0.4	0.5	0.6	0.7	0.8	0.9	1.0	1.1	1.2	1.3	1.4	1.5	1.6	1.7	1.8	1.9	2.0	2.1	2.2	2.3	2.4	2.5				
					T	1.0	2.1	3.1	4.2	5.3	6.4	7.5	8.7	9.8	11.0	12.3	13.5	14.8	16.1	17.4	18.8	20.1	21.5	23.0	24.5	26.0	27.5	29.1	30.7	32.3				
					T'	0.0	0.0	1.3	2.6	3.9	5.1	6.4	7.7	8.9	10.2	11.5	12.8	14.2	15.5	16.9	18.3	19.7	21.1	22.6	24.1	25.6	27.2	28.8	30.4	32.1				

Table 9. (Continued)

D	Lo	b	h	t	d	1	2	3	4	5	6	7	8	9	10	11	12	13	14	15	16	17	18	19	20	21	22	23	24	25	
					P	0.1	0.3	0.4	0.6	0.7	0.9	1.0	1.2	1.3	1.5	1.6	1.8	1.9	2.1	2.2	2.4	2.5	2.6	2.8	2.9	3.1	3.2	3.4	3.5	3.7	
43	5000	50	50	2.0	T	1.3	2.6	4.0	5.3	6.7	8.1	9.5	11.0	12.5	14.0	15.5	17.1	18.6	20.2	21.9	23.5	25.2	27.0	28.7	30.5	32.3	34.2	36.1	38.0	40.0	
					T'	0.0	0.2	1.9	3.5	5.2	6.8	8.3	9.9	11.5	13.1	14.7	16.4	18.0	19.7	21.4	23.1	24.8	26.6	28.4	30.2	32.0	33.9	35.8	37.8	39.8	
					P	0.2	0.4	0.5	0.7	0.9	1.1	1.2	1.4	1.6	1.8	2.0	2.1	2.3	2.5	2.7	2.9	3.0	3.2	3.4	3.6	3.7	3.9	4.1	4.3	4.5	
43	5000	50	50	2.5	T	1.6	3.2	4.8	6.5	8.1	9.8	11.6	13.3	15.1	16.9	18.8	20.7	22.6	24.5	26.5	28.6	30.6	32.7	34.8	37.0	39.2	41.5	43.8	46.1	48.5	
					T'	0.0	0.8	2.7	4.7	6.6	8.5	10.4	12.3	14.2	16.1	18.0	20.0	22.0	24.0	26.0	28.1	30.2	32.3	34.5	36.7	38.9	41.2	43.5	45.9	48.3	
					P	0.2	0.4	0.6	0.8	1.0	1.2	1.5	1.7	1.9	2.1	2.3	2.5	2.7	2.9	3.1	3.3	3.5	3.7	3.9	4.2	4.4	4.6	4.8	5.0	5.2	
43	5000	50	50	3.0	T	1.8	3.7	5.6	7.5	9.5	11.4	13.5	15.5	17.6	19.7	21.9	24.1	26.3	28.6	30.9	33.2	35.6	38.1	40.6	43.1	45.7	48.3	51.0	53.7	56.5	
					T'	0.0	1.6	3.9	6.1	8.3	10.4	12.6	14.8	16.9	19.1	21.4	23.6	25.9	28.2	30.6	32.9	35.4	37.8	40.3	42.9	45.5	48.1	50.8	53.5	56.3	
					P	0.1	0.1	0.2	0.3	0.4	0.4	0.5	0.6	0.7	0.7	0.8	0.9	0.9	1.0	1.0	1.1	1.2	1.2	1.3	1.4	1.5	1.5	1.6	1.7	1.8	1.8
80	5000	40	40	2.0	T	0.4	0.7	1.1	1.5	1.9	2.3	2.6	3.0	3.4	3.8	4.2	4.6	5.1	5.5	5.9	6.3	6.7	7.2	7.6	8.0	8.5	8.9	9.4	9.8	10.3	
					T'	0.0	0.0	0.0	0.0	0.0	0.0	0.0	0.0	0.0	0.0	0.0	0.0	0.0	0.0	0.1	0.8	1.4	2.0	2.7	3.3	3.9	4.5	5.1	5.7	6.3	6.9
					P	0.1	0.2	0.3	0.4	0.4	0.5	0.6	0.7	0.8	0.9	1.0	1.0	1.1	1.1	1.2	1.3	1.4	1.5	1.6	1.7	1.8	1.8	1.9	2.0	2.1	2.2
80	5000	40	40	2.5	T	0.4	0.9	1.3	1.8	2.3	2.7	3.2	3.7	4.1	4.6	5.1	5.6	6.1	6.6	7.1	7.6	8.1	8.6	9.1	9.7	10.2	10.7	11.3	11.8	12.4	
					T'	0.0	0.0	0.0	0.0	0.0	0.0	0.0	0.0	0.0	0.0	0.0	0.0	0.3	1.1	1.8	2.5	3.3	4.0	4.7	5.4	6.1	6.8	7.5	8.1	8.8	9.5
					P	0.1	0.2	0.3	0.4	0.5	0.6	0.7	0.8	0.9	1.0	1.1	1.1	1.2	1.3	1.4	1.5	1.6	1.7	1.8	1.9	2.0	2.1	2.2	2.3	2.4	2.5
80	5000	40	40	3.0	T	0.5	1.0	1.5	2.1	2.6	3.1	3.7	4.2	4.8	5.3	5.9	6.5	7.0	7.6	8.2	8.8	9.4	10.0	10.6	11.2	11.8	12.4	13.0	13.7	14.3	
					T'	0.0	0.0	0.0	0.0	0.0	0.0	0.0	0.0	0.0	0.0	0.8	1.6	2.5	3.3	4.1	4.9	5.7	6.4	7.2	8.0	8.8	9.5	10.3	11.0	11.8	

Table 9. (Continued)

D	Lo	b	h	t	d	1	2	3	4	5	6	7	8	9	10	11	12	13	14	15	16	17	18	19	20	21	22	23	24	25	
					P	0.1	0.3	0.4	0.6	0.7	0.9	1.0	1.2	1.3	1.5	1.6	1.8	1.9	2.1	2.2	2.4	2.5	2.6	2.8	2.9	3.1	3.2	3.4	3.5	3.7	
80	5000	50	50	2.0	T	0.7	1.4	2.1	2.8	3.5	4.3	5.0	5.7	6.5	7.2	8.0	8.7	9.5	10.3	11.1	11.8	12.6	13.5	14.3	15.1	15.9	16.7	17.6	18.4	19.3	
					T'	0.0	0.0	0.0	0.0	0.0	0.0	0.0	0.0	0.0	1.0	2.1	3.2	4.3	5.3	6.4	7.4	8.4	9.4	10.4	11.4	12.4	13.3	14.3	15.3	16.3	17.2
					P	0.2	0.4	0.5	0.7	0.9	1.1	1.2	1.4	1.6	1.8	2.0	2.1	2.3	2.5	2.7	2.9	3.0	3.2	3.4	3.6	3.7	3.9	4.1	4.3	4.5	
80	5000	50	50	2.5	T	0.8	1.7	2.5	3.4	4.3	5.2	6.0	6.9	7.8	8.7	9.7	10.6	11.5	12.5	13.4	14.4	15.3	16.3	17.3	18.3	19.3	20.3	21.3	22.4	23.4	
					T'	0.0	0.0	0.0	0.0	0.0	0.0	0.3	1.7	3.0	4.3	5.6	6.8	8.0	9.2	10.4	11.5	12.7	13.8	15.0	16.1	17.2	18.4	19.5	20.6	21.8	
					P	0.2	0.4	0.6	0.8	1.0	1.2	1.5	1.7	1.9	2.1	2.3	2.5	2.7	2.9	3.1	3.3	3.5	3.7	3.9	4.2	4.4	4.6	4.8	5.0	5.2	
80	5000	50	50	3.0	T	1.0	2.0	3.0	4.0	5.0	6.0	7.0	8.1	9.1	10.2	11.2	12.3	13.4	14.5	15.6	16.7	17.8	19.0	20.1	21.3	22.5	23.6	24.8	26.0	27.2	
					T'	0.0	0.0	0.0	0.0	0.0	0.3	1.8	3.4	4.8	6.3	7.6	9.0	10.4	11.7	13.0	14.3	15.6	16.9	18.2	19.4	20.7	22.0	23.3	24.6	25.9	
					P	0.1	0.1	0.2	0.3	0.4	0.4	0.5	0.6	0.7	0.7	0.8	0.9	0.9	1.0	1.0	1.1	1.2	1.2	1.3	1.4	1.5	1.5	1.6	1.7	1.8	1.8
20	10000	40	40	2.0	T	1.9	3.9	6.0	8.1	10.4	12.8	15.4	18.1	20.9	23.9	27.1	30.4	34.0	37.8	41.9	46.3	51.0	56.0	61.5	67.4	73.7	80.7	88.3	96.7	105.9	
					T'	1.7	3.8	5.9	8.1	10.4	12.8	15.3	18.0	20.9	23.9	27.0	30.4	34.0	37.8	41.9	46.3	51.0	56.0	61.5	67.3	73.7	80.7	88.3	96.7	105.9	
					P	0.1	0.2	0.3	0.4	0.4	0.5	0.6	0.7	0.8	0.9	1.0	1.0	1.1	1.1	1.2	1.3	1.4	1.5	1.6	1.7	1.8	1.8	1.9	2.0	2.1	2.2
20	10000	40	40	2.5	T	2.3	4.7	7.2	9.8	12.5	15.4	18.5	21.7	25.1	28.7	32.6	36.6	40.9	45.5	50.4	55.7	61.3	67.4	74.0	81.0	88.7	97.1	106.3	116.3	127.4	
					T'	2.1	4.6	7.1	9.7	12.5	15.4	18.5	21.7	25.1	28.7	32.5	36.6	40.9	45.5	50.4	55.7	61.3	67.4	74.0	81.0	88.7	97.1	106.3	116.3	127.4	
					P	0.1	0.2	0.3	0.4	0.5	0.6	0.7	0.8	0.9	1.0	1.1	1.1	1.2	1.3	1.4	1.5	1.6	1.7	1.8	1.9	2.0	2.1	2.2	2.3	2.4	2.5
20	10000	40	40	3.0	T	2.6	5.4	8.3	11.3	14.5	17.8	21.4	25.1	29.0	33.2	37.6	42.3	47.3	52.6	58.3	64.3	70.9	77.9	85.4	93.6	102.5	112.2	122.7	134.4	147.2	
					T'	2.5	5.3	8.2	11.2	14.4	17.8	21.3	25.1	29.0	33.2	37.6	42.3	47.3	52.6	58.3	64.3	70.9	77.9	85.4	93.6	102.5	112.2	122.7	134.4	147.2	

Table 9. (Continued)

D	Lo	b	h	t	d	1	2	3	4	5	6	7	8	9	10	11	12	13	14	15	16	17	18	19	20	21	22	23	24	25
					P	0.1	0.1	0.2	0.3	0.4	0.4	0.5	0.6	0.7	0.7	0.8	0.9	0.9	1.0	1.1	1.2	1.2	1.3	1.4	1.5	1.5	1.6	1.7	1.8	1.8
43	10000	40	2.0	T	0.7	1.5	2.2	3.0	3.8	4.6	5.4	6.2	7.1	7.9	8.8	9.7	10.6	11.6	12.5	13.5	14.5	15.5	16.5	17.6	18.7	19.8	20.9	22.1	23.2	
					T'	0.0	0.4	1.3	2.1	3.0	3.8	4.7	5.6	6.5	7.4	8.3	9.3	10.2	11.2	12.2	13.2	14.2	15.2	16.3	17.3	18.4	19.6	20.7	21.9	23.1
					P	0.1	0.2	0.3	0.4	0.4	0.5	0.6	0.7	0.8	0.9	1.0	1.1	1.1	1.2	1.3	1.4	1.5	1.6	1.7	1.8	1.8	1.9	2.0	2.1	2.2
43	10000	40	2.5	T	0.9	1.8	2.7	3.6	4.6	5.5	6.5	7.5	8.5	9.6	10.6	11.7	12.8	13.9	15.1	16.2	17.4	18.7	19.9	21.2	22.5	23.8	25.2	26.5	28.0	
					T'	0.0	0.7	1.8	2.8	3.8	4.8	5.9	6.9	8.0	9.1	10.2	11.3	12.4	13.6	14.8	16.0	17.2	18.4	19.7	21.0	22.3	23.6	25.0	26.4	27.8
					P	0.1	0.2	0.3	0.4	0.5	0.6	0.7	0.8	0.9	1.0	1.1	1.2	1.3	1.4	1.5	1.6	1.7	1.8	1.9	2.0	2.1	2.2	2.3	2.4	2.5
43	10000	40	3.0	T	1.0	2.1	3.1	4.2	5.3	6.4	7.5	8.7	9.8	11.0	12.3	13.5	14.8	16.1	17.4	18.8	20.1	21.5	23.0	24.5	26.0	27.5	29.1	30.7	32.3	
					T'	0.0	1.0	2.2	3.4	4.6	5.8	7.0	8.2	9.4	10.6	11.9	13.2	14.5	15.8	17.1	18.5	19.9	21.3	22.8	24.3	25.8	27.3	28.9	30.5	32.2
					P	0.1	0.3	0.4	0.6	0.7	0.9	1.0	1.2	1.3	1.5	1.6	1.8	1.9	2.1	2.2	2.4	2.5	2.6	2.8	2.9	3.1	3.2	3.4	3.5	3.7
43	10000	50	2.0	T	1.3	2.6	4.0	5.3	6.7	8.1	9.5	11.0	12.5	14.0	15.5	17.1	18.6	20.2	21.9	23.5	25.2	27.0	28.7	30.5	32.3	34.2	36.1	38.0	40.0	
					T'	0.0	1.4	2.9	4.4	5.9	7.4	8.9	10.5	12.0	13.6	15.1	16.7	18.3	20.0	21.6	23.3	25.0	26.8	28.6	30.4	32.2	34.1	36.0	37.9	39.9
					P	0.2	0.4	0.5	0.7	0.9	1.1	1.2	1.4	1.6	1.8	2.0	2.1	2.3	2.5	2.7	2.9	3.0	3.2	3.4	3.6	3.7	3.9	4.1	4.3	4.5
43	10000	50	2.5	T	1.6	3.2	4.8	6.5	8.1	9.8	11.6	13.3	15.1	16.9	18.8	20.7	22.6	24.5	26.5	28.6	30.6	32.7	34.8	37.0	39.2	41.5	43.8	46.1	48.5	
					T'	0.2	2.0	3.9	5.7	7.5	9.3	11.1	12.9	14.7	16.6	18.5	20.4	22.4	24.3	26.3	28.4	30.4	32.6	34.7	36.9	39.1	41.4	43.7	46.0	48.4
					P	0.2	0.4	0.6	0.8	1.0	1.2	1.5	1.7	1.9	2.1	2.3	2.5	2.7	2.9	3.1	3.3	3.5	3.7	3.9	4.2	4.4	4.6	4.8	5.0	5.2
43	10000	50	3.0	T	1.8	3.7	5.6	7.5	9.5	11.4	13.5	15.5	17.6	19.7	21.9	24.1	26.3	28.6	30.9	33.2	35.6	38.1	40.6	43.1	45.7	48.3	51.0	53.7	56.5	
					T'	0.5	2.6	4.7	6.8	8.9	10.9	13.0	15.1	17.3	19.4	21.6	23.8	26.1	28.4	30.7	33.1	35.5	38.0	40.4	43.0	45.6	48.2	50.9	53.6	56.4

Table 9. (Continued)

D	Lo	b	h	t	d	1	2	3	4	5	6	7	8	9	10	11	12	13	14	15	16	17	18	19	20	21	22	23	24	25
					P	0.1	0.1	0.2	0.3	0.4	0.4	0.5	0.6	0.7	0.7	0.8	0.9	0.9	1.0	1.1	1.2	1.2	1.3	1.4	1.5	1.5	1.6	1.7	1.8	1.8
80	10000	40	2.0		T	0.4	0.7	1.1	1.5	1.9	2.3	2.6	3.0	3.4	3.8	4.2	4.6	5.1	5.5	5.9	6.3	6.7	7.2	7.6	8.0	8.5	8.9	9.4	9.8	10.3
					T'	0.0	0.0	0.0	0.0	0.0	0.0	0.0	0.0	0.1	0.7	1.2	1.7	2.3	2.8	3.3	3.9	4.4	4.9	5.4	6.0	6.5	7.0	7.5	8.1	8.6
					P	0.1	0.2	0.3	0.4	0.4	0.5	0.6	0.7	0.8	0.9	1.0	1.1	1.1	1.2	1.3	1.4	1.5	1.6	1.7	1.8	1.8	1.9	2.0	2.1	2.2
80	10000	40	2.5		T	0.4	0.9	1.3	1.8	2.3	2.7	3.2	3.7	4.1	4.6	5.1	5.6	6.1	6.6	7.1	7.6	8.1	8.6	9.1	9.7	10.2	10.7	11.3	11.8	12.4
					T'	0.0	0.0	0.0	0.0	0.0	0.0	0.0	0.4	1.1	1.7	2.3	3.0	3.6	4.2	4.8	5.4	6.0	6.6	7.3	7.9	8.5	9.1	9.7	10.3	10.9
					P	0.1	0.2	0.3	0.4	0.5	0.6	0.7	0.8	0.9	1.0	1.1	1.2	1.3	1.4	1.5	1.6	1.7	1.8	1.9	2.0	2.1	2.2	2.3	2.4	2.5
80	10000	40	3.0		T	0.5	1.0	1.5	2.1	2.6	3.1	3.7	4.2	4.8	5.3	5.9	6.5	7.0	7.6	8.2	8.8	9.4	10.0	10.6	11.2	11.8	12.4	13.0	13.7	14.3
					T'	0.0	0.0	0.0	0.0	0.0	0.0	0.4	1.2	1.9	2.6	3.3	4.0	4.7	5.4	6.1	6.8	7.5	8.2	8.9	9.6	10.3	11.0	11.7	12.4	13.1
					P	0.1	0.3	0.4	0.6	0.7	0.9	1.0	1.2	1.3	1.5	1.6	1.8	1.9	2.1	2.2	2.4	2.5	2.6	2.8	2.9	3.1	3.2	3.4	3.5	3.7
80	10000	50	2.0		T	0.7	1.4	2.1	2.8	3.5	4.3	5.0	5.7	6.5	7.2	8.0	8.7	9.5	10.3	11.1	11.8	12.6	13.5	14.3	15.1	15.9	16.7	17.6	18.4	19.3
					T'	0.0	0.0	0.0	0.0	0.0	0.8	1.8	2.8	3.7	4.7	5.6	6.5	7.4	8.3	9.2	10.1	11.0	11.9	12.8	13.7	14.6	15.5	16.4	17.3	18.3
					P	0.2	0.4	0.5	0.7	0.9	1.1	1.2	1.4	1.6	1.8	2.0	2.1	2.3	2.5	2.7	2.9	3.0	3.2	3.4	3.6	3.7	3.9	4.1	4.3	4.5
80	10000	50	2.5		T	0.8	1.7	2.5	3.4	4.3	5.2	6.0	6.9	7.8	8.7	9.7	10.6	11.5	12.5	13.4	14.4	15.3	16.3	17.3	18.3	19.3	20.3	21.3	22.4	23.4
					T'	0.0	0.0	0.0	0.0	0.8	2.0	3.2	4.3	5.4	6.5	7.6	8.7	9.8	10.8	11.9	12.9	14.0	15.1	16.1	17.2	18.3	19.3	20.4	21.5	22.6
					P	0.2	0.4	0.6	0.8	1.0	1.2	1.5	1.7	1.9	2.1	2.3	2.5	2.7	2.9	3.1	3.3	3.5	3.7	3.9	4.2	4.4	4.6	4.8	5.0	5.2
80	10000	50	3.0		T	1.0	2.0	3.0	4.0	5.0	6.0	7.0	8.1	9.1	10.2	11.2	12.3	13.4	14.5	15.6	16.7	17.8	19.0	20.1	21.3	22.5	23.6	24.8	26.0	27.2
					T'	0.0	0.0	0.0	0.4	1.8	3.1	4.4	5.7	7.0	8.2	9.4	10.7	11.9	13.1	14.3	15.5	16.7	17.9	19.1	20.4	21.6	22.8	24.1	25.3	26.6